Developing efficient photocatalysts for high-performance decomposition of perfluorooctanoic acid

by Xiaoqing Liu

Thesis submitted in fulfilment of the requirements for
the degree of

Doctor of Philosophy

under the supervision of Prof. Bing-Jie Ni

University of Technology Sydney
Faculty of Engineering and Information Technology

March, 2022

CERTIFICATION OF ORIGINAL AUTHORSHIP

I, Xiaoqing Liu declare that this thesis, is submitted in fulfilment of the requirements for the award of Doctor of Philosophy, in the School of Civil and Environmental Engineering/Faculty of Engineering and Information Technology at the University of Technology Sydney.

This thesis is wholly my own work unless otherwise referenced or acknowledged. In addition, I certify that all information sources and literatures used are indicated in the thesis.

This document has not been submitted for qualifications at any other academic institution.

This research is supported by the Australian Government Research Training Program.

Signature: Production Note:
Signature removed prior to publication.

Date: 15/3/2022

ACKNOWLEDGEMENTS

It is my pleasure to express my deepest gratitude to my principal supervisor Prof. Bruce Ni for his endless support, excellent guidance, constant encouragement, and patients throughout my Ph.D. study. During my Ph.D. period, his advanced academic knowledge, valuable suggestion, and motivation help me to overcome difficulties in my research. I could not finish my Ph.D study within the scheduled time without his help and guidance. His patience and encouragement make me more and more confident, which is an asset in my future study and life. I also would like to thank my co-supervisor Dr. Yiwen Liu, whose suggestions and comments are always valuable in my research. I also would like to express my gratitude to Dr. Xiaoguang Duan from The University of Adelaide, who helps me a lot in my experiments design and paper writing.

I would like to express my deep gratitude to my groupmates for their kindness and knowledge, which helps me a lot during my Ph.D study. My thanks also go to lab managers Dr. Johir and Dr. Niren for their help in setting up experiments and analysing results.

Apart from this, I would like to acknowledge the help and assistance from academic and administration staff from the Faculty of Engineering and Information Technology (FEIT) and Graduate Research School (GRS).

Finally, I would like to give my gratitude to my families and friends, especially the lovely friends in Centre for Technology in Water and Wastewater (CTWW); all of them give me encourage and help during my Ph.D study.

RESEARCH PUBLICATIONS

Publications included in this thesis

1. **Liu, X. Q.**; Wei, W., Xu, J., Wang, D. B., Ni, B. J., Photochemical decomposition of perfluorochemicals in contaminated water. *Water Research.* **2020**, 186, 116311 (IF, 11.236; Q1). (Chapter 2)
2. **Liu, X. Q.**; Xu, B. T., Duan, X. G., Hao, Q., Wei, W., Wang, S. B, Ni, B. J., Facile preparation of hydrophilic In_2O_3 nanospheres and rods with improved performances for photocatalytic degradation of PFOA. *Environmental Science Nano*, **2021**, 8, 1010-1018 (IF, 8.131; Q1). (Chapter 4)
3. **Liu, X. Q.**; Ni, B. J., et al. Fe^{3+} promoted the defluorination of PFOA over In_2O_3. *ACS ES&T Water*, **2021**, 1, 2431-2439. (Chapter 5).
4. **Liu, X. Q.**; Ni, B. J., et al. High-Performance Photocatalytic decomposition of PFOA by BiOX/TiO_2 Heterojunctions: Self-Induced Inner Electric Fields and Band Alignment. *Journal of Hazardous Materials*, **2022**, 430, 128195 (IF, 10.588, Q1) (Chapter 6)
5. **Liu, X. Q.**; Ni, B. J., et al. Bismuth single atoms on TiO_2 as a photocatalyst for the efficient decomposition of PFOA. Submitted. (Chapter 7)

Other publications during candidature

6. **Liu, X. Q.**; Duan, X. G.; Wei, W., Wang, S. B., Ni, B. J., Photocatalytic conversion of lignocellulosic biomass to valuable products. *Green Chemistry.* **2019**, 21, 4266-4289 (IF, 10.182; Q1).
7. **Liu, X. Q.**, Wei, W. and Ni, B.-J. (2021). Photocatalytic and Photoelectrochemical Reforming of Biomass. In Solar-to-Chemical Conversion, H. Sun (Ed.). https://doi.org/10.1002/9783527825073.ch14

TABLE OF CONTENTS

CHAPTER 6 High-performance photocatalytic decomposition of PFOA by $BiOX/TiO_2$

LIST OF TABLES

LIST OF FIGURES

LIST OF ABBREVIATIONS

Symbol	**Description**
PFOA	Perfluorooctanoic acid
PFOS	Perfluorooctanesulfonic acid
PFHpA	Perfluoroheptanoic acid
PFHxA	Perfluorohexanoic acid
PFPeA	Perfluoropentanoic acid
PFBA	Perfluorobutanoic acid
PFPA	Pentafluoropropionic acid
TFA	Trifluoroacetic acid
PFCAs	Perfluorocarboxylic acids
MOFs	Metal-organic frameworks
In-BDC	Indium (III)-benzenedicarboxylate
PFCs	Perfluorinated chemicals
PFECAs	Perfluoroalkyl ether carboxylic acids
PFAS	Perfluoroalkyl substances
DMF	N,N-dimethylformamide
NS	Nanosphere
SEM	Scanning electron microscopy
XRD	X-ray diffraction
ITO	Indium tin oxide
XPS	X-ray photoelectron spectroscopy
SSA	Specific surface areas
TEM	Transmission electron microscopy
ESR	Electron spin resonance
PL	Photoluminescence spectroscopy
DRIFTS	Diffuse reflectance infrared Fourier transform spectroscopy
FTIR	Fourier transform infrared
EIS	Electrochemical impedance spectroscopy
UHPLC-MS/MS	Triple quadrupole ultra-high-performance liquid chromatograph tandem mass spectrometer
MRM	Multiple reaction monitoring

SI	Supporting Information
BJH	Barrett-Joyner-Halenda
BET	Brunauer-Emmett-Teller
BE	Binding energy
O_V	Oxygen vacancy
EIS	Electrochemical impedance spectroscopy
TOC	Total organic carbon
DMPO	5,5-dimethyl-1-pyrroline-N-oxide
TG	Thermogravimetric
MCT	Mercury cadmium telluride
VB	Valence band
CB	Conduction band
BIEF	Built-in electric field
IEF	Internal electric field
BiOX	Bismuth oxyhalide
KX	Potassium halide
BQ	p-benzoquinone
BTA	Tertbutyl alcohol
ROS	Reactive oxygen species
IPA	Isopropanol
TEMPO	2,2,6,6-tetramethylpiperidine-1-oxyl free radical
SACs	Single atom catalysts
SPR	Surface plasmon resonance
HAADF	High angle annular dark field
STEM	Scanning transmission electron microscopy

LIST OF SYMBOLS

Symbol	**Description**
KI	Potassium iodide
$C_7F_{15}COOH$	Perfluorooctanoic acid
$C_6F_{13}COOH$	Perfluoroheptanoic acid
$C_5F_{11}COOH$	Perfluorohexanoic acid
C_4F_9COOH	Perfluoropentanoic acid
C_3F_7COOH	Perfluorobutanoic acid
C_2F_5COOH	Pentafluoropropionic acid
CF_3COOH	Trifluoroacetic acid
e_{cb}^-	Photo-induced electron
NaOAc	Sodium acetate
$In(OH)_3$	Indium hydroxide
Eg	Band gap
F^-	Fluoride ion
In_2O_3	Indium oxide
TiO_2	Titanium dioxide
Ga_2O_3	Gallium oxide
Na_2SO_4	Sodium sulfate
$^{\bullet}OH$	Hydroxyl radical
$O_2^{\bullet-}$	Superoxide radical
t-BuOH	t-butyl alcohol
$FeCl_3$	Ferric chloride anhydrous
Fe^{3+}	Ferric ion
$Na_2C_2O_4$	Sodium oxalate
λ_g	Band gap wavelength

Ph.D. DISSERTATION ABSTRACT

Author:	Xiaoqing Liu
Date:	February 2022
Thesis title:	Developing efficient photocatalysts for high-performance decomposition of perfluorooctanoic acid
Faculty:	Faculty of Environmental and Information Technology
School:	Civil and Environmental Engineering
Supervisors:	Prof. Bruce Ni (Principal supervisor) Dr. Yiwen Liu (Co-supervisor)

Abstract

Perfluorochemicals (PFCs) are a set of chemicals containing C-F bonds, which are concerned due to their persistent and toxicological properties. Perfluorooctanoic acid (PFOA, $C_7F_{15}COOH$) is one of the most widely used PFCs. Photocatalytic approaches appear to be an effective way for the removal of PFCs. We first used metal-organic frameworks (MOFs) derived In_2O_3 for photocatalytic degradation of PFOA under UV light irradiation. The results show that PFOA was completely decomposed in 3 h. MOFs-derived In_2O_3 was super-hydrophilic with a contact angle of ~20º, which facilitated the tight coordination between PFOA and In_2O_3.

Lower calcination temperatures enable higher oxygen vacancy concentrations and larger specific surface area (SSA) of In_2O_3. In_2O_3 prepared at 300 ºC (In_2O_3-300) and 400 ºC (In_2O_3-400) demonstrated better catalytic performance, and PFOA (10 mg L^{-1}) could be completely removed within 4 h, with a defluorination ratio of 39% over In_2O_3-400 in 8h. Fe^{3+} only slightly increased the defluorination ratio of PFOA over In_2O_3-400 to 43%. A much higher defluorination ratio of ~60% was obtained in In_2O_3-600 system after the addition of Fe^{3+}, than the defluorination ratio of ~20% over In_2O_3-600. Combined with a series of characterizations, we speculated that Fe^{3+} participated in the coordination between PFOA and In_2O_3-600, thus promoting the defluorination of PFOA.

The BiOX/TiO_2 heterojunctions demonstrated significantly enhanced efficiency for photocatalytic decomposition of perfluorooctanoic acid (PFOA) compared with BiOX or TiO_2. PFOA (10 mg L^{-1}) was completely degraded by BiOCl/TiO_2 in 8h with a high defluorination ratio of 82 %. The charge transfer and photo-induced electron hole separation were facilitated by the p-n heterojunctions between BiOX and TiO_2 and the inner electric fields (IEF) in BiOX. XRD and TEM characterizations indicated that TiO_2 combined with BiOX along the [110] facet, which facilitated photo-induced electron transfer in the [001] direction, thus benefiting PFOA decomposition.

Single bismuth (Bi) atoms decorated TiO_2 catalyst (N-Bi/TiO_2) was synthesized by a green and simple UV irradiation method using $Bi(NO_3)_3$ as the precursor. When $BiCl_3$ was used as the Bi precursor, BiOCl nanocluster were formed on the surface of TiO_2 (denoted as Cl-Bi/TiO_2). Both N-Bi/TiO_2 and Cl-Bi/TiO_2 demonstrated excellent performance for the defluorination of PFOA. In-situ DRIFTS spectra demonstrated that the Bi single atoms in N-Bi/TiO_2 induced the ionization of C-F bond of PFOA, leading to the deep defluorination of PFOA. Our findings provide approaches for manipulating the photocatalytic activities of In_2O_3 and TiO_2-based composites for the high-performance decomposition of PFOA.

Keywords: Metal-organic frameworks; hydrophilic In_2O_3; In_2O_3; perfluorooctanoic acid; photocatalytic degradation; oxygen vacancies; Fe^{3+}; defluorination ratio; inner electric fields; band alignment; Bi single atoms; in-situ DRIFTS.

CHAPTER 1

Introduction

1.1 Research background

Perfluorinated chemicals (PFCs) are a group of anthropogenic fluorinated organic compounds (Hori et al. 2006, Prevedouros et al. 2006). They have been produced since 1940s for numerous industrial applications such as refrigerants, polymers, pharmaceuticals, adhesives, insecticides, and fire retardants (Baduel et al. 2015, Lehmler 2005, Trojanowicz et al. 2018). PFCs are demonstrated to have considerable effects on the health of human beings (Butenhoff et al. 2012). C-F bond is unreactive due to the high electronegativity and the small atomic radius of fluorine. The bond energy of C–F bond is up to 544 kJ mol^{-1}, leading to its bio-accumulative nature (Xu et al. 2017a). Moreover, PFCs are resistant to conventional oxidation processes which utilize reactive oxygen species (ROS) and biological methods due to the strong C–F bond (Dillert et al. 2007, Schultz et al. 2006). Therefore, effective approaches are essential to convert PFCs to harmless substances under mild conditions.

Basic structure of anthropogenic PFCs is comprised of a fully fluorinated alkyl chain (a hydrophobic part) and a terminated functional group such as carboxylates, sulfonates, sulphonamides, and phosphonates, which constitutes a hydrophilic part. Perfluorocarboxylic acids (PFCAs) especially perfluorooctanoic acid (PFOA) have received tremendous attention recently. Bioaccumulativity of PFCAs is related to their chain length. Short-chain PFCAs are less bio-accumulative than PFOA(Martin et al. 2003). Perfluorooctanesulfonic acid (PFOS) is also one of the primary PFCs, which has been widely found in humans, wildlife, and various environmental media (Benskin et al. 2010, Kannan et al. 2004). Perfluoroalkyl ether carboxylic acids (PFECAs) containing ether C–O bonds are less bio-accumulative alternatives to full-carbon-chain predecessor PFCs (Brandsma et al. 2019). However, studies revealed that some PFECAs exhibited even higher bioaccumulation potential and toxicity than PFOA, and PFECAs have been recognized as a new class of emerging contaminants (Cui et al. 2018).

Photocatalytic reactions are the acceleration of chemical reactions by photo-induced electron/hole, in the presence of a photocatalyst under electromagnetic radiation (Colmenares and Luque 2014b). In recent decades, photocatalysis has been extensively studied for contaminants remediation (Liu et al. 2017b), fine chemical synthesis (Yoon et al. 2010), proton reduction and carbon dioxide (CO_2) reduction (Kuriki et al. 2017). Compared to conventional chemocatalytic approaches, photocatalytic reactions are typically carried out under ambient atmospheric pressure and temperature because of using photon rather than thermal energy. Heterogeneous photochemical processes are widely explored for environmental detoxification of liquid and gaseous ecosystems (Colmenares and Luque 2014a), with the advantages of low energy consumption and high photocatalytic ability (Chen et al. 2015). Although a great many of organic pollutants could be readily transformed to CO_2 and H_2O over TiO_2 photocatalysts, TiO_2 is inefficient for decomposing PFOA under mild conditions, or harsh reaction conditions are required (Dillert et al. 2007, Panchangam et al. 2009). Notably, Ga_2O_3, In_2O_3 are found to be superior to TiO_2 when degrading PFOA in aqueous solution, such as good chemical activity and stability (Li et al. 2020a, Li et al. 2012b). Bismuth based photocatalysts showed good performance in PFOA removal as well (Sahu et al. 2018). However, these photocatalysts are used for PFCs remediation only under UV light irradiation. Few photocatalysts are reported to possess a significant photocatalytic activity for PFOA decomposition under solar light irradiation(Wu et al. 2019b).

Complete mineralization of PFCs to CO_2 and F^- is the final target for pollutant remediation, but this ideal situation for PFCs degradation has not been documented. Therefore, efficient semiconductor photocatalysts are necessary to improve both the decomposition and defluorination efficiencies for PFCs removal.

1.2 Objectives and scope of the research

For heterogeneous photocatalytic processes degrading PFCs, various photocatalysts developed are reviewed. Their instinct properties benefiting PFCs removal are discussed. A linear relationship is obtained between the photocatalytic degradation efficiency of PFOA and the Ovs amount in photocatalysts. Photo-induced e_{cb}^- and h^+ are reactive species of photo-oxidative and photo-reductive approaches for PFOA removal, respectively. And strong binding between PFOA and semiconductor is beneficial for its decomposition. Adjusting aqueous pH and the surface properties of photocatalysts, such as higher Ovs level could benefit the adsorption of PFOA towards photocatalysts, further enhancing its decomposition. But, heterogeneous methods show relatively lower defluorination efficiency compared to homogenous photocatalytic processes. For this instance, various efficient semiconductor photocatalysts have been developed to achieve efficient defluorination of PFOA under UV light or Xenon lamp irradiation.

The specific objectives of this study are as follows:

1) To design In_2O_3 and investigate its properties for the efficient decomposition and defluorination of PFOA.
2) To study the effect of Fe^{3+} on the decomposition of PFOA over In_2O_3 and investigate why Fe^{3+} could enhance the defluorination of PFOA over In_2O_3.
3) To fabricate BiOX/TiO_2 heterojunctions and explore the charge separation pathway for the highly efficient defluorination of PFOA.
4) To develop an easy and mild method for the preparation of Bi SAs deposited on the surface of TiO_2 and demonstrate its high performance for the defluorination of PFOA.

1.3 Research significance

This study provides methods for the preparation of semiconductor photocatalysts for the efficient photocatalytic decomposition and defluorination of PFOA. PFOA is one of the most widely used perfluorochemicals which have raised great concern due to their wide distribution, persistence and toxicity. Hydrophilic In_2O_3 is prepared by facilely calcination of In-based MOF and demonstrated significant enhanced activities for the photocatalytic decomposition and defluorination of PFOA. Moreover, homogeneous and heterogeneous photocatalytic processes are also combined to enable a deep defluorination of PFOA. Specifically, Fe^{3+} is added in the In_2O_3/UV system and greatly enhances the photocatalytic defluorination of PFOA. Bismuth based semiconductors appear to be efficient for the photocatalytic degradation of PFOA. BiOX/TiO_2 p-n heterojunctions are synthesized by hydrothermal reactions in ethylene glycol solvent. BiOX/TiO_2 demonstrated significantly enhanced efficiency for the photocatalytic defluorination of PFOA, with a defluorination ratio of 82% obtained in BiOCl/TiO_2 system. Bi SAs deposited on TiO_2 are prepared by a facile method by irradiation of $Bi(NO_3)_3$ dissolved in TiO_2 dispersion. A deep defluorination of PFOA is also obtained with a defluorination ratio of 85%. Overall, the present study helps to broaden the overview of purposely developing efficient photocatalysts to remediate PFOA

1.4 Organization of the thesis

The thesis includes 8 chapters, and the main contents of each chapter are listed below (Figure 1.1).

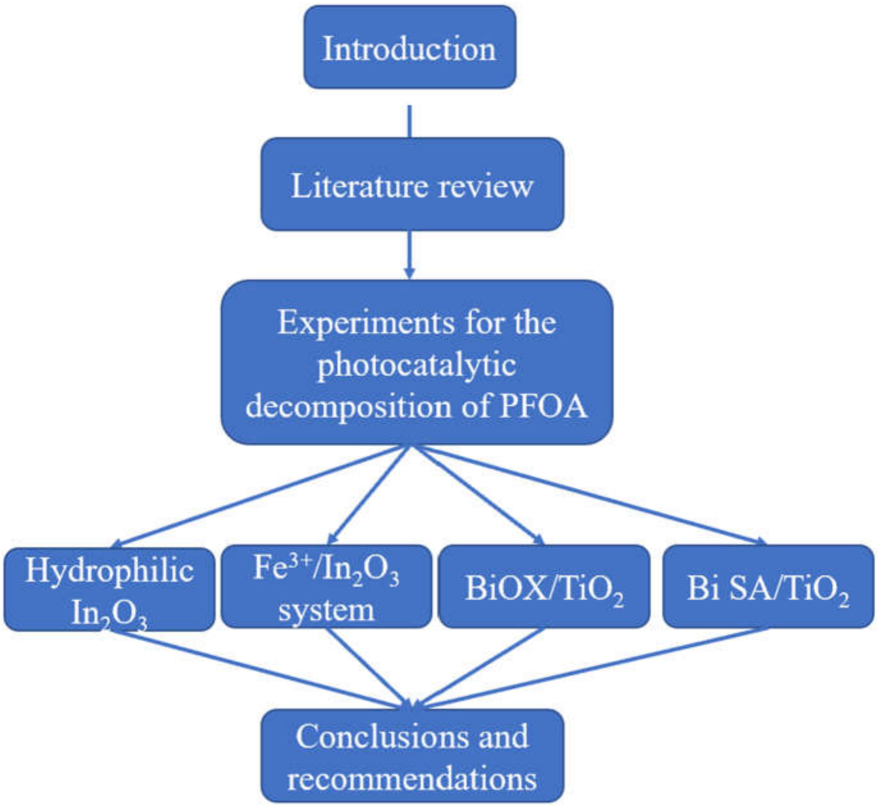

Figure 1.1 The main structure of this thesis.

Chapter 1 generally describes the background of this study. The significance and the scope are included in this section.

Chapter 2 provides a review of the recent developments in the heterogeneous photocatalytic decomposition and defluorination of PFOA.

Chapter 3 describes the preparation of semiconductor photocatalysts and the analysis methods for the characterization of the prepared catalysts. Moreover, in-situ techniques to investigate the decomposition of PFOA are also introduced in Chapter 3.

Chapter 4 facilely prepared hydrophilic In_2O_3 by the calcination of In-based MOF and demonstrated its good performance for the efficient degradation of PFOA under UV254 nm irradiation. The hydrophilic In_2O_3 possessed particle size of only 20-50 nm. Moreover, a tighter coordination was formed between PFOA and MOF-derived In_2O_3 than that between commercial In_2O_3 and PFOA. These properties led to the significant enhancement of the photocatalytic defluorination of PFOA.

Chapter 5 mainly describes that Fe^{3+} could promote the photocatalytic defluorination of PFOA over In_2O_3. In_2O_3 catalysts were prepared by the calcination of $In(OH)_3$ at different temperatures, i.e. 300, 400, 500 and 600 °C (denoted as In_2O_3-300, In_2O_3-400, In_2O_3-500 and In_2O_3-600). In_2O_3-300 and In_2O_3-400 had better activities than In_2O_3-500 and In_2O_3-600, due to the higher OVs and larger SSA. However, when Fe^{3+} was added to the system, the defluorination ratio of PFOA over In_2O_3-600 was greatly enhanced. While Fe^{3+} could only slightly enhance the defluorination of PFOA over In_2O_3-400. In-situ DRIFTS spectra indicated that Fe^{3+} maybe could participate in the coordination between PFOA and In_2O_3-600, thus promoting its defluorination ratio.

Chapter 6 prepared the $BiOX/TiO_2$ (X=Cl, Br and I) heterojunctions and demonstrated its high performance for the deep defluorination of PFOA. $BiOCl(Br)/TiO_2$ exhibited great enhancement than BiOCl(Br) for the photocatalytic defluorination of PFOA. While, $BiOI/TiO_2$ only had slight increase than BiOI. XRD and TEM characterizations indicate that BiOX connects with TiO_2 along the [110] facet. Internal electric field in BiOX will guide the photo-induced electrons transfer from BiOX to TiO_2 in the [001] direction, and photo-induced holes from TiO_2 to BiOX along [110] facet. Moreover, the band alignment between BiOCl(Br) and TiO_2 will separate the photo-induced holes and electrons in BiOCl(Br) and TiO_2, respectively. All these internal guidance contribute to the high performance of $BiOCl(Br)/TiO_2$ composites.

Chapter 7 prepared Bi SAs deposited on TiO_2 by irradiation using $Bi(NO_3)_3$ as the precursor (denoted as N-Bi/TiO_2). When $BiCl_3$ was adopted as the precursor, BiOCl nanoclusters were generated on the surface of TiO_2 (denoted as Cl-Bi/TiO_2). Both N-Bi/TiO_2 and Cl-Bi/TiO_2 demonstrated excellent performance for the defluorination of PFOA under UV 254 nm or Xenon lamp irradiation. STEM and EXAFS confirmed the formation of Bi SAs and BiOCl nanoclusters on the surface of TiO_2. DRIFTS and in-situ DRIFTS revealed that Bi SAs may induce the ionization of C-F bond, thus leading to the deep defluorination of PFOA.

Chapter 8 summarizes the main results of the studies in this thesis and proposes future research challenges and perspectives in this field.

CHAPTER 2

Literature review

2.1 Introduction

Perfluorooctanoic acid (PFOA), as a representative of perfluorinated chemicals (PFCs), has been detected globally in water, air, wildlife, and humans. Exposure to PFOA can lead to liver damage, and possibly cancer. These chemicals are very stable as carbon-fluorine (C-F) bond is very strong with a bond energy of 544 kJ/mol, clearly demonstrating its persistent and bioaccumulative nature in the environment.(Xu et al. 2017a) Therefore, it is necessary and urgent to develop feasible methods to decompose PFOA into harmless molecules. Various approaches including ultrasonication, aqueous electron reduction, persulfate oxidation, have been studied for the degradation of PFOA (Li et al. 2012c). However, these methods require harsh reaction conditions or/and high energy consumption. Among potential methods for PFOA decomposition, heterogeneous photocatalysis is attractive due to its low energy cost and high efficiency. However, TiO_2, the most widely used photocatalyst, demonstrated very low efficiency for PFOA decomposition under mild conditions. β-Ga_2O_3 and In_2O_3 showed good activity to decompose PFOA (Xu et al. 2017a). And their activity can be further enhanced via modulation of the structure, morphology, and particle size of the materials. For example, sheaf-like Ga_2O_3 was self-assembled from nanoplates and showed good activity for the mineralization of PFOA under UV light irradiation (Shao et al. 2013a). Bismuth (Bi)-based photocatalysts also demonstrated good performance for the photocatalytic degradation of PFOA. And the reported photocatalysts, their performances for the photocatalytic degradation of PFOA, together with the properties impacting the activities of photocatalysts are concluded in this chapter.

2.2 Heterogeneous photochemical process for PFCs decomposition

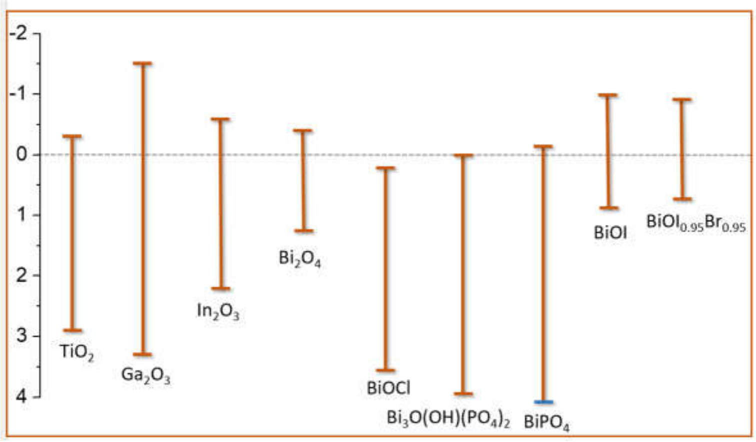

Figure 2.1 Band energy diagram of semiconductors used for PFOA decomposition.

Heterogeneous photocatalysis is an efficient approach for PFCs removal from contaminated water, the related studies are concluded in Table 2.1. Up to date, there are only a few semiconductors studied for the photocatalytic degradation of PFCs, and researches are only focused on the decomposition of PFOA. Figure 2.1 displays the band energy diagram of semiconductors studied for the degradation of PFOA. The performance and mechanisms of these photocatalysts for remediating PFOA in contaminated water are discussed according to the photo-oxidative and photo-reductive pathways. Mainly focused on bismuth-based photocatalysts, In_2O_3, Ga_2O_3.

2.2.1 Photo-reductive processes

Semiconductor photocatalysis can degrade PFCs in a reductive way. B-Ga_2O_3 with a wide bandgap was employed for photocatalytic decomposition of PFOA (Zhao et al. 2015, Zhao and Zhang 2009). The β-Ga_2O_3 has much wider bandgap (4.8 eV) than TiO_2 (3.2 eV). And its conduction band position (E_{CB} = –1.55 eV) is much higher than TiO_2 (E_{CB} = –0.29 eV) relative to the vacuum energy level (Fig. 4) (Zhao et al. 2015). Therefore, photo-induced electrons (e_{cb}^-) in the conduction band of β-Ga_2O_3 have stronger reductive capability than that of TiO_2. PFOA molecules adsorbed on the surface of β-Ga_2O_3 could be reductively decomposed in an anaerobic atmosphere (Zhao and Zhang 2009). Photocatalytic reduction of PFOA by β-Ga_2O_3 was also investigated in anoxic aqueous solution (Zhao et al. 2015, Zhao et al. 2012). After reacting for 3 h, 98.8% of PFOA was degraded with a defluorination efficiency of 31.6% in the presence of thiosulfate and bubbling N_2. A possible mechanism was proposed, involving the attack of e_{cb}^- onto the carboxyl of $C_nF_{2n+1}COOH$. The generated $C_nF_{2n+1}^\bullet$ reacted with

H_2O to form $C_nF_{2n+1}OH$, and then $C_nF_{2n+1}OH$ underwent HF elimination and hydrolysis to form $C_{n-1}F_{2n-1}COOH$.

Wang et al. reported that oxalic acid could greatly improve PFOA decomposition over TiO_2, under N_2 atmosphere (Wang and Zhang 2011). EPR results confirmed the formation of $CO_2^{\bullet-}$, which was produced from reactions between oxalic acid and photo-generated h^+ (Eq.1 and Eq. 2). Oxalic acid can also remarkably prolong the life time of photo-generated e_{cb}^- by reacting with photo-generated h^+. $CO_2^{\bullet-}$ is a strong reductant with a normal potential of −1.85 V (Surdhar et al. 1989). The authors propose that both e_{cb}^- and $CO_2^{\bullet-}$ could possibly initiate the decarboxylation of PFOA (Eq.3 and Eq.4) to form $C_7F_{15}^\bullet$. Then, $C_7F_{15}^\bullet$ would rapidly react with H_2O to produce $C_7F_{15}OH$ and forming $C_6F_{13}COF$ after eliminating HF (Eq.5 and Eq.6). $C_6F_{13}COF$ was unstable and underwent hydrolysis to form $C_6F_{13}COOH$ (Eq.7). $C_6F_{13}COOH$ would undergo the same way to be completely mineralized to CO_2 and F^-. $CO_2^{\bullet-}$ was primarily responsible for PFOA decomposition due to its significantly larger reduction potential compared with e_{cb}^-. And 86.7% pf PFOA could be decomposed in 180 min, with the addition of 3 mM oxalic acid and under nitrogen atmosphere.

$$TiO_2 + h\nu \rightarrow h^+ + e_{cb}^- \qquad (1)$$

$$C_2O_4^{2-} + h^+ \rightarrow CO_2 + CO_2^{\bullet-} \qquad (2)$$

$$C_7F_{15}COOH + e^- + H^+ \rightarrow C_7F_{15}^\bullet + HCOOH \qquad (3)$$

$$C_7F_{15}COOH + CO_2^{\bullet-} + H^+ \rightarrow C_7F_{15}^\bullet + HCOOH + CO_2 \qquad (4)$$

$$C_7F_{15}^\bullet + H_2O \rightarrow C_7F_{15}OH + H^\bullet \qquad (5)$$

$$C_7F_{15}OH \rightarrow C_6F_{13}COF + H^+ + F^- \qquad (6)$$

$$C_6F_{13}COF + H_2O \rightarrow C_6F_{13}COOH + H^+ + F^- \qquad (7)$$

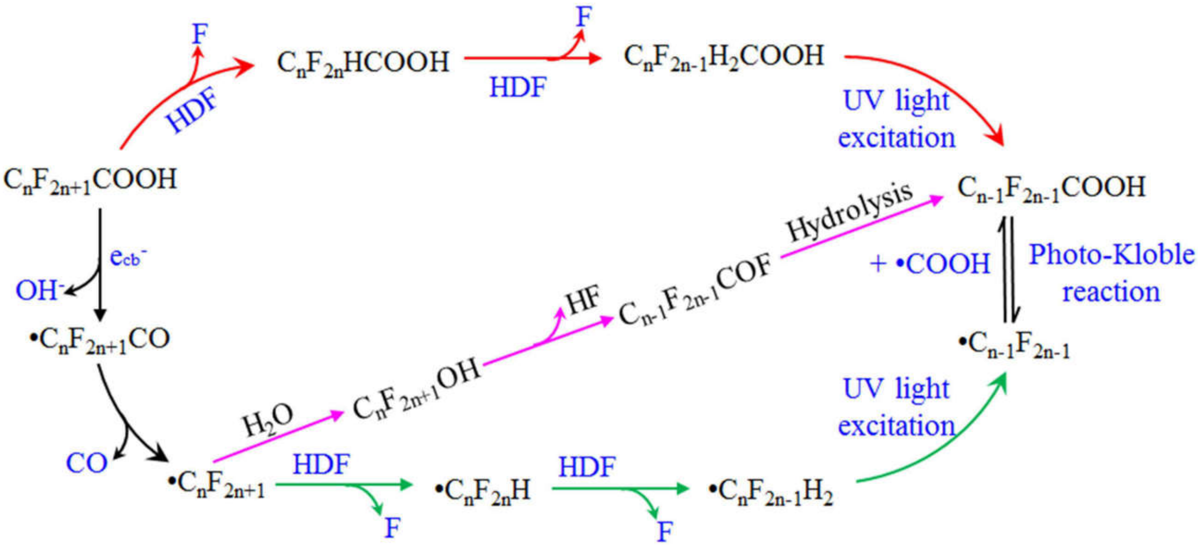

Figure 2.2 Photoinduced hydrodefluorination mechanisms of PFOA with SiC/Graphene at room temperature. The dosage of SiC/Graphene was 0.5 g L^{-1}, the wavelength of UV light was 254 nm, the pH value was 7, and the concentration of PFOA was 0.12 mmol L^{-1} (Huang et al. 2016a).

PFOA was decomposed under UV light irradiation with SiC/Graphene catalyst (Huang et al. 2016a). Reactive Si-H bonds were generated under UV light irradiation and responsible for reductive cleavage of C-F bonds via Si-H/C-F redistribution, consequently resulting in CH_2 carbene from hydrogen-containing perfluoroalkyl chains, and the C–C bonds scission (Fig. 2.2). Besides that, carbonyl groups were attacked by e_{cb}^{-}, yielding perfluoroalkyl radicals ($\bullet C_nF_{2n+1}$) by losing HO^{-} and CO. There were two main reaction pathways for the subsequent transformation of $\bullet C_nF_{2n+1}$. On one hand, it reacted with H_2O to generate unstable $C_nF_{2n+1}OH$, which then underwent HF elimination and hydrolysis to form $C_{n-1}F_{2n-1}COOH$. On the other hand, the hydro–defluorination also took place via Si-H/C-F redistribution at chain-terminal of $\bullet C_nF_{2n+1}$, thus yielding $\bullet C_{n-1}F_{2n-1}$ by removing CH_2 carbene. Furthermore, addition or elimination of $\bullet COO^{-}$ induced mutual transformation between $C_{n-1}F_{2n-1}\bullet$ and $C_{n-1}F_{2n-1}COOH$.

A new method for reductive defluorination of PFOA under visible light was conducted by using Pt-Bi_2O_4 as photocatalysts and KI as electron donors (Wang et al. 2020c). The defluorination of PFOA proceeded in a photo-reductive pathway, in which the photo-induced e_{cb}^{-} was the dominate active species. Pt served as co-catalyst to trap e_{cb}^{-}, while KI could trap photo-generated h_{vb}^{+} to promote e_{cb}^{-}- h^{+} separation. Due to the high affinity of e_{cb}^{-}, the e_{cb}^{-} firstly attacked F atom at α-position, resulting in the replacement of F with H atom to form $C_7F_{13}H_2COOH$. The produced $C_7F_{13}H_2COOH$ was further transformed to $C_6F_{13}COOH$ (Eq.8 and Eq.9). Then, the generated $C_6F_{13}COOH$ was further decomposed in the same way and finally mineralized to F^{-} and CO_2.

$$C_7F_{13}H_2COOH \rightarrow \bullet C_6F_{13} +: CH_2 + \bullet COOH \quad (8)$$

$$\bullet C_6F_{13} + \bullet COOH \rightarrow C_6F_{13}COOH \quad (9)$$

The e_{cb}^{-} production from heterogeneous catalytic systems is rarely reported. Shao et al. demonstrated the production of photo-induced e_{cb}^{-} from diamond/UV system for the efficient degradation of PFOA (Liu et al. 2021a). UV/diamond system has a wide pH applicability (pH 2-pH 11). This system could help to solve the secondary pollution caused by the homogeneous system, such as UV/sulfite system, which is pH dependent.

2.2.2 Photo-oxidative processes

Photo-induced h^+ was mainly responsible for the heterogeneous photo-oxidative decomposition of PFOA. Other ROS (e.g. $OH^{\bullet}$) also participate in the decomposition process. Unstable perfluoroalkyl radical ($C_7F_{15}COO^{\bullet}$) is generated from oxidation of the adsorbed PFOA by the photo-generated h^+ (Eq. 10), and subsequently decarboxylated to form $\bullet C_7F_{15}$ (Eq. 11). $\bullet C_7F_{15}$ radical is unstable and may react with $OH^{\bullet}$, forming $C_6F_{13}COF$ after eliminating HF (Eq. 12 and Eq. 13). $C_6F_{13}COF$ further undergoes hydrolysis to generate $C_6F_{13}COOH$ (Eq. 14). $C_6F_{13}COOH$ then undergoes the same way as $C_7F_{15}COOH$ and decomposed in a stepwise manner. The amount of h_{vb}^+ and the adsorption capacity of PFOA are two key parameters that determine the degradation efficiency of semiconductors under UV/visible light irradiation. And these two key parameters can be optimized by adjusting inherent properties of semiconductors and operation conditions of degradation reactions.

$$C_7F_{15}COO^- + h_{vb}^+ \rightarrow C_7F_{15}COO^{\bullet} \tag{10}$$

$$C_7F_{15}COO^{\bullet} \rightarrow C_7F_{15}^{\bullet} + CO_2 \tag{11}$$

$$C_7F_{15}^{\bullet} + OH^{\bullet} \rightarrow C_7F_{15}OH \tag{12}$$

$$C_7F_{15}OH \rightarrow C_6F_{13}COF + HF \tag{13}$$

$$C_6F_{13}COF + H_2O \rightarrow C_6F_{13}COOH + HF \tag{14}$$

Table 2.1 Photocatalytic removal of PFOA by different semiconductor photocatalysts.

Photochemical catalyst	Pollutant	Light wavelength	Power	Conditions	Reaction time	Degradation ratio &Defluorination ratio	Ref.
$TiO_2/H_2C_2O_4$	PFOA	254 nm	23 W	C_0=24 μM pH=2.47 $C_{catalyst}$=0.5 g L^{-1} N_2 atomosphere	3 h	86.7% & 16.5%	(Wang and Zhang 2011)
$TiO_2/HClO_4$	PFOA	254 nm	16 W	C_0=120 μM pH=2.47 $C_{catalyst}$=0.66 g L^{-1} O_2 atmosphere	7 h	97% & 38%	(Panchangam et al. 2009)

TiO_2/O_3	PFOA	254 nm	28 W	C_0=10 mg L^{-1} $C_{catalyst}$=0.2 g L^{-1} O_3 dosage: 25 mg h^{-1}	4 h	99.1% & 44.3%	(Huang et al. 2016b)
Ga_2O_3	PFOA	254 nm	14 W	C_0=0.5 mg L^{-1} $C_{catalyst}$=0.5 g L^{-1} N_2 atmosphere	3 h	36% & 15%	(Zhao and Zhang 2009)
Sheaf-like Ga_2O_3	PFOA	254 nm	14 W	C_0=0.5 mg L^{-1} $C_{catalyst}$=0.5 g L^{-1} O_2 atmosphere	45 min	100% & 60%	(Shao et al. 2013a)
Needle-like Ga_2O_3	PFOA	254 nm	14 W	C_0=0.5 mg L^{-1} $C_{catalyst}$=0.5 g L^{-1} O_2 atmosphere	1 h	100% & 58%	(Shao et al. 2013b)
β-Ga_2O_3	PFOA	254 nm	50 W	C_0=10 mg L^{-1} $C_{catalyst}$=0.5 g L^{-1} N_2 atmosphere	1.5 h	100% & 56%	(Zhao et al. 2015)
In_2O_3	PFOA	254 nm	23 W	C_0=40 mg L^{-1} $C_{catalyst}$=3.4 g L^{-1} O_2 atmosphere	4 h	80% & 33%	(Li et al. 2012b)
In_2O_3 NPNs	PFOA	254 nm	23 W	C_0=30 mg L^{-1} $C_{catalyst}$=0.5 g L^{-1} O_2 atmosphere	0.5 h	100% & 71%	(Li et al. 2012c)
In_2O_3 microspheres	PFOA	254 nm	15 W	C_0=30 mg L^{-1} $C_{catalyst}$=0.5 g L^{-1} O_2 atmosphere	17 min	100% & –	(Li et al. 2013b)
In_2O_3 nanocubes	PFOA	254 nm	15 W	C_0=30 mg L^{-1} $C_{catalyst}$=0.5 g L^{-1}	2 h	100% & –	(Li et al. 2013b)

				O_2 atmosphere			
In_2O_3 nanoplates	PFOA	254 nm	15 W	C_0=30 mg L^{-1} $C_{catalyst}$=0.5 g L^{-1} O_2 atmosphere	42 min	100% & –	(Li et al. 2013b)
In_2O_3 with graphene	PFOA	254 nm	15 W	C_0=30 mg L^{-1} $C_{catalyst}$=0.5 g L^{-1} O_2 atmosphere	3 h	100% & 60.9%	(Li et al. 2013a)
In_2O_3/0.86 % CeO_2	PFOA	254 nm	500 W	C_0=100 mg L^{-1} $C_{catalyst}$=0.4 g L^{-1}	1 h	100% & –	(Jiang et al. 2016)
MnO_x-In_2O_3	PFOA	Xenon lamp	500 W	C_0=50 mg L^{-1} $C_{catalyst}$=0.5 g L^{-1}	4 h	100% & 3%	(Wu et al. 2019b)
BiOCl	PFOA	254 nm	10 W	C_0=20 μM $C_{catalyst}$=0.5 g L^{-1}	12 h	100% & 59.3%	(Song et al. 2017)
BiOCl/Zn-Al hydrotalcite	PFOA	< 350 nm	500 W	C_0=0.5 mg L^{-1} pH=2.0 $C_{catalyst}$=0.5 g L^{-1}	6 h	90% &	(Yang et al. 2020b)
Surface defective BiOCl	PFOA	Xenon lamp	300 W	C_0=50 μM pH=3.9 $C_{catalyst}$=1 g L^{-1}	8.5 h	68.8% & 12.86%	(Sun et al. 2019)

Enhanced adsorption of PFOA and a strong binding between PFOA and heterogeneous semiconductors, would benefit the direct oxidation of PFOA by h^+. Inherent properties of semiconductors have great impact on the adsorption capacity of photocatalysts. Larger SSA of photocatalysts helps to expose more active surfaces and enhances the adsorption capacity for PFOA. It is reported that higher oxygen vacancy (OV) level would facilitate the adsorption of PFOA onto semiconductors (Li et al. 2013c). The bidentate coordination allows closer contact between PFOA and photocatalysts than that of monodentate mode (Li et al. 2012b, Song et al. 2017).

Moreover, a side-on parallel mode with both the head and tail groups anchored on the photocatalysts is reported to be much more efficient for PFOA decomposition (Li et al. 2020b). The optimization approaches for different classes of semiconductors are discussed in detail along with the enhanced performance for PFOA degradation.

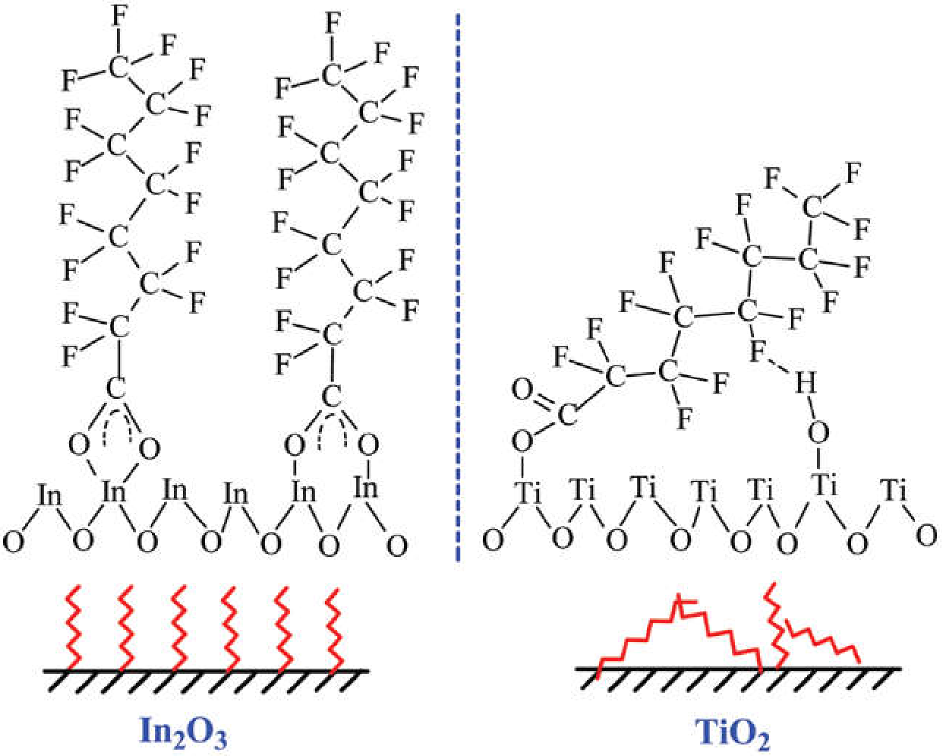

Figure 2.3 Schematic diagram of PFOA configurations adsorbed on In_2O_3 and TiO_2 (Li et al. 2012b).

In_2O_3 exhibited enhanced activity than TiO_2 for PFOA decomposition (Li et al. 2012b). The binding pattern to TiO_2 surface was monodentate, and the binding strength was relatively weaker. Therefore, the h_{vb}^+ of TiO_2 are preferentially transformed to hydroxyl radicals ($OH^•$) which is less reactive for PFOA degradation, indicated by electron spin resonance (ESR) results (Li et al. 2012b). PFOA closely coordinates to In_2O_3 in a bidentate or bridging mode (Fig. 2.3). The strong bidentate binding between carboxylic group of PFOA and In_2O_3 surface benefited direct decomposition of PFOA by photo-induced h_{vb}^+. The main decomposition products of In_2O_3 are similar to those of TiO_2, including C2-C7 PFCAs and fluoride ions. Thereafter, In_2O_3 nanostructures with different morphologies were prepared and exhibited distinct properties. Three kinds of nanostructured In_2O_3 materials were fabricated by dehydration of the corresponding $In(OH)_3$ nanostructures at 500 ℃ for 2h (Fig. 2.3a and Fig. 2.3b). The decomposition rates of PFOA by these In_2O_3 materials, *i.e.* porous microspheres, nanoplates and nanocubes were 74.7, 41.9 and 17.3 times higher than that using P25 TiO_2, respectively (Fig. 2.4c) (Li et al. 2013b). Higher surface oxygen vacancies (Ovs) level benefited the adsorption of PFOA towards In_2O_3. The more Ovs defects existed in In_2O_3 materials. The better activity was obtained for PFOA decomposition (Fig. 2.4d).

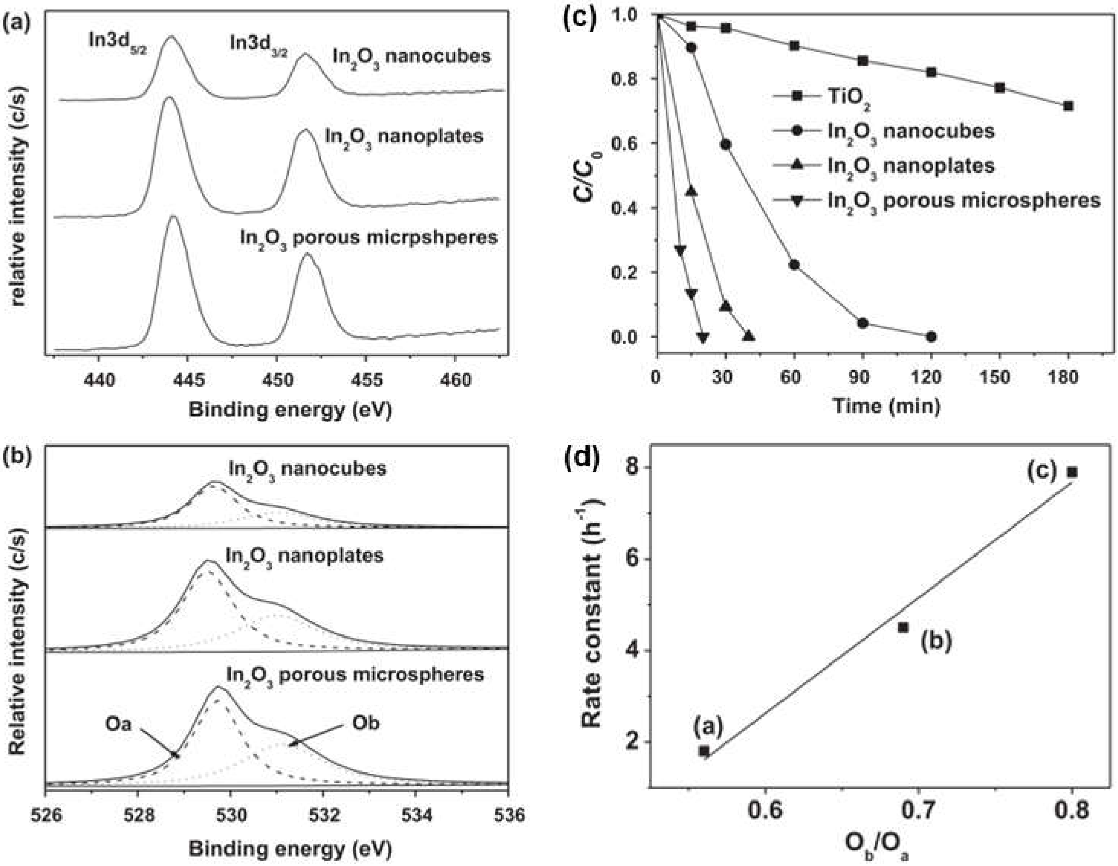

Figure 2.4 XPS spectra of In 3d (a) and O 1s (b) of different In_2O_3 samples; Photocatalytic decomposition of PFOA by different In_2O_3 samples (c); The photocatalytic activity of three nanostructured In_2O_3 materials vs their O_b/O_a ratio: (a) In_2O_3 nanocubes, (b) In_2O_3 nanoplates, and (c) In_2O_3 porous microspheres (d) (Li et al. 2013b).

A semiconductor of wide band gap, p-block metal oxyhydroxide InOOH was prepared and exhibited high activity for PFOA degradation under UV light irradiation at mild conditions (Xu et al. 2017c). The rate constant for PFOA degradation by InOOH is 27.6 times higher than that by P25. The main reason is that InOOH have an enhanced adsorption capacity for ionized PFOA ($C_7F_{15}COO^-$) than P25.

Sheaf-like Ga_2O_3 was prepared via a polyvinyl alcohol (PVA)-assisted hydrothermal method followed by heat treatment(Shao et al. 2013a), and exhibited superior photocatalytic activity for PFOA degradation under UV 254 nm light irradiation. The decomposition rate constant was 4.85 h^{-1}, which was 16 and 44 times higher than that using commercial Ga_2O_3 and P25 TiO_2, respectively. Needle-like β-Ga_2O_3 was also prepared and used as photocatalyst for PFOA decomposition(Shao et al. 2013b). The prepared material was efficient for the removal of trace PFOA in both pure water and wastewater, with first-order rate constants of 4.03 and 3.51 h^{-1}, respectively. Diffuse reflectance infrared Fourier transform spectroscopy (DRIFTS) revealed the tight coordination of PFOA with Ga_2O_3 surface in a bidentate or bridging configuration, which facilitates direct PFOA decomposed by h_{vb}^+ (Fig. 2.5).

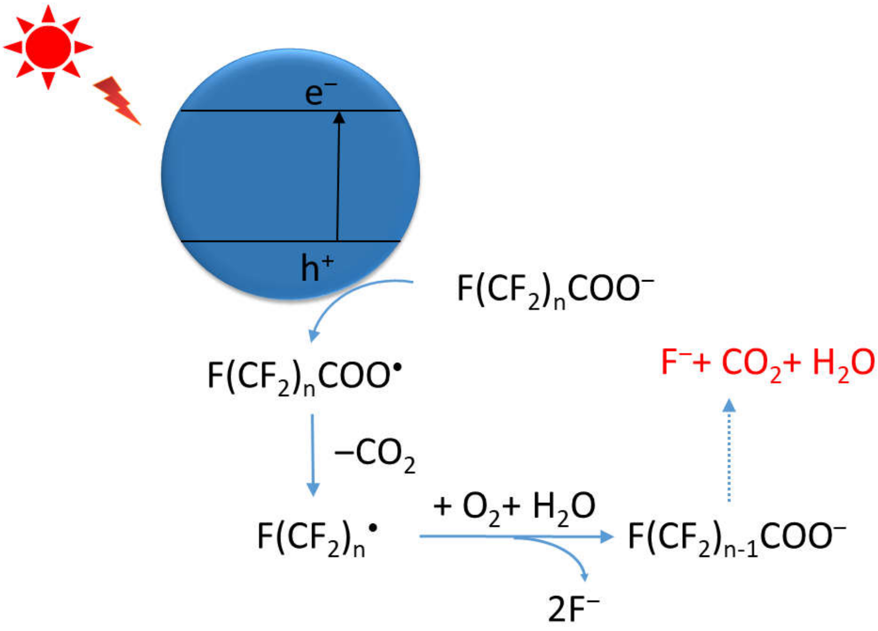

Figure 2.5 Schematic illustration of PFOA decomposition by Ga_2O_3 under UV light irradiation

BiOCl also demonstrated good performance for the photocatalytic degradation of PFOA. Ovs-controllable BiOCl nanosheets were facilely synthesized via a hydrolysis method, and applied to degrade PFOA. When Ovs ratio in BiOCl nanosheets increased from 0.573 to 0.981 by changing the alkali source applied for preparation, the efficiencies of degradation and defluorination of PFOA increased by 3–4 times. The photocatalytic decomposition of PFOA over BiOCl is dominated by the direct hole oxidation process(Song et al. 2017). A linear relationship was observed between the Ovs level in BiOCl and the photocatalytic decomposition efficiency of PFOA (Song et al. 2019). The presence of Ovs in semiconductors can not only narrow the band gap to facilitate photo absorption (Ye et al. 2011). But also promote the separation of charge carriers by trapping e_{cb}^{-}, thus promoting efficient h_{vb}^{+} oxidation (Liu et al. 2009). Moreover, Ovs can serve as adsorption sites for PFCs and consequently promote the oxidation of target pollutants by photo-generated h_{vb}^{+} (Song et al. 2019). Surface defective BiOCl was also synthesized and used for efficient photocatalytic defluorination of PFOA using sunlight as the energy source (Sun et al. 2019).

The application of BiOX in photocatalytic mineralization of persistent organic pollutants still suffers from drawbacks such as mismatch among the large band gap, wide spectral response and weak oxidizing capability of h_{vb}^{+} (Liu et al. 2015, Qin et al. 2016). Halogen doping was an effective way to adjust the band structures of bismuth oxyhalide to achieve optimal photocatalytic activity(Gnayem and Sasson 2013). Facet regulation is another efficient method to enhance the activity of a photocatalyst. A high (001) facet exposed $BiOI_{0.95}Br_{0.05}$ was successfully prepared by doping bromine via solvothermal method, and possessed remarkably high photocatalytic ability for PFOA degradation under UV light irradiation. 96% of PFOA could be decomposed within 120 min and 65% of PFOA was mineralized within 180min. The reaction kinetic constant was 4.3 times higher than that using BiOI control. The photo-generated electrons and holes were responsible for PFOA decomposition(Li et al. 2019). The generated short-chain PFCAs and their evolution trends indicated that the α-carbon atom was the attack point. The degradation process of PFOA was initialized, followed by losing $-CF_2$ unit in a stepwise manner.

$BiOI@Bi_5O_7I$ p-n heterojunction photocatalysts could be facilely prepared by calcinating BiOI at 350 ℃ < T < 410 ℃(Wang et al. 2019a). The rate constant for PFOA decomposition by $BiOI@Bi_5O_7I$ p-n heterojunction calcinated at 390 ℃ (T-390) was four times higher than that of pristine BiOI ($k = 0.061\ h^{-1}$) and 1.2 times higher than that of Bi_5O_7I (prepared at 410 ℃, $k = 0.206\ h^{-1}$). T-390 also possessed excellent mineralization ability for PFOA with about 60% of total organic carbon removed after 6 h of irradiation. EPR results and active species scavenging experiments demonstrated that $OH^{\bullet}$ was largely responsible for photodegradation of PFOA in this system, followed by $O_2^{\bullet-}$ and h_{vb}^{+}. Attacked by these active species, PFOA was gradually mineralized by losing CF_2 units.

Monoclinic $BiPO_4$, a novel $Bi_3O(OH)(PO_4)_2$ (BOHP) catalyst of wide band gap semiconductor, were applied for the degradation of PFOA under ultraviolet irradiation.

BOHP microparticles achieved dramatically faster rate in PFOA degradation and mineralization compared to $BiPO_4$ and a β-Ga_2O_3 nanomaterial catalyst, which have smaller surface area and lower band gap energy. The rate constant of BOHP for PFOA degradation in a pure water solution was ~15 times higher than those of both BiPO4 and β-Ga_2O_3. The superior performance of BOHP was primarily related to the surface charge, facilitating the adsorption behavior of PFOA onto the catalyst. The favorable redox potentials of BOHP charge carriers also contributed to the enhanced PFOA decomposition(Sahu et al. 2018). Carbon sphere (CS) modification could enhance the performance of bismuth phosphate composite (BiOHP/CS) (Xu et al. 2020c). > 99% of PFOA could be adsorbed by BiOHP/CS in 2 h, and subsequently, almost completely decomposed in 4 h of UV irradiation with a defluorination ratio of 32.5%. The PFOA degradation rate was ~18 times higher than that by neat BiOHP. The carbon modification can not only enhance the adsorption capacity of PFOA, but also facilitate a side-on adsorption configuration of PFOA with the active sites, which would promote photocatalytic cleavage of C–F bonds. Moreover, CS could enhance the stability of BiOHP by accepting photo-induced e_{cb}^- to suppress photo-corrosion of the composite.

Tungstic heteropolyacid ($H_3PW_{12}O_{40}$, HPW) demonstrated good performance for the photodegradation of PFOA. But it is worth noting that HPW has small specific surface area, which would limit its application to a large extent. You et al. synthesized HPW/biomodal mesoporous silica (BMS) catalyst and employed it as photocatalyst for PFOA degradation under VUV light irradiation(You et al. 2018). BMS possessed large specific surface area (1000 $m^2\ g^{-1}$), and provided sufficient surfaces for the dispersion of HPW, which could make more active sites exposed for PFOA decomposition. VUV/HPW/BMS system was efficient for PFOA defluorination.

Boron nitride (BN) was reported to degrade PFOA under 254 nm light irradiation (Duan et al. 2020). Scavenging experiment results indicated that PFOA degraded in a hole-initiated reaction pathway in the presence of BN, which is similar to the TiO_2 case, and ROS species (i.e., $O_2^{\bullet-}$, $OH^{\bullet}$) also participated in the degradation process. BN was ~2 and ~4 times more active than TiO_2, before and after ball milling the material. The reason may be that edge defects or B or vacancies help to enhance light absorption. Moreover, BN demonstrated good stability, showing no decrease in activity over three cycles. BN was also active for the photocatalytic degradation of GenX.

However, few semiconductor photocatalysts are found to efficiently degrade PFOA under mild solar irradiation. MnO_x is deposited on the surface of In_2O_3 to enhance ROS generation. Ovs generated on the surface of In_2O_3 paly critical roles to assist PFOA adsorption. The MnO_x-modified oxygen-vacancy-rich In_2O_3 photocatalyst possesses a significantly improved photodegradation and defluorination activity for PFOA under solar light irradiation compared to the pristine In_2O_3. Enhanced PFOA adsorption ability and ROS generation efficiency contribute to the improved performance of MnO_x-modified In_2O_3.

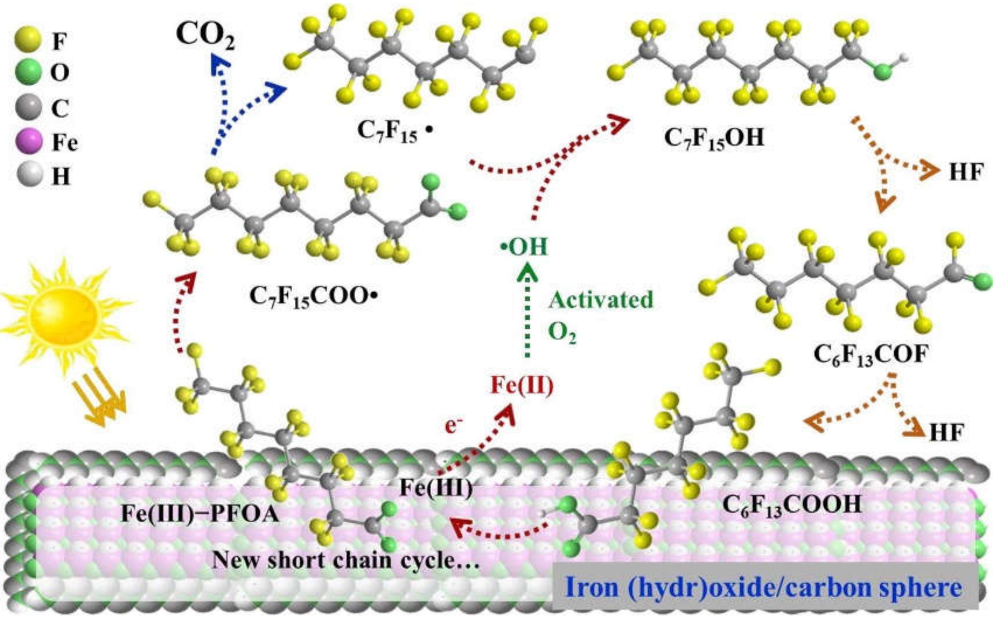

Figure 2.6 Proposed pathway of PFOA degradation by FeO/CS under solar light(Xu et al. 2020b).

Iron (hydr) oxides and carbon spheres (FeO/CS) was prepared via a one-step hydrothermal method(Xu et al. 2020b). FeO/CS showed good performance for adsorbing and then degrading the pre-sorbed PFOA under simulated solar light (Fig. 2.6). FeO/CS (1:1), derived from Fe/glucose mixture with a molar ratio of 1:1, possessed the highest PFOA adsorption capacity and photoactivity. FeO/CS (1:1, 1.0 g/L) adsorbed nearly 200 μg/L of PFOA within 1 h, and 95.2% of pre-concentrated PFOA was photodegraded in 4 h at neutral pH with a defluorination rate of 57.2%. There were two reasons for the good performance of FeO/CS. On one hand, CS facilitated formation of ferrihydrite, enabling adsorption of PFOA onto FeO/CS via binuclear and bidentate binding. On the other hand, the hybrid FeO-CS structure promoted multi-point, corporative adsorption of PFOA, which could benefit direct electron extraction from PFOA under solar light irradiation.

A novel adsorptive photocatalyst, Fe/TNTs@AC, was prepared based on commercial activated carbon (AC) and titanate nanotubes (TNTs) (Li et al. 2020b). Fe/TNTs@AC demonstrated synergistic adsorption and photocatalytic activity for rapid and efficient degradation of PFOA in aqueous solution. Fe/TNTs@AC was able to adsorb PFOA within a few minutes, thereby effectively concentrating PFOA on the photoactive sites. More than 90% of the pre-concentrated PFOA could be degraded in 4 h by Fe/TNTs@AC under UV irradiation, with a defluorination ratio of 62%. Fe/TNTs@AC was also regenerated by the efficient photodegradation of pre-concentrated PFOA and showed no significant difference in the performance for PFOA adsorption and degradation. The cooperative adsorption modes of α-Fe_2O_3 particles and AC for PFOA allowed PFOA to be adsorbed on the surface of Fe/TNTs@AC in the parallel orientation (side-on), with both tail and carboxylate group of PFOA anchored on the photocatalyst. The closer contact between PFOA and photocatalyst is conducive to PFOA decomposition by photo-generated h_{vb}^+. This study offers a “concentrate-&-destroy” strategy for efficient decomposition of PFOA, which is potential to degrade PFOA, and other PFCs in real wastewater, more cost-effectively.

EPR spin-trapping experiments could be applied for identifying reactive radicals generated in the photocatalytic processes. TEMPO (2,2,6,6-tetramethylpiperidine-N-oxyl) could be used as the radical scavenger of photo-induced e_{cb}^- and h_{vb}^+ (Peng et al. 2020). DMPO (5,5-dimethyl-1-pyrroline-N-oxide) is used as the trapping agent for the detection of $OH^\bullet$ and $^\bullet O_2^-$. The detection of $^\bullet O_2^-$ should be conducted in methanol dispersion, and in aqueous solution for the detection of $OH^\bullet$(Chen et al. 2017). TEMP (2,2,6,6-tetramethylpiperidine) is selected as the trapping agents to examine $^1O_2$ generation (Wang et al. 2016). For active species scavenging experiments, *tert*-butanol (*t*-BuOH), EDTA-Na_2, benzoquinone (BQ) and sodium azide (NaN_3) are used as scavengers of $OH^\bullet$, holes, $^\bullet O_2^-$ and $^1O_2$ (Xu et al. 2019) (Wang et al. 2016). $S_2O_8^{2-}$ can effectively consume the hydrated electrons as an electron scavenger (Yamazaki et al. 2001).

To enhance the amount of h^+ available for PFOA degradation, photocatalysts have been combined with other semiconductors or graphene to improve its photocatalytic activity for PFOA degradation to decrease the recombination of photo-induced h^+-e_{cb}^-. CeO_2-doped In_2O_3 ($x CeO_2/In_2O_3$) were synthesized and used for PFOA photocatalytic degradation(Jiang et al. 2016). The as-prepared $x CeO_2/In_2O_3$ showed much higher photocatalytic activity than CeO_2 and In_2O_3 under UV light irradiation. The excellent photocatalytic activity of 0.86%CeO_2/In_2O_3 was ascribed to the effective separation of photo-induced e_{cb}^{-}- h_{vb}^{+} promoted by charge transfer between CeO_2 and In_2O_3. In_2O_3-graphene composites were also synthesized and demonstrated enhanced activity for the photodecomposition of PFOA(Li et al. 2013a). Graphene was deposited on the surface of In_2O_3 via a sonication-assisted solution method followed by heat treatment. The coverage percentage of graphene on In_2O_3 could be adjusted by changing calcination temperature. The In_2O_3-graphene composites without calcination was compactly covered by graphene but showed lower photocatalytic activity than In_2O_3 nanoparticles. After heating In_2O_3-graphene composites at 400 ℃, the surface of In_2O_3 nanoparticles was partly enwrapped by graphene and demonstrated enhanced activity for photocatalytic decomposition of PFOA. The increased exposed surface of In_2O_3-graphene composites should be the predominant reason for providing more adsorption sites for PFOA. In addition, some researchers demonstrated that graphene could carry excited electrons from the semiconductor to the electron acceptor due to the role of electron shuttling, resulting in efficient photogenerated e_{cb}^{-}-h_{vb}^{+} pairs separation(Zhang et al. 2010a).

BiOCl/Zn-Al hydrotalcite (B-BHZA) photocatalyst was prepared and applied for the photocatalytic degradation of PFOA(Yang et al. 2020b). Over 90% of PFOA could be removed in 6 h under UV light at an optimal pH of 2. The hybrid structure of B-BHZA promoted the separation of photogenerated carriers, thus facilitating the direct hole oxidation of PFOA.

The operation parameters (e.g., pH) also have significant impact on the adsorption capacity of semiconductors for PFOA. With a pK_a of 2.8 in water (Goss 2008), PFOA was completely deprotonated even at a pH of 4; The surface of photocatalyst is positively charged, when solution pH < the pH point of zero charge (pH_{PZC}) of photocatalyst, and negatively charged at pH > pH_{PZC}. Therefore, enhanced adsorption of PFOA on photocatalysts could be realized, when solution pH is smaller than pH_{PZC} and conducive to PFOA ionization. Heavily acidic and alkaline conditions are not conducive to the decomposition of PFOA. For instance, higher defluorination rate of 38% was obtained at pH 4 in the VUV/HPW/BMS system (You et al. 2018). More positively charged BOHP surfaces at acidic conditions facilitated electrostatic attraction of $CF_3(CF_2)_xCOO^{-}$, thus enhancing its photocatalytic efficiency for PFOA degradation (Sahu et al. 2018). The presence of perchloric acid could increase the chances of perfluorocarboxylic anions to be oxidized by the h_{vb}^{+} of excited TO_2 (Panchangam et al. 2009). Heterogeneous photocatalytic treatment achieved more than

99% decomposition with a defluorination efficiency of 38% of PFOA in 7h, in the presence of perchloric acid. The photocatalytic system with 0.15 M perchloric acid in conjunction with optimum TiO_2 loading of 0.66 g L^{-1} exhibited optimal performance.

2.3 Mechanisms for the photocatalytic degradation of PFOA

2.3.1 Photo-oxidative degradation of PFOA

An e^{-}–h^{+} pair is generated, after the photocatalyst absorbs a photon with energy exceeding its bandgap energy. In the oxidation process (Fig. 2.7), photo-generated h^{+} is the primary active species. The h^{+} initiates the decarboxylation of PFOA forming perfluoroalkyl radicals ($C_7F_{15}^{\bullet}$) (Hori et al. 2003, Hori et al. 2008). $C_7F_{15}^{\bullet}$ radicals are prone to react with H_2O and O_2 or ${}^{\bullet}OH$ to form an unstable alcohol $C_7F_{15}OH$. The $C_7F_{15}OH$ would then undergo HF elimination generating $C_6F_{13}COF$. The $C_6F_{13}COF$ undergoes hydrolysis to generate PFHpA with one CF_2 unit removed from PFOA. Then, PFHxA, PFPeA, PFBA, PFPrA, and TFA are generated step wisely following the same pathway. Finally, PFOA would be mineralized to F^{-} and CO_2, ideally.

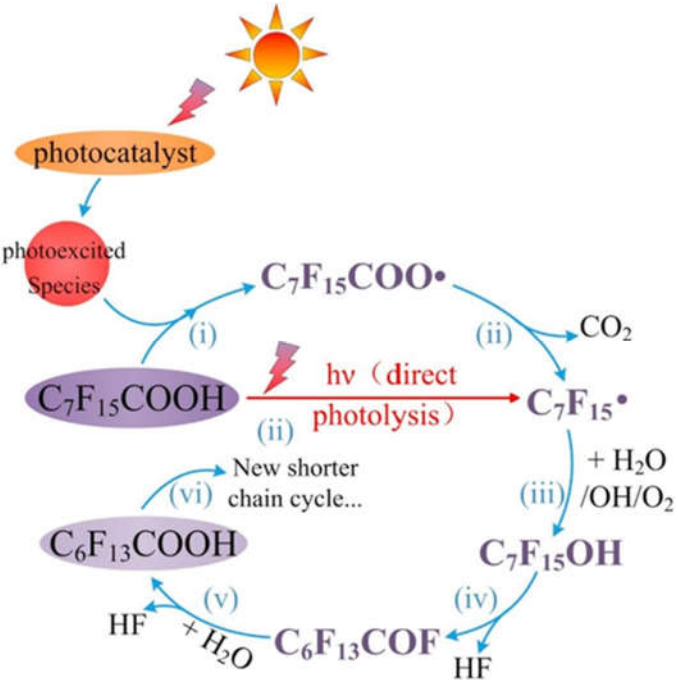

Figure 2.7 Pathway for photo-oxidative degradation of PFOA (Wang et al. 2017b).

2.3.2 Photo-reductive degradation of PFOA

Figure 2.8 presents the photo-reductive degradation of PFOA. In this process, the photo-induced e_{cb}^{-} is the primary active species. Firstly, the e_{cb}^{-} will attack the fluorine atom at α-position. The fluorine atom is eliminated to generate $C_7F_{14}HCOOH$ and $C_7F_{13}H_2COOH$. $C_7F_{13}H_2COOH$ would then generate $C_6F_{13}^{\bullet}$ radical, $^{\bullet}COOH$ radical and CH_2 carbene. $C_6F_{13}^{\bullet}$ radical and $^{\bullet}COOH$ radical may connect to form $C_6F_{13}COOH$, which would be further degraded in the same way (Wang et al. 2017b).

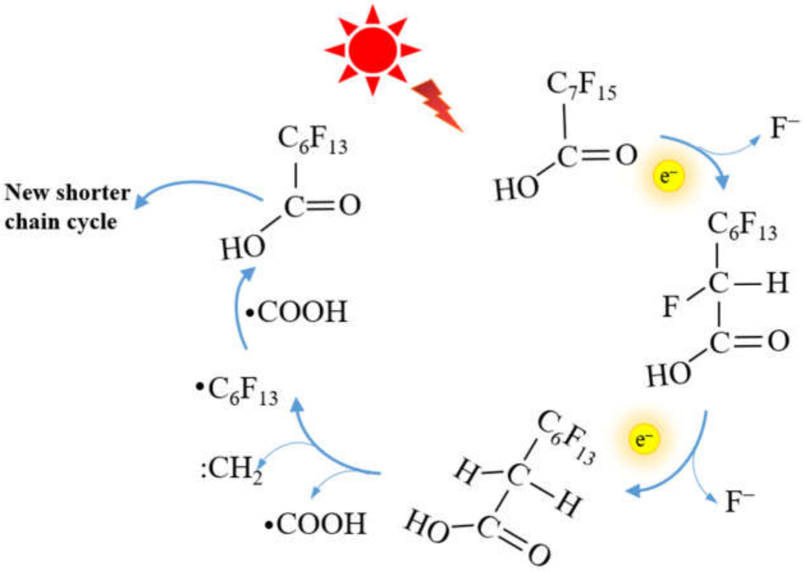

Figure 2.8 Possible photo-reductive degradation pathway of PFOA.

2.4 Conclusion

For heterogeneous photocatalytic processes degrading PFCs, various photocatalysts have been developed. Their instinct properties benefiting PFCs removal are discussed. A linear relationship is obtained between the photocatalytic degradation efficiency of PFOA and the Ovs amount in photocatalysts. Photo-induced e_{cb}^{-} and h^{+} are reactive species of photo-oxidative and photo-reductive approaches for PFOA removal, respectively. And strong binding between PFOA and semiconductor is beneficial for its decomposition. Adjusting aqueous pH and the surface properties of photocatalysts, such as higher Ovs level could benefit the adsorption of PFOA towards photocatalysts, further enhancing its decomposition.

CHAPTER 3

Experimental methods

3.1 Introduction

This chapter consists of materials, characterizations of as-prepared photocatalysts, as well as analysis methods of aqueous samples in the series of experiments (Chapter 4 – 7) during the whole research period.

3.2 Materials

All the reagents were purchased from Sigma-Aldrich and used without further purification. N,N-dimethylformamide (DMF, anhydrous, 99.8%), benzene-1,4-dicarboxylic acid (BDC), PFOA ($C_7F_{15}COOH$, 95%), perfluoroheptanoic acid ($C_6F_{13}COOH$, PFHpA, 99%), perfluorohexanoic acid ($C_5F_{11}COOH$, PFHxA, 97%), perfluoropentanoic acid (C_4F_9COOH, PFPeA, 97%), perfluorobutanoic acid (C_3F_7COOH, PFBA, 98%), pentafluoropropionic acid (C_2F_5COOH, PFPA, 97%), and trifluoroacetic acid (CF_3COOH, TFA, 99%). The $In(OH)_3$ was purchased from Sigma-Aldrich. All chemicals are used as received without further purification.

3.3 Characterizations

3.3.1 X-ray Diffraction

X-ray diffraction (XRD) is recorded to investigate the crystal structures of as-synthesized semiconductor photocatalysts. The crystal structure of photocatalysts could be identified by indexing to the standard PDF card in Joint Committee on Powder Diffraction Standards (JCPDS) database. In_2O_3 samples in Chapter 4 and 5 are characterized by XRD (Siemens D5000) for their crystalline structure (Cu Kα, λ = 1.54059 Å). The photocatalysts studied in Chapter 6 and 7 are collected on XRD (Bruke D8 Advance) from 10° to 80°.

3.3.2 Scanning electron microscopy

Scanning electron microscopes (SEM) are applied to observe the morphologies of the photocatalysts and element percentages (equipped with energy dispersive X-ray spectroscopy, EDS) of synthesized catalysts. The morphologies of In_2O_3 samples in Chapter 4 and 5 are measured by a scanning electron microscopy (SEM, Zeiss Supra 55VP, Carl Zeiss AG). The morphologies of BiOX and BiOX/TiO_2 catalysts in Chapter 6 are observed by scanning electron microscopy (SEM, Zeiss Sigma 300).

3.3.3 Transmission electron microscopy

Transmission electron microscopy (TEM) is applied to observe the nanostructures as-prepared photocatalysts. High-resolution TEM (HRTEM) is recorded to investigate the lattice fringes of the semiconductors. In addition, the selected area electron diffraction (SAED) can be used to investigate the phase characteristics (crystalline or amorphous) of the as-prepared photocatalysts. Transmission electron microscopy (TEM, JEM-2100, JEOL Co. Ltd., Japan) were recorded to observe the microscopic morphology of the samples.

3.3.4 X-ray photoelectron spectroscopy

X-ray photoelectron spectroscopy is used to investigate the composition, quantity and state of surface elements. XPS spectra can provide information of the relative quantification and the valence states of constituent elements in the materials. The valence states of the elements can be estimated from the binding energies. XPS of as-synthesized photocatalysts are recorded on the X-ray photoelectron spectroscopy (XPS, ESCALab 250Xi, Thermo Fisher) with C as the internal standard (C1s = 284.8 eV).

3.3.5 UV-vis absorption spectroscopy

The UV-Vis absorption spectra of as-prepared photocatalysts were recorded on a 950 UV/Vis-NIR spectrophotometer (Perkin Elmer Lambda). $BaSO_4$ is used as a reference.

3.3.6 Photoluminescence spectroscopy

Room-temperature photoluminescence (PL) spectra are collected on an Edinburgh FLS1000/FS5 luminescence spectrometer. The PL spectra are collected to investigate the recombination of the photogenerated hole with oxygen-deficient defect centers in In_2O_3 samples.

3.3.7 High angle annular dark field-scanning transmission electron microscopy images

High angle annular dark field (HAADF)-scanning transmission electron microscopy (STEM) images (Themis Z, Thermo scientific) are recorded to observe the morphologies of prepared materials.

3.3.8 Extended X-ray absorption fine structure spectroscopy

Extended X-ray absorption fine structure spectroscopy (EXAFS) is applied to identify the structure of Bi SAs. The XANES spectra (C K-edge and N K-edge) were measured at beamline BL12B of National Synchrotron Radiation Laboratory (NSRL) of China. The samples were deposited onto double-sided carbon tape for analysis on the X-ray spectroscopy. XAFS measurement and data analysis: XAFS spectra at the Bi L-edge was collected at BL14W1 station in Shanghai Synchrotron Radiation Facility (SSRF). The Bi L-edge XANES data were recorded in fluorescence mode.

3.3.9 N_2 sorption/desorption measurement

A surface-area pore analyzer (NOVA-2200e, Quantachro) is used to determine the specific surface areas (SSAs) by N_2 sorption/desorption. Other critical parameters (e.g., pore size, pore volume) could also be obtained from the N_2 sorption/desorption analysis.

3.4 Photocatalytic degradation of PFOA

The photocatalytic degradation of PFOA in Chapter 4 was carried out in a cylindrical reactor vessel. 200 mL of PFOA aqueous solution (initial concentration of 10 mg L^{-1}) and 40 mg catalyst were mixed and stirred in dark for 30 min to achieve adsorption equilibrium. A 32-W UV lamp of 254 nm wavelength (Nbet Co. Ltd., Beijing, China) was used as the light source. The irradiation intensity was 3.5 mW cm^{-2} as measured by a UV intensity meter (ST-512). During the reaction, the solution and photocatalyst were well mixed by magnetic stirring. At regular time intervals, 2 mL of samples were taken and filtered through a filter (Puradisc syring fiter, 0.2 μm, Whatman) for further analysis. The photocatalytic degradation of PFOA in Chapter 5-7 was carried out in a cylindrical reactor vessel with a quartz cap. The volume of the photoreactor was 160 mL, with a height of 8 cm, and the irradiated area was 20 cm^{-2}. The irradiation power received on the surface of the photoreactor was 4.0 mW cm^{-2}. The pH of PFOA solution (10 mg L^{-1}) was 4.85. 100 mL of PFOA solution (10 mg L^{-1}) and a certain amount of In_2O_3 were mixed in the reactor, the mixture was then stirred in dark for 30 min to achieve adsorption-desorption equilibrium. Afterwards, the 254 nm UV light was turned on and 2 mL solution was taken at certain times. Lastly, the sample was filtered for further analysis of PFOA concentration and fluoride ion concentration. The samples were taken at regular times, filtered and then diluted by 20 times. External standards were applied for the quantification of PFOA and its degradation intermediates. The concentration limit of PFOA and its degradation intermediates were in the range of 0.5-500 μg L^{-1}.

3.5 The analysis of PFOA and the degradation intermediates

3.5.1 The analysis of PFOA and its degradation intermediates

The concentration of PFOA and its degradation intermediates in Chapter 4 were analyzed by a triple quadrupole ultra-high-performance liquid chromatograph tandem mass spectrometer (UHPLC-MS/MS) from Shimadzu (model 8060) equipped with a binary pump and a Shim-pack column (1.6 μm, 2.0 mm × 50 mm). The mobile phase was a binary mixture of A (Milli-Q water) and B (methanol) at a flow rate of 0.4 mL min^{-1}. The elution gradient started with 50% B for 2.5 min, then 100% B for the next 1 min followed by 50% B for another 1.5 min. The total running time of this method was 5 min. The injection volume of samples was 1 μL. The tandem mass analysis was conducted in a multiple reaction monitoring (MRM) mode. For PFOA, m/z 169.1 and m/z 219.0 are used as the qualitative ions and m/z 369.0 is used as the quantitation ion to avoid mass interference. The tandem mass analysis conditions of the PFOA and its degradation intermediates are listed in Table 3.1.

Table 3.1 The target compounds of PFOA and its degradation products, and their MS/MS parameters.

Acronym	Name	Formula	MS/MS mass transition	Cone voltage (V)	Collision energy (eV)
PFOA	Perfluorooctanoic acid	$C_7F_{15}COOH$	412.90 → 369.00	20	10
PFHpA	Perfluoroheptanoic acid	$C_6F_{13}COOH$	363.00 → 319.00	2.6	22
PFHxA	Perfluorohexanoic acid	$C_5F_{11}COOH$	313.00 → 269.00	2.6	8.4
PFPeA	Perfluoropentanoic	C_4F_9COOH	262.55 →	2.6	8.4

	acid		219.10		
PFBA	Perfluorobutyric acid	C_3F_7COOH	212.20 → 169.10	2.6	10.0
PFPrA	Pentafluoropropionic acid	C_2F_5COOH	162.9 → 118.8	12.0	7.0
TFA	Trifluoroacetic acid	CF_3COOH	112.9 → 68.9	12.0	7.0

The concentration of PFOA and its degradation intermediates in Chapter 5-7 were analyzed by a high-performance liquid chromatography-tandem mass spectrometry (HPLC-MS/MS, Agilent). Agilent 1260 series equipped with a Poroshell 120 EC-C18 reversed-phase column (3 ×100 mm, 2.7 μm, Agilent) were employed to separate PFOA and its decomposition intermediates. Mass spectrometric analysis was performed under the multiple reaction monitoring (MRM) mode with negative electrospray ionization. Solvent A (methanol) and solvent B (0.1 % formic acid aqueous solution) were used as the mobile phase. The elution gradient was set as follows: 0-8.0 min, solvent A increased from 30% to 90%; 8.0-10.0 min, held solvent A at 90%; 10.0-13.0 min, solvent A incrreased from 90% to 100%; 13.0-15.0 min, held this proportion; 15.0-15.5 min, the gradient of solvent A decreased from 100% to 30%. The method on mass spectrometry was listed Table 3.2.

Table 3.2 The target compounds of PFOA and its degradation products, and their MS/MS parameters.

Acronym	Name	Formula	MS/MS mass transition	Collision energy (eV)	Fragmentor (V)	Cell Accelerator Voltage (eV)
PFOA	Perfluorooctanoic acid	$C_7F_{15}COOH$	413.3 → 369.1	1	110	3
PFHpA	Perfluoroheptanoic acid	$C_6F_{13}COOH$	362.6 → 319.1	1	80	3
PFHxA	Perfluorohexanoic acid	$C_5F_{11}COOH$	313.0 → 269.1	1	70	3
PFPeA	Perfluoropentanoic acid	C_4F_9COOH	262.6→ 219.2	1	70	3

3.5.2 The analysis of fluoride ion

The concentration of the fluoride ion was detected by a Dionex ICS-600 IC system.

The defluorination ratio of PFOA is an important indicator of the decomposition of PFOA.

3.6 Photoelectrochemical measurements

Electrochemical impedance spectroscopy (EIS) experiments were conducted employing a three-electrode system in a 0.02 M Na_2SO_4 solution. ITO was thoroughly washed with ethanol and water for several times before use. Each In_2O_3 (10 mg) sample was firstly dispersed in 0.7 ml ethanol by sonication for 1 h, and then coated on ITO glasses evenly and dried at the ambient temperature. The coated ITO glass served as the working electrode with an effective geometric coating area of 1.5×2 cm^2. Ag/AgCl electrode and Platinum wire were used as the reference electrode and counter electrode, respectively. The measurements were carried out on a CHI-760E (CH Instrument Co., China) electrochemical workstation at a frequency range from 0.1 Hz to 1.0×10^6 Hz.

CHAPTER 4

Facile preparation of hydrophilic In_2O_3 nanospheres and rods with improved performances for photocatalytic degradation of PFOA

4.1 Introduction

Perfluorinated chemicals (PFCs) have been extensively used as refrigerants, adhesives, insecticides, fire retardants, and surface treatment agents in photolithography(Trojanowicz et al. 2018). These chemicals are very stable because of the strong carbon-fluorine (C–F) bond with the high bonding energy of 544 kJ/mol(Xu et al. 2017a), giving rise to the environmental persistence and bioaccumulative nature(Cui et al. 2020). Some of PFCs, especially perfluoroctanoic acid (PFOA), are globally distributed and have been ubiquitously detected in water, animals and human beings(Wang et al. 2017b). Developmental and reproductive toxicities, liver damage, thyroid disease and possible cancer would be caused by the exposure to PFOA(Lau et al. 2007). Due to its chemical inertness, most conventional approaches including biological and chemical methods are ineffective to destruct PFOA(Wu et al. 2019b).

Heterogeneous photocatalysis appears to be an efficient and mild method to purify various pollutants including halogenated organics(Herrmann 1999, Sahu et al. 2018). Although TiO_2 can readily photodegrade diverse organic pollutants, it demonstrated a low activity for degrading PFOA under mild conditions; thus harsh reaction conditions are required such as highly acidic conditions (pH 1)(Li et al. 2016b, Zhong et al. 2019). Therefore, significant efforts have been dedicated to developing efficient photocatalysts with a relativly large bandgap corresponding to a sufficient redox potential for PFOA degradation. Indium oxide (In_2O_3) is appealing for direct photocatalytic degradation of PFOA(Li et al. 2012c, Xu et al. 2017a).

In_2O_3 was typically obtained by the calcination of indium hydroxide ($In(OH)_3$)(Li et al. 2013c). Developing a synthetic method for synthesizing In_2O_3-based materials with on-demanding structures and properties is essential and significant(Cho et al. 2009). Considering the flexible and porous structures of metal-organic frameworks (MOFs)(Lee et al. 2009, Nie et al. 2017), In-based MOF may serve as a good precursor for In_2O_3. MOFs constituted by the coordination of metal ions and organic ligands enables great flexibility for preparation of functional materials with diverse structures and functions(Long and Yaghi 2009). MOFs can be employed as versatile precursors for the facile preparation of functional MOF-derived materials(Dhakshinamoorthy et al. 2018, Yang et al. 2017). MOF-derived materials have high surface area, ordered porosities, and designable functionalities which are beneficial for their catalytic performances(Jiao and Jiang 2019).

In this study, In_2O_3 was prepared by the calcination of Indium (III)-benzenedicarboxylate (In-BDC) MOF. In-BDC derived In_2O_3 was firstly used for the degradation of PFOA under 254 nm UV light irradiation and demonstrated superior performances. Multiple characterizations and together with the degradation results of PFOA help to elucidate why In-BDC derived In_2O_3 samples show better activity than commercial In_2O_3.

4.2 Experimental section

4.2.1 Preparation of In_2O_3

In-BDC nanosphere (NS) was synthesized according to a reported method (Cho et al. 2008). $In(NO_3)_3 \bullet xH_2O$ (23.4 mg) in 1.35 mL DMF and BDC (9 mg) in 1.35 mL DMF were mixed in a 5 mL vial. The resulting mixture was heated in a water bath (100 °C) for 20 min. The generated In-BDC NS were separated by centrifugation after the reaction mixture cooled to room temperature, and washed several times with DMF and methanol. Then, the resulting In-BDC was dried at 40 °C in a vaccum drying oven. The In_2O_3 nanospheres (In_2O_3 NS) were obtained by calcination of In-BDC at 550 °C for 45 min with a heating rate of 3 °C/min.

NaOAc (sodium acetate) was used to ajust the morphology of In-BDC, and In-BDC rods were synthesized. 2 mmol of $In(NO_3)_3 \bullet xH_2O$ and 2 mmol BDC were dissolved in 10 mL DMF separately and mixed, then 100 µL of 0.04 M NaOAc aqueous solution was added with vigorous stirring (Jin et al. 2013). The resulting mixture was heated in a water bath (100 °C) for 30 min. The generated In-BDC rods were separated by centrifugation, and washed several times with distilled water and ethanol, which were then dried in a vaccum drying oven at 40 °C. Then the obtained In-BDC complexes were calcinated at 500 °C for 1 h with a heating rate of 2 °C min^{-1} to prepare In_2O_3 rods.

4.2.2 Characterization

The morphology of In-BDC derived In_2O_3 and commercial In_2O_3 were measured by a scanning electron microscopy (SEM, Zeiss Supra 55VP, Carl Zeiss AG). In_2O_3 samples were characterized by X-ray diffraction (XRD) (Siemens D5000) for their crystalline structure (Cu Kα, $\lambda = 1.54059$ Å). A sessile drop method utilizing Theta Lite

100 (Attension, Sweden) was employed to measure the contact angles of In_2O_3 samples(Ren et al. 2019). The In_2O_3 (10 mg) powders were firstly dispersed in 0.7 mL ethanol and the solution was sonicated for 1 h and then evenly coated on an indium tin oxide (ITO) glass. A water droplet around 5 µl released from a needle tip was dropped onto the ITO glass coated with In_2O_3 samples. Photos were taken at a rate of 12 frames/s with a motion camera. The contact angle experiments were conducted in duplicate and the average value was taken. X-ray photoelectron spectroscopy (XPS, ESCALab 250Xi, Thermo Fisher) was used to investigate the composition, quantity and state of surface elements. A surface-area pore analyzer (NOVA-2200e, Quantachro) was used to determine the specific surface areas (SSAs) by N_2 sorption. Transmission electron microscopy (TEM, JEM-2100, JEOL Co. Ltd., Japan) were recorded to observe the microscopic morphology of the samples. Room-temperature electron spin resonance (ESR) spectra were obtained using an ESR spectrometer (Brucker A300). Room-temperature photoluminescence (PL) spectra were obtained from an Edinburgh FLS1000/FS5 luminescence spectrometer. UV/Vis absorption spectra of In_2O_3 samples were conducted on a Perkin Elmer Lambda 950 UV/Vis-NIR spectrophotometer. Diffuse reflectance infrared Fourier transform spectroscopy (DRIFTS) measurements were carried out on a Thermo Scientific Nicolet iS50 spectrometer equipped with an MCT detector cooled by liquid N_2. The IR spectra were recorded in the range of 2000 to 800 cm^{-1} at a resolution of 4 cm^{-1}.

Electrochemical impedance spectroscopy (EIS) experiments were conducted employing a three-electrode system in a 0.02 M Na_2SO_4 solution. ITO was thoroughly washed with ethanol and water for several times before use. Each In_2O_3 (10 mg) sample was firstly dispersed in 0.7 ml ethanol by sonication for 1 h, and then coated on ITO glasses evenly and dried at the ambient temperature. The coated ITO glass served as the working electrode with an effective geometric coating area of 1.5×2 cm^2. Ag/AgCl electrode and Platinum wire were used as the reference electrode and counter electrode, respectively. The measurements were carried out on a CHI-760E (CH Instrument Co., China) electrochemical workstation at a frequency range from 0.1 Hz to 1.0×10^6 Hz.

4.2.3 Photocatalytic decomposition of PFOA

The photocatalytic degradation of PFOA was carried out in a cylindrical reactor vessel. 200 mL of PFOA aqueous solution (initial concentration of 10 mg L^{-1}) and 40 mg catalyst were mixed and stirred in dark for 30 min to achieve adsorption equilibrium. A 32-W UV lamp of 254 nm wavelength (Nbet Co. Ltd., Beijing, China) was used as the light source. The irradiation intensity was 3.5 mW cm^{-2} as measured by a UV intensity meter (ST-512). During the reaction, the solution and photocatalyst were well mixed by magnetic stirring. At regular time intervals, 2 mL of samples were taken and filtered through a filter (Puradisc syring fiter, 0.2 μm, Whatman) for further analysis.

4.2.4 Analyses

The concentration of PFOA and its degradation intermediates were analyzed by a triple quadrupole ultra-high-performance liquid chromatograph tandem mass spectrometer (UHPLC-MS/MS) from Shimadzu (model 8060) equipped with a binary pump and a Shim-pack column (1.6 μm, 2.0 mm × 50 mm). The mobile phase was a binary mixture of A (Milli-Q water) and B (methanol) at a flow rate of 0.4 mL min^{-1}. The elution gradient started with 50% B for 2.5 min, then 100% B for the next 1 min followed by 50% B for another 1.5 min. The total running time of this method was 5 min. The injection volume of samples was 1 μL. The tandem mass analysis was conducted in a multiple reaction monitoring (MRM) mode. For PFOA, m/z 169.1 and m/z 219.0 are used as the qualitative ions and m/z 369.0 is used as the quantitation ion to avoid mass interference.

4.3 Results and discussion

4.3.1 Characterization

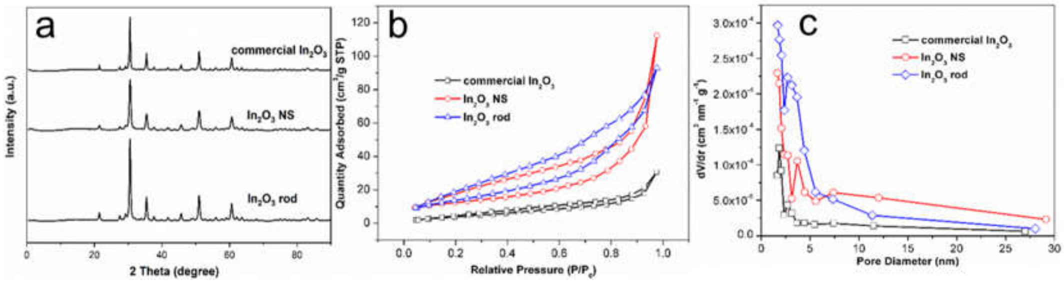

Figure 4.1 XRD patterns of commercial In_2O_3 and In-BDC based In_2O_3 (a); N_2 adsorption/desorption isotherm (b) and Barrett-Joyner-Halenda (BJH) pore size distribution plot (inset) (c) of commercial In_2O_3, In_2O_3 NS, and In_2O_3 rods.

The powder X-ray diffraction (XRD) pattern of the prepared In_2O_3 is shown in Fig. 4.1a. All the diffraction peaks could be indexed to the cubic In_2O_3 (JCPDS, No. 06-

0416), indicating that In_2O_3 is successfully prepared. In_2O_3 rods exhibit the highest crystallinity, and the peaks of In_2O_3 NS are much weaker, which may be related with the smaller size of buiding blocks of In_2O_3 NS (Li et al. 2012c).

Brunauer-Emmett-Teller (BET) gas sorptometry measurements were performed to investigate the SSA of In_2O_3 samples. Figure 4.1b shows the N_2 adsorption/desorption isotherms. The BET SSA of In_2O_3 NS and In_2O_3 rods are 43.78 and 52.86 $m^2\ g^{-1}$, respectively. SSA of commercial In_2O_3 is only 17.82 $m^2\ g^{-1}$. All three samples show the Type IV isotherm, suggesting the mesoporous structure of In_2O_3 materials (Shi et al. 2018). As shown in Fig. 4.1c, the pore size distribution is in the range of 1.5-5.0 nm. Compared with commercial In_2O_3, In_2O_3 NS and rods exhibit much larger hysteresis loops, suggesting that the MOF-derived In_2O_3 NS and rods have larger pore volumes and SSA. The relatively higher BET surface area confirms that MOF derived In_2O_3 have a porous structure. Generally, a high surface area could promote the activity due to more active adsorption and reaction centers provided (Li et al. 2014, You et al. 2018).

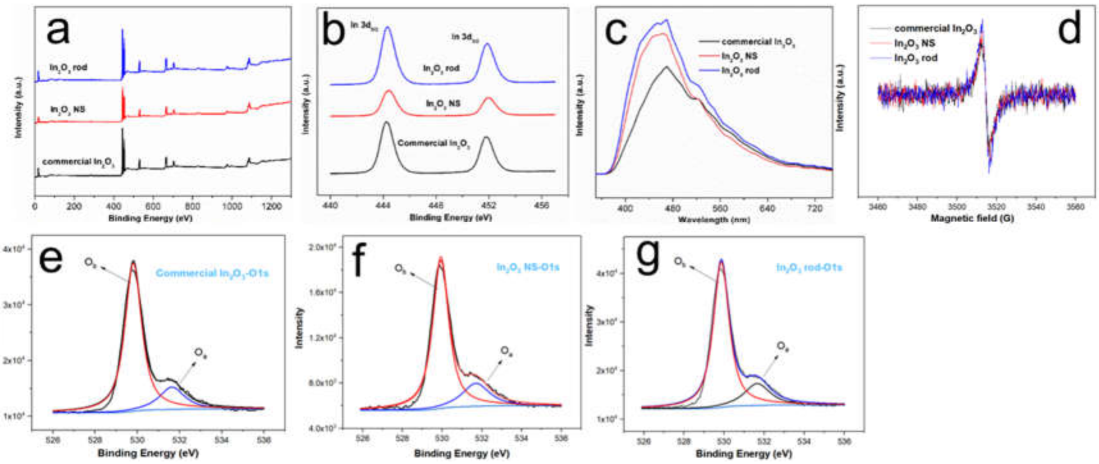

Figure 4.2 XPS survey (a), In 3d core level spectra (b), Room-temperature photoluminescence spectra (c), ESR spectra (d) and the O1s XPS spectra (e, f, g) of In_2O_3 samples.

XPS spectra were conducted to identify the surface chemistry of In_2O_3 samples. Figure 4.2a showed the full XPS spectra, which indicated O and In elements in the In_2O_3 samples. Additionally, the carbon ligands in In-BDC MOFs were completely decomposed and removed during the calcination. Two peaks situated at 444.5 and 452.0 eV in the 3d core level spectra (Fig. 4.2b) are ascribed to the characteristic spin–orbit split $3d_{5/2}$ and $3d_{3/2}$ of In. Furthermore, the high-resolution O 1s spectra can be deconvoluted into two peaks (Fig. 4.2e-g). One peak located at 529.8 eV is assigned to the oxygen bond of In-O-In, and the other at 531.4 eV is deemed as the oxygen atoms in the vicinity of oxygen vacancy (O_V)(Wang et al. 2020a). The two peaks of O 1s are assigned as O_b and O_a, and the binding energy (BE) of O_a is 1.6 eV higher than that of O_b. The O_a/O_b ratio therefore could indicate the O_V level in the material(Gan et al. 2013). The O_a/O_b values of commercial In_2O_3, In_2O_3 NS and rods are 0.224, 0.239, and 0.256, respectively. The PL emission peak at ~460 nm could be mainly attributed to the recombination of the photogenerated hole with oxygen-deficient defect centers (Cho et al. 2009, Lei et al. 2014). The PL intensities follow the order of In_2O_3 rods > In_2O_3 NS > commercial In_2O_3 (Fig. 4.2c), suggesting a little higher concentration of O_V in In-BDC derived In_2O_3. In_2O_3 samples exhibit an ESR signal at g = 2.004 (Fig. 4.2d), which could be identified as the electrons trapped on O_V(Lei et al. 2014). The signal intensity follows the order of In_2O_3 rod > In_2O_3 NS > commercial In_2O_3, indicating the slightly higher O_V concentration of MOF-derived In_2O_3 than commercial In_2O_3, which is in accordance with the PL and XPS results.

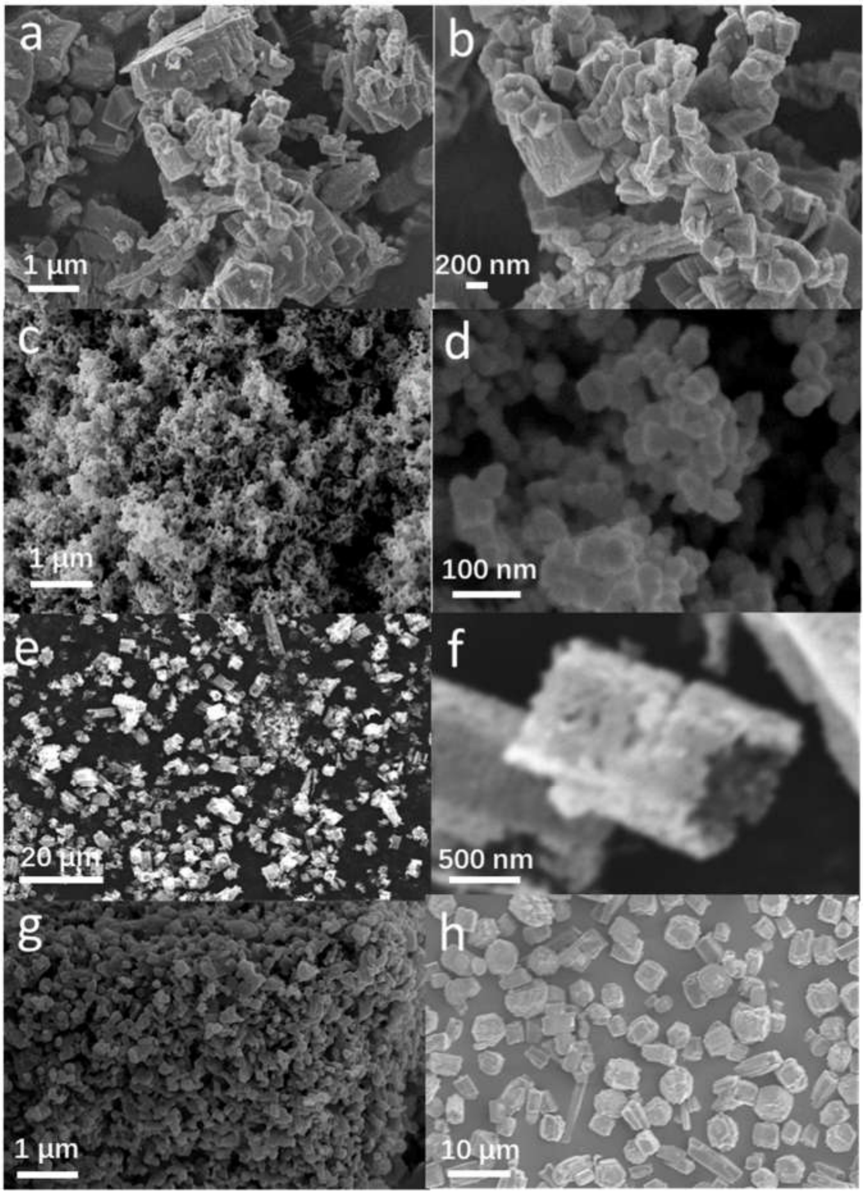

Figure 4.3 SEM images of commercial In_2O_3 (a, b), In_2O_3 NS (c, d), In_2O_3 rod (e, f), In-BDC NS (g), and In-BDC rod (h).

The morphologies of In_2O_3 samples and In-BDC complexes were characterized by SEM and TEM (Fig. 4.3 and Fig. 4.4). Typical SEM images of In_2O_3 samples demonstrate that the original shape of In-BDC is maintained when it transforms into metal oxide (Fig. 4.3). The SEM images (Fig. 4.3 e-f) and the TEM image (Fig. 4.4 g) reveal that In-BDC synthesized with the assistance of NaOAc presents uniform hexagonal rods comprised by nanocrystals. After calcination, hollow In_2O_3 is obtained in Fig. 4.4h. The hollow In_2O_3 rods were composed of numerous In_2O_3 nanocrystals within a size range of 10-30 nm (Fig. 4.4i). The TEM images (Fig. 4.4 c) reveal the ultrathin morphology of In-BDC NS, and In_2O_3 NS with a larger size of ~20-40 nm was obtained after calcination (Fig. 4.4d-e). TEM images show that In_2O_3 NS and In_2O_3 rods are constructed by the interlocking stack of nanoplates, and the single crystal property of the nanoplates is also entified. As shown in the HRTEM image of In_2O_3 NS (Fig. 4.4f), the lattice fringe revealed a planar distance of 0.297 nm in the (222) plane and 0.413 nm of the (211) plane of the cubic In_2O_3 (Cho et al. 2009).

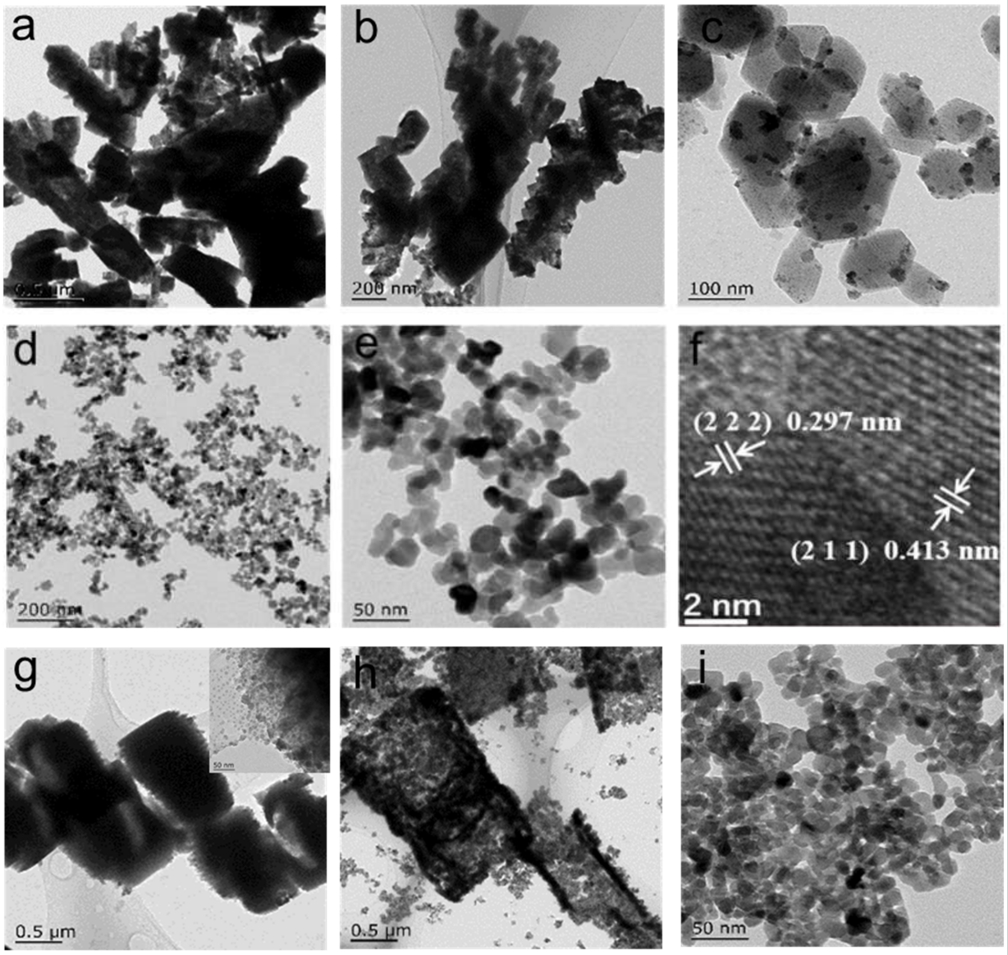

Figure 4.4 TEM images of (a, b) commercial In_2O_3, (c) In-BDC NS, (d, e) In_2O_3 NS, (f) HRTEM of In_2O_3 NS, (g) In-BDC rod, inset is the amplified TEM image of In-BDC rod, and (h, i) In_2O_3 rod.

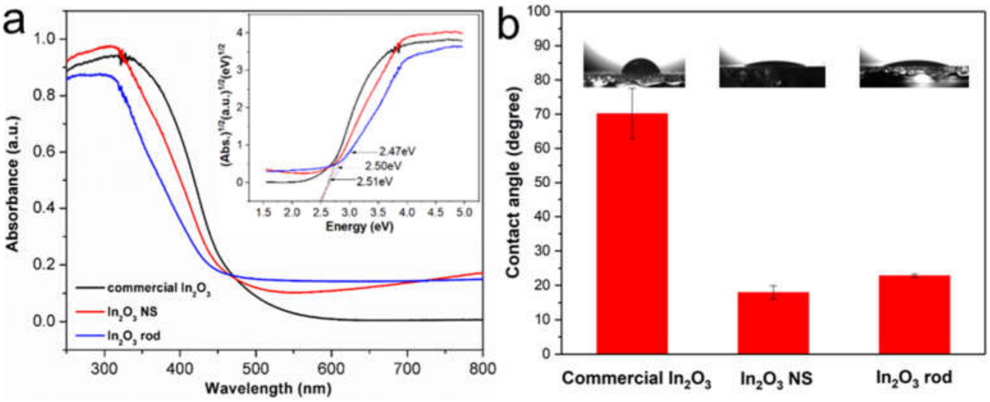

Figure 4.5 UV-vis absorption spectra of commercial In_2O_3, In_2O_3 NS and In_2O_3 rods. Inset is the bandgap of samples (a). Contact angles of commercial In_2O_3, In_2O_3 NS, and In_2O_3 rods (b).

The UV-vis absorption spectra of commercial In_2O_3, synthesized In_2O_3 NS and rods are shown in Fig. 4.5a. Blue shift in the UV-vis spectra of In_2O_3 NS may be due to the small particle size and homogeneous distribution of In_2O_3 NS, compared to the commercial In_2O_3(Bhui et al. 2009). The absorption coefficient α of the indirect transition semiconductor near the band edge can be described as $\alpha h\nu = A(h\nu - E_g)^2$, where $h\nu$ is the photo energy, and E_g is the band gap energy(Song et al. 2017). Thus, $(\alpha h\nu)^{1/2}$ versus hv is plotted. By extrapolating the straight line to the abscissa, the band gaps (Eg) of commercial In_2O_3, NS and rods are estimated to be 2.51 eV, 2.50 eV and 2.47 eV, respectively.

Contact angles of the three In_2O_3 samples are presented in Fig. 4.5b. The contact angle of commercial In_2O_3, In_2O_3 NS and rods are 70.19 ± 7.33°, 17.99 ± 1.88° and 22.84 ± 0.43°, respectively. The relatively small contact angles of In-BDC derived In_2O_3 clearly demonstrate its enhanced hydrophilicity, compared with the commercial In_2O_3. Porous morphology facilitated the liquid media to penetrate into the interior of the photocatalyst and thus lower the contact angle, which created a more hydrophilic surface in nature (Munirathinam et al. 2015). The hydrophilic nature facilitated the contact of PFOA with the In_2O_3 photocatalysts, thus enhancing the efficiency for PFOA decomposition. The increases in surface area might be a main contributor to the enhancement of photocatalytic activity (Liu et al. 2020). It is known that the hydrophobicity/hydrophilicity would significantly affect the adsorption/desorption behaviour of molecules on the catalyst surface (Yang et al. 2008). Such properties are particularly important in designing catalysts for aqueous reactions (Makowski et al.

2008).

4.3.2 Improved photochemical properties

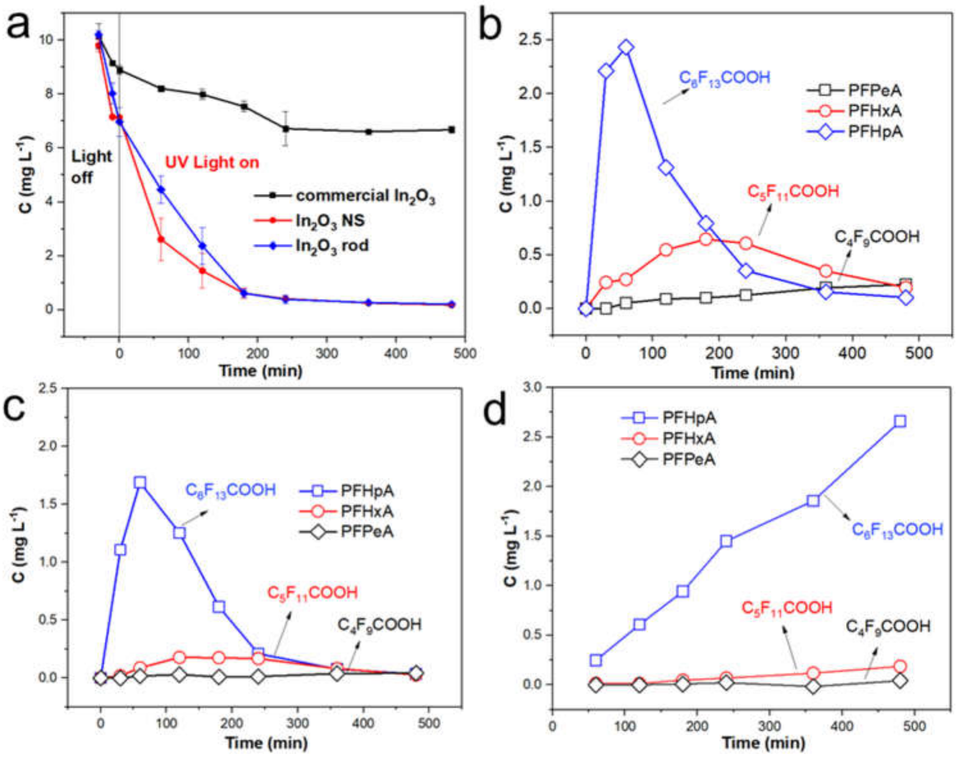

Figure 4.6 Time course of PFOA degradation over commercial In_2O_3, In_2O_3 NS, and In_2O_3 rod (a); and shorter-chain intermediates under UV irradiation in the presence of In_2O_3 NS (b), In_2O_3 rod (c) and commercial In_2O_3 (d).

Figure 4.6a demonstrates the photocatalytic degradation of PFOA by different In_2O_3. In_2O_3 NS and rods could adsorb ~ 30% of PFOA, after stirring in the dark for 30 min. Based on the preliminary experiment results, the adsorption equilibrium for PFOA was achieved within 30 min. Under the irradiation of 254 nm UV light, PFOA was completely degraded within 3 h. While only ~ 10% of PFOA was adsorbed in 30 min in dark and 35% of PFOA was removed after irradiation for 8 h in the presence of commercial In_2O_3. PFOA degradation follows the second-order reaction kinetics (Fig. S4), and the reaction constants for In_2O_3 NS, In_2O_3 rod and commercial In_2O_3 are 0.01754, 0.00901 and 7.59×10^{-5} L mg^{-1} min^{-1}. These results demonstrate that In_2O_3 NS and rods have much better efficiency for PFOA decomposition than the commercial In_2O_3. The good performances of In-BDC derived In_2O_3 are attributed to the larger SSA and mesoporous structure of In_2O_3 NS and rods. Large SSA can provide more adsorption and reaction sites, which are beneficial to the photocatalytic activity of the catalysts. The mesoporous structure could promote the diffusion of reactants and intermediates during the reaction, which is an important step in determining the reaction rate. High adsorbability for PFOA of In_2O_3 favors the direct oxidation of PFOA by the photo-induced holes of In_2O_3 (Li et al. 2012b, Song et al. 2017).

The main decomposition intermediates of PFOA are C_5-C_7 shorter-chain perfluorocarboxylic acids (PFCAs). The time-dependent formation of C_5-C_7 shorter-chain PFCAs in the presence of In_2O_3 NS and rods are shown in Fig. 4.6b and Fig. 4.6c. The amount of PFHpA increased rapidly at the beginning reaching the maximum concentration in 1 h. PFHpA was then gradually decreased and completely degraded in 4 h. PFHxA increased continuously during the first 3 h, and then decreased to zero in 8 h. The concentration of PFPeA increased slowly during 8 h reaction, indicating that PFOA is degraded stepwisely manner to remove the CF_2 units (Li et al. 2012b). In the presence of commercial In_2O_3 (Fig. 4.6d), the concentration of PFHpA increased with irradiation time, and no decrease was observed in 8h.

Fluoride ion was detected during the photocatalytic decomposition process of PFOA (Fig. 4.7). A higher concentration of fluoride ion was detected in the presence of In_2O_3 NS (F^- of 3.89 mg L^{-1}) and In_2O_3 rod (F^- of 3.32 mg L^{-1}), and only 1.79 mg L^{-1} of fluoride ion was detected for commercial In_2O_3.

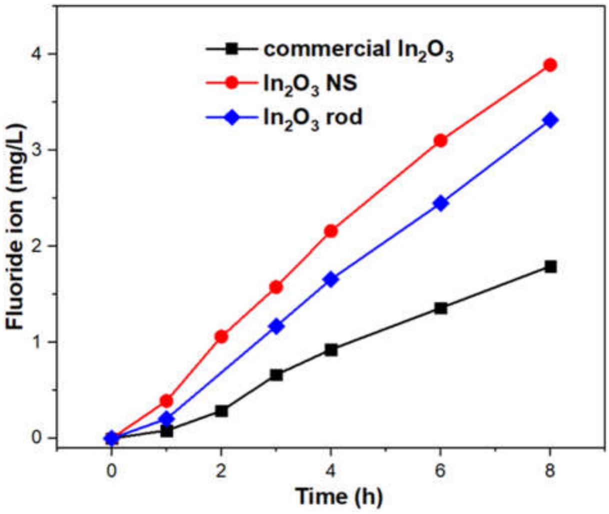

Figure 4.7 Fluoride ion detected during the photodegradation of PFOA.

4.3.3 Charge separation

Transient photocurrent and EIS experiments were carried out to identify the separation efficiency of photoinduced electron-hole pairs (Chen et al. 2016, Liu et al.

2017b). Figure 4.8 shows the transient photocurrent responses under UV light irradiation and EIS of different In_2O_3 electrodes. In_2O_3 NS and commercial In_2O_3 show the similar photocurrent responses peaking at 0.0065 mA, while the photocurrent of In_2O_3 rods is about 0.0055 mA.

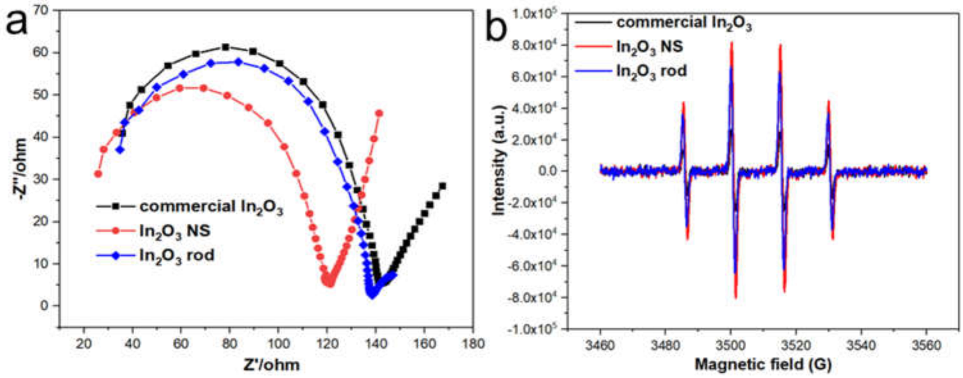

Figure 4.8 Electrochemical impedance spectroscopy (EIS) Nyquist plots of In_2O_3 electrodes (a), and DMPO spin-trapping ESR spectra under UV irradiation for 4 min at room temperature of water in the presence of In_2O_3 samples (b).

Generally, a smaller arc in the EIS Nyquist plot indicates that the charge-transfer resistance on the electrode surface is smaller (He et al. 2014, Teng et al. 2013). The arc radius in the EIS Nyquist plot follows the order of commercial In_2O_3 > In_2O_3 rod > In_2O_3 NS (Fig. 4.8a), indicating that In-BDC derived In_2O_3 has a higher efficiency in charge separation and transfer. This may contribute to the enhanced photocatalytic activity of In_2O_3 NS and rods (WookáLee and WooáHan 2010). The transient photocurrent and EIS results imply that In_2O_3 NS possesses the best efficiency for separation of photogenerated charge carriers, giving rise to its greatest photocatalytic degradation activity of PFOA.

The generation of $OH^{\bullet}$ in the presence of In_2O_3 samples under UV light irradiation was monitored by ESR with DMPO as the spin-trap agent (Fig. 4.8b). The four characteristic peaks of DMPO-$OH^{\bullet}$ adduct with the intensity ratio of 1:2:2:1 were clearly recorded for the In_2O_3 suspension. The signal intensity in the presence of In_2O_3 photocatalysts follow the order of In_2O_3 NS > In_2O_3 rods > commercial In_2O_3. Therefore, In_2O_3 NS and rods generated a higher population of $OH^{\bullet}$ than commercial In_2O_3, thanks to the lower recombination rate of photogenerated holes and electrons, which is consistent with the EIS results.

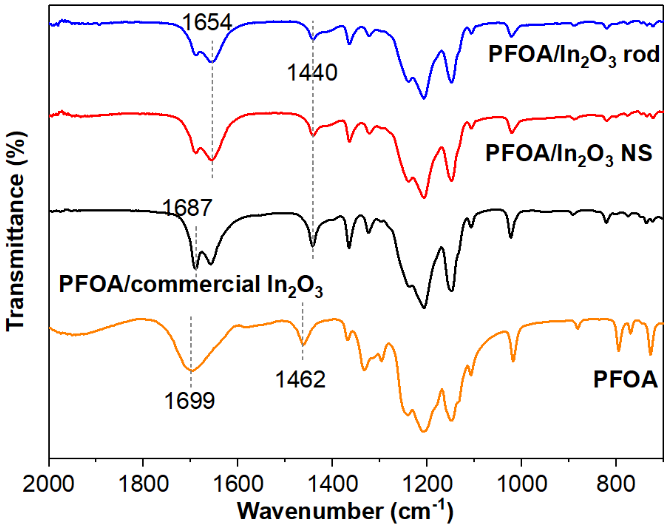

Figure 4.9 DRIFT spectra of PFOA and adsorption equilibrium on In_2O_3 samples.

The peaks at 1699 cm^{-1} and 1462 cm^{-1} of PFOA are ascribed to asymmetric (υ_{as}(COO$^-$)) and symmetric stretches (υ_s(COO$^-$)) of carboxylate, respectively (Fig. 4.9). Upon adsorption on In_2O_3 NS and rods, the asymmetric and symmetric stretching types of the –COO group are located at 1654 and 1440 cm^{-1}, respectively (Nakamoto 2009, Rotzinger et al. 2004a). Similarly, upon adsorption on commercial In_2O_3, υ_{as}(COO$^-$) and υ_s(COO$^-$) appear at 1687 and 1440 cm^{-1}, respectively. An empirical relationship between the frequency difference ($\Delta\upsilon = \upsilon_{as}$(COO$^-$) – υ_s(COO$^-$)) and the bonding modes of carboxylate to cations was concluded (Deacon and Phillips 1980). When the $\Delta\upsilon$ value is larger than the ionic $\Delta\upsilon$, a monodentate coordination type is formed between PFOA and semiconductor photocatalyst, thereagainst a bidentate or bridging coordination (Song et al. 2017, Sun et al. 2019). The $\Delta\upsilon$ of PFOA (237 cm^{-1}) is substantially greater than that of PFOA/In_2O_3 NS or In_2O_3 rod (214 cm^{-1}), and is less than PFOA/commercial In_2O_3 (247 cm^{-1}). This indicates that PFOA coordinates with In_2O_3 NS and In_2O_3 rod in a bidentate configuration, which could promote the direct oxidation of PFOA by photo-induced holes (Li et al. 2012b, Xu et al. 2017b).

Overall, hydrophilic In_2O_3 NS and rods with larger SSA are prepared by the calcination of In-BDC MOF. Higher adsorption capacity for PFOA and tight coordination between PFOA and In_2O_3 NS and rods are beneficial for the direct destruction of PFOA by photo-induced holes. The possible degradation pathway may be that PFOA is firstly decarboxylated by the oxidation of h$^+$ to yield C_7F_{13}•, which is unstable and subsequently react with •OH to form $C_7F_{13}OH$. $C_6F_{11}COOH$ is then generated by the hydrolysis of $C_7F_{13}OH$. $C_6F_{11}COOH$ will undergo the same way to remove CF_2, and finally menalized to fluoride and CO_2 (Figure 4.10).

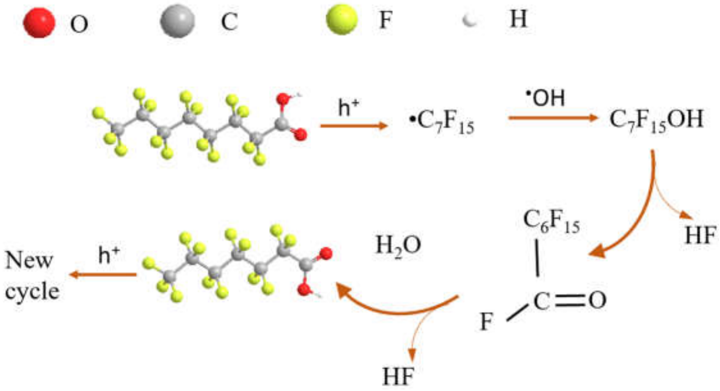

Figure 4.10 The proposed pathway for the photocatalytic degradation of PFOA over In_2O_3.

4.4 Conclusion

In_2O_3 NS and In_2O_3 rod were prepared by the calcination of Indium-based MOFs, and showed much better performances than the commercial In_2O_3 for photocataltyic decomposition of PFOA. After irradiated with UV light, PFOA and intermediates were totally degraded by In_2O_3 NS or rods in 8 h, while only 35% of PFOA was removed by the commercial In_2O_3. The higher photocatalytic activity of In-BDC-based In_2O_3 compared with commercial In_2O_3 is due to the better hydrophlicity which enables a better dispersion in the PFOA solution. The uniform dispersion of the photocatalysts is much beneficial to the photocatalytic evolution of reactive oxygen species ($OH^•$) for the decomposition of PFOA. Moreover, the enhanced hydrophilicity and enlarged SSA facilitate the tight coordination of In_2O_3 NS and In_2O_3 rods with PFOA, which contributed to the rapid photocatalytic degradation of PFOA.

CHAPTER 5

Fe^{3+} promoted the photocatalytic defluorination of PFOA over In_2O_3

5.1 Introduction

Perfluorinated compounds (PFCs) are a group of widely used organofluorine chemicals with fluorine replacing all the hydrogen atoms on the carbon chain (Wang et al. 2017b). Previous studies indicate that PFCs pose considerable concerns to the natural environment and human health due to their wide distribution, extraordinary persistence, bioaccumulation properties, and potential toxicities (Chen et al. 2019, Huang and Jaffé 2019). Perfluorooctanoic acid (PFOA) is the most common PFC presented in environment (Post et al. 2009), and it is detected in different environmental and biological matrices (Heydebreck et al. 2016, Li et al. 2017b). What's worse, the concentration of PFOA was reported up to ng L^{-1} level in some natural waters (Sun et al. 2011), and high concentration level of mg L^{-1} was recorded in groundwater (Houtz et al. 2013). Currently, PFCs are regarded as the most intractable organic pollutants because of the strong C–F bonds, which are endurable to most conventional chemical and biotic approaches (Liu et al. 2020).

Encouragingly, heterogeneous photocatalytic processes appear to be efficient and feasible for the removal of PFOA from wastewater, which could be conducted under mild conditions (Xu et al. 2017a). TiO_2, In_2O_3, Ga_2O_3, Fe-zeolites and bismuth based semiconductors were reported for the study of photocatalytic degradation of PFOA (Liu et al. 2020, Qian et al. 2021). Among them, In_2O_3 photocatalysts hve advantages of facile preparation, chemical stability, and easy availability (Sun et al. 2020c). It also possessed good performance for the photocatalytic degradation of PFOA due to the bidentate coordination with PFOA (Li et al. 2012b). The decomposition of PFOA was initiated by direct hole oxidation (Liu et al. 2021c), the tight coordination of PFOA is essential for direct hole oxidation (Hoffmann et al. 1995). Diffuse reflectance infrared Fourier transform spectroscopy (DRIFTS) is a useful technique to gain an insight into the coordination mode between PFOA and semiconductor photocatalysts (Song et al. 2017, Sun et al. 2019). In-situ DRIFTS were widely used to track the reaction intermediates and products to better understand reaction mechanisms (Li et al. 2020c, Shang et al. 2019).

Previous studies demonstrate that calcination temperature could significantly affect the photoelectrochemical performance of In_2O_3 films by introducing different concentrations of oxygen vacancies (Gan et al. 2013). Furthermore, higher concentration of oxygen vacancies could promote the photocatalytic activity of In_2O_3

catalysts (Huang et al. 2020, Wan et al. 2021, Wang et al. 2020b, Wu et al. 2019c). It is reported that Fe^{3+} could degrade PFOA under ultraviolet (UV) light irradiation, due to the complexation between Fe^{3+} and the carboxyl group of PFOA (Liu et al. 2013). The cations like Fe^{3+} would improve the efficiency of photocatalytic oxidation of TiO_2 hydrosols in solutions by influencing the complex hydroxyl group bond between TiO_2 surface and Fe^{3+} (Wang et al. 2008a). Fe^{3+} was reported to complex with oxalic acid and TiO_2, and greatly accelerated the degradation of oxalic acid in the UV/TiO_2 system (Xie et al. 2018). TiO_2/$FeCl_3$ system was applied to significantly enhance the photocatalytic degradation of sulfonamides under UV irradiation due to the coordination between Fe^{3+} and sulphonamides (Adamek et al. 2015). Previous study also demonstrated the decomposition of PFOA mediated by Fe^{3+} under UV light irradiation (Wang et al. 2008b). Up to date, there are no reports about the effect of Fe^{3+} ion on the photocatalytic performance of In_2O_3 under UV light irradiation. There is no knowledge about whether the oxygen vacancy level in In_2O_3 would affect the interaction between In_2O_3, Fe^{3+} and the pollutant, further influencing the decomposition processes. Therefore, it is quite necessary to carry out studies to know more about the effect of Fe^{3+} on the performances of In_2O_3 catalysts of different oxygen vacancy levels.

In this work, the In_2O_3 samples were prepared by the calcination of $In(OH)_3$ at 300, 400, 500 and 600 ℃ (denoted as In_2O_3-300, In_2O_3-400, In_2O_3-500 and In_2O_3-600), and employed for the photocatalytic destruction of PFOA under 254 nm UV light irradiation. In_2O_3-300/In_2O_3-400 possessed better performance for the decomposition and defluorination of PFOA, due to their larger specific surface area (SSA) and rich oxygen vacancy. The performance of In_2O_3 for the defluorination of PFOA deteriorated while further increasing the calcination temperature. In_2O_3-400 and In_2O_3-600 were selected to investigate the effect of Fe^{3+} on the PFOA degradation over In_2O_3 catalysts. Surprisingly, we found that Fe^{3+} could greatly promote the defluorination of PFOA over the oxygen-vacancy-deficient In_2O_3-600, while a slight increase was obtained in the In_2O_3-400 system. DRIFTS spectra showed that the C=O exited when PFOA was adsorbed on In_2O_3-500/In_2O_3-600, while not detected when PFOA was adsorbed on In_2O_3-300/In_2O_3-400. Therefore, we proposed that Fe^{3+} ions maybe participated in the coordination between PFOA and In_2O_3-600, thus promoting the defluorination of PFOA.

5.2 Experimental section

5.2.1 Preparation of In_2O_3 samples

The In_2O_3 samples were prepared by annealing $In(OH)_3$ in a muffle furnace at 300, 400, 500 and 600 ℃, denoted as In_2O_3-300, In_2O_3-400, In_2O_3-500 and In_2O_3-600, respectively. Thermogravimetric (TG) analysis of the $In(OH)_3$ shows that the dehydration of $In(OH)_3$ to form In_2O_3 occurs at 200 to 270 ℃. From 270 to 600 ℃, high crystalline In_2O_3 phase is formed with little weight loss (Li et al. 2014), thus, 300, 400, 500 and 600 °C were selected.

5.2.2 Characterization of In_2O_3 samples

Scanning electron microscopy (SEM, Zeiss Supra 55VP, Carl Zeiss AG) was employed to observe the morphologies of In_2O_3 catalysts. X-ray diffraction (XRD) (Siemens D5000) was conducted over Bragg angles ranging from 1° to 90° (Cu Kα, $\lambda = 1.54059$ Å). The composition and state of surface elements were monitored by X-ray photoelectron spectroscopy (XPS, ESCALab 250Xi, Thermo Fisher). N_2 adsorption/desorption isotherms were carried out to determine the specific surface areas (SSAs). Transmission electron microscopy (TEM), high-resolution transmission electron microscopy (HRTEM) and the selected area electron diffraction (SAED) were recorded on a JEOL-2100F high resolution transmission microscope using an accelerating voltage of 200 kV. Photoluminescence (PL) spectra were recorded on a fluorescence spectrophotometer (F-4600, Hitachi) to detect the generation of hydroxyl radicals (•OH) on the surface of UV-irradiated In_2O_3 surface without or in the presence of Fe^{3+}. Electron Paramagnetic Resonance (EPR) was carried out using a EPR spectrometer (JES-FA 200). DRIFTS spectra were collected on a Shimadzu Tracer-100 FTIR spectrometer equipped with a high-sensitivity mercury cadmium telluride (MCT) detector cooled by liquid nitrogen.

In-situ DRIFTS were recorded to track the degradation process of PFOA over In_2O_3 catalysts under 254 nm UV light irradiation. In_2O_3 was mixed with PFOA solution (2 g L^{-1}) and stirred for 1 h to ensure that PFOA was adsorbed on In_2O_3. Afterwards, In_2O_3 was separated by centrifugation and heated in the drying oven for 12 h at 55 ℃. In_2O_3 catalysts with adsorbed PFOA were placed in a ceramic cup (0.35 mm depth, 5 mm i.d.) (Wang et al. 2018). The temperature of DRIFTS chamber was controlled at 25 °C. The flow rate of humid air was set as 200 mL min^{-1} controlled by mass flow controllers (Beijing Sevenstar electronics Co., LTD). A background spectrum was recorded firstly. Then, high-pure humid air was introduced. And a 32 W 254 nm UV light lamp was switched on to irradiate the sample. The spectra of DRIFTS were collected every 2 min, with a resolution of 4 cm^{-1}. Each spectrum was the average of 100 scans.

5.2.3 Photocatalytic degradation of PFOA

A cylindrical reactor vessel with a quartz cap was used for the photocatalytic decomposition of PFOA. The volume of the photoreactor was 160 mL, with the height of 8 cm, and the irradiated area was 20 cm^{-2}. The irradiation power received on the surface of the photoreactor was 4.0 mW cm^{-2}. The pH of PFOA solution (10 mg L^{-1}) was 4.85, and after the addition of $FeCl_3$, the solution pH decreased to 4.42, 4.18 and 3.96 when the concentration of $FeCl_3$ was 25, 50 and 100 μM, respectively. 100 mL of PFOA solution (10 mg L^{-1}) and a certain amount of In_2O_3 were mixed in the reactor, the mixture was then stirred in dark for 30 min to achieve adsorption-desorption equilibrium, according to our preliminary experiments. Afterwards, the 254 nm UV light was turned on and 2 mL solution was taken at certain times. Lastly, the sample was filtered for further analysis of PFOA concentration and fluoride ion concentration. The samples were taken at regular times, filtered and then diluted by 20 times. External standards were applied for the quantification of PFOA and its degradation intermediates (Fig. S1). The concentration limit of PFOA and its degradation intermediates were in the range of 0.5-500 μg L^{-1}. The concentration of the fluoride ion was detected by a Dionex ICS-600 IC system.

5.2.4 Analysis of PFOA and its decomposition intermediates

High-performance liquid chromatography-tandem mass spectrometry (HPLC-MS/MS, Agilent) was applied for the quantification of PFOA and its decomposition intermediates. Agilent 1260 series equipped with a Poroshell 120 EC-C18 reversed-phase column (3 ×100 mm, 2.7 μm, Agilent) were employed to separate PFOA and its decomposition intermediates. Mass spectrometric analysis was performed under the multiple reaction monitoring (MRM) mode with negative electrospray ionization. Solvent A (methanol) and solvent B (0.1 % formic acid aqueous solution) were used as the mobile phase. The elution gradient was set as follows: 0-8.0 min, solvent A increased from 30% to 90%; 8.0-10.0 min, held solvent A at 90%; 10.0-13.0 min, solvent A increased from 90% to 100%; 13.0-15.0 min, held this proportion; 15.0-15.5 min, the gradient of solvent A decreased from 100% to 30%.

5.3 Results and discussion

5.3.1 Characterization of In_2O_3 catalysts

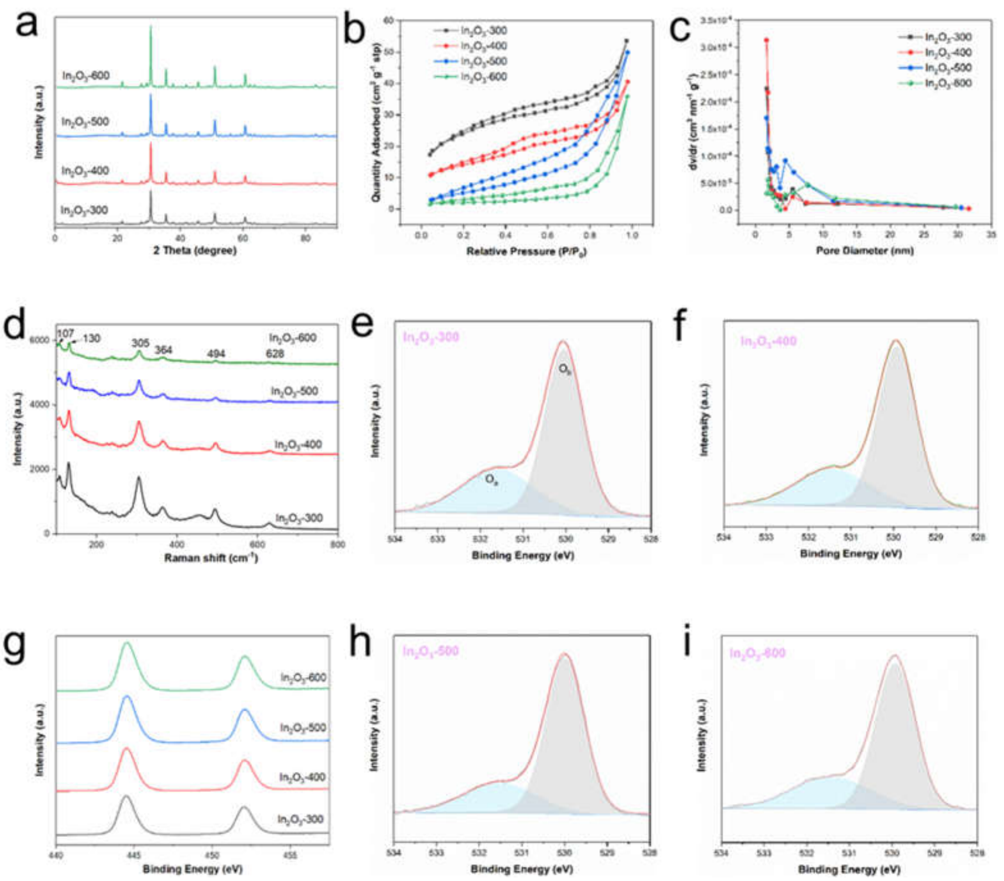

Figure 5.1 XRD patterns (a), N_2 adsorption/desorption isotherm (b), Barrett-Joyner-Halenda (BJH) pore size distribution plots (c) and Raman spectra (d), In 3d core level spectra (g), and the O1s XPS spectra (e, f, h, i) of In_2O_3 samples.

Figure 5.1a shows the powder XRD patterns of In_2O_3 samples. All the recorded peaks can be indexed to the cubic In_2O_3 (JCPDS, No. 06-0416). In addition, the intensity of XRD pattern increases with the increase of calcination temperature, indicating the crystallinity of In_2O_3 enhances with temperature (Yan et al. 2010). The N_2 adsorption/desorption isotherms and the pore-size distribution of In_2O_3 samples are shown in Fig. 5.1b and Fig. 5.1c, respectively. The Brunauer-Emmett-Teller (BET) surface area of In_2O_3-300, In_2O_3-400, In_2O_3-500 and In_2O_3-600 are 83.34, 48.14, 21.96 and 6.80 m^2 g^{-1}, correspondingly. The improved SSA may facilitate the adsorption of PFOA. The defect states of In_2O_3 catalysts treated at different temperatures were analyzed using room temperature Raman-scattering, and the Raman shift data were collected from 100-800 cm^{-1}, as shown in Fig. 5.1d. All observed peaks in Raman spectra of In_2O_3 samples decreased with the increase of the calcination temperature. The results were consistent with the reported values in the literature (Gan et al. 2013). Typically, the peaks at 364 cm^{-1} are attributed to the stretching of In-O-In, which reflects the oxygen vacancy in the In_2O_3 structure (Sun et al. 2020a, Wu et al. 2021). In_2O_3 prepared under lower temperature exhibit higher oxygen vacancy concentration.

XPS spectra were utilized to investigate the sample surface chemistry. The peaks at 444.5 and 452.0 eV could be assigned to the characteristic spin-orbit split $3d_{5/2}$ and $3d_{3/2}$ of In element (Figure 5.1g) (Lei et al. 2014). As shown in Figures 5.1e, 5.1f, 5.1h, 5.1i, the O 1s core spectra were deconvoluted into two peaks located at 530.0 and 531.5 eV, which were named as O_b and O_a, respectively. The O_a peak is related to oxygen atoms adjacent to oxygen deficiency sites and the O_b peak demonstrates O^{2-} ions surrounded by In atoms (Fan and Goodenough 1977). The binding energy (BE) of O_a is about 1.5 eV higher than that of O_b. Therefore, the oxygen vacancy level of In_2O_3 samples corresponds with O_a/O_b ratio (Li et al. 2013c). The O_a/O_b ratios of In_2O_3 materials prepared at 300, 400, 500 and 600 ℃ are calculated to be 0.466, 0.404, 0.342 and 0.329 correspondingly, indicating that oxygen vacancy level of In_2O_3 decreased with the increase of annealing temperature(Lei et al. 2014), consistent with the Raman spectra.

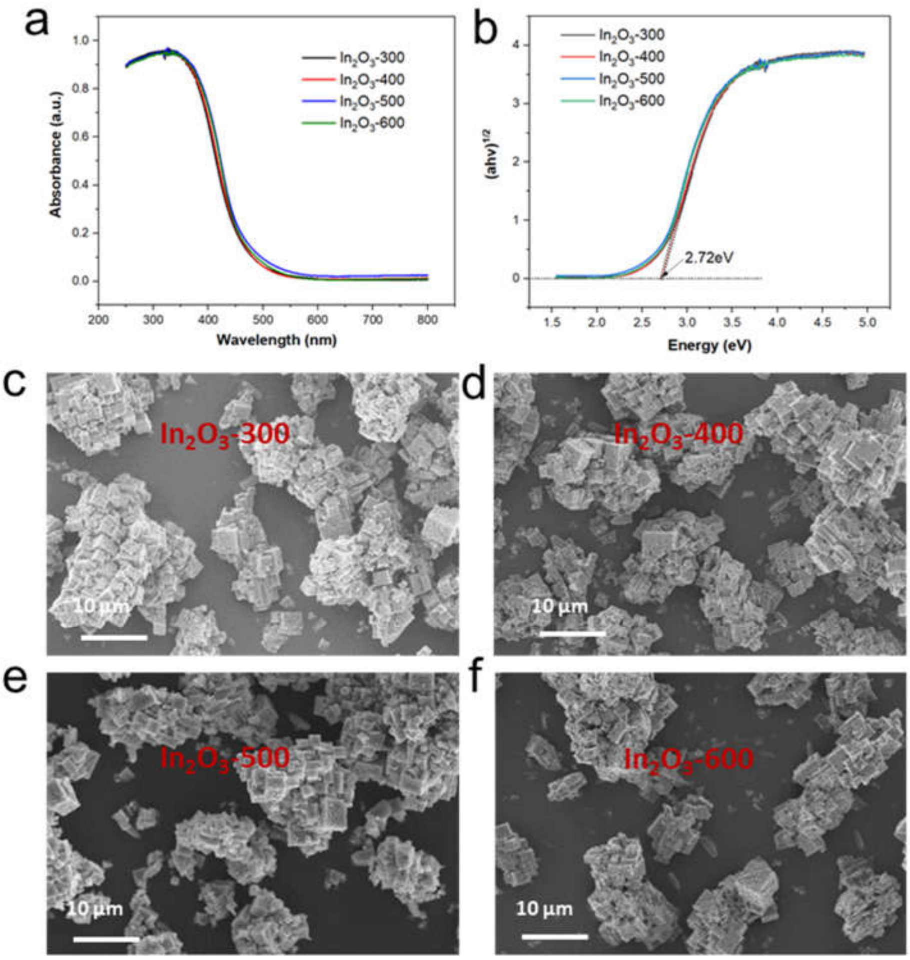

Figure 5.2 UV-vis absorption spectra (a); the band gaps (b) and SEM images (c-f) of In_2O_3 samples.

The UV-vis spectra (Fig. 5.2a) demonstrate that In_2O_3 samples prepared at different temperatures have similar absorption for UV-visible light. From Fig. 5.2b, we can see that the estimated band gap of the In_2O_3 catalysts was ~2.72 eV. In Fig. S3b, $E = hv$, E is the photon energy, h is known as the Planck constant, and v is the light frequency. The conduction band (~2.17 eV) of In_2O_3 was well-positioned for the oxidation of PFOA by photo-induced holes. Figure 5.2c-f shows that In_2O_3 samples obtained at different temperatures have similar morphologies and structures, and thus the influence of morphologies on the performance of In_2O_3 can be excluded. As can be seen from the SEM images (Fig. 5.2), In_2O_3 catalysts obtained by the calcination of $In(OH)_3$ at 300, 400, 500 and 600 °C had similar particle sizes. The particle sizes of the In_2O_3 particles were in the range of 2-5 µm. The microstructures of In_2O_3-400 and In_2O_3-600 were explored by TEM analyses, as shown in Fig. 5.2. The SAED pattern indicate that In_2O_3-400 (Fig. 5.3b) and In_2O_3-600 (Fig. 5.3g) exhibit the polycrystalline nature. The interplanar spacing of 0.292/0.289 and 0.413 nm indicated the presences of (222) and (211) planes of In_2O_3 (Fig. 5.3c and Fig. 5.3f). The observed stripes demonstrate good crystallinity of In_2O_3-600 (Fig. 5.3h), while the lattice fringes of In_2O_3-400 (Fig. S6a) were not that obvious as In_2O_3-600, indicating its much lower crystallinity. The results were consistent with the XRD intensities of In_2O_3 catalysts. Thus, more amorphous phases were mingled with crystal phases at lower calcination temperatures (300 and 400 °C), resulting in the formation of defect structures (Wang et al. 2021b). A great amount of dangling bonds in the defects would act as dense active sites for enhancing the activities of catalysts (Chandrasekaran et al. 2019, Hao et al. 2020).

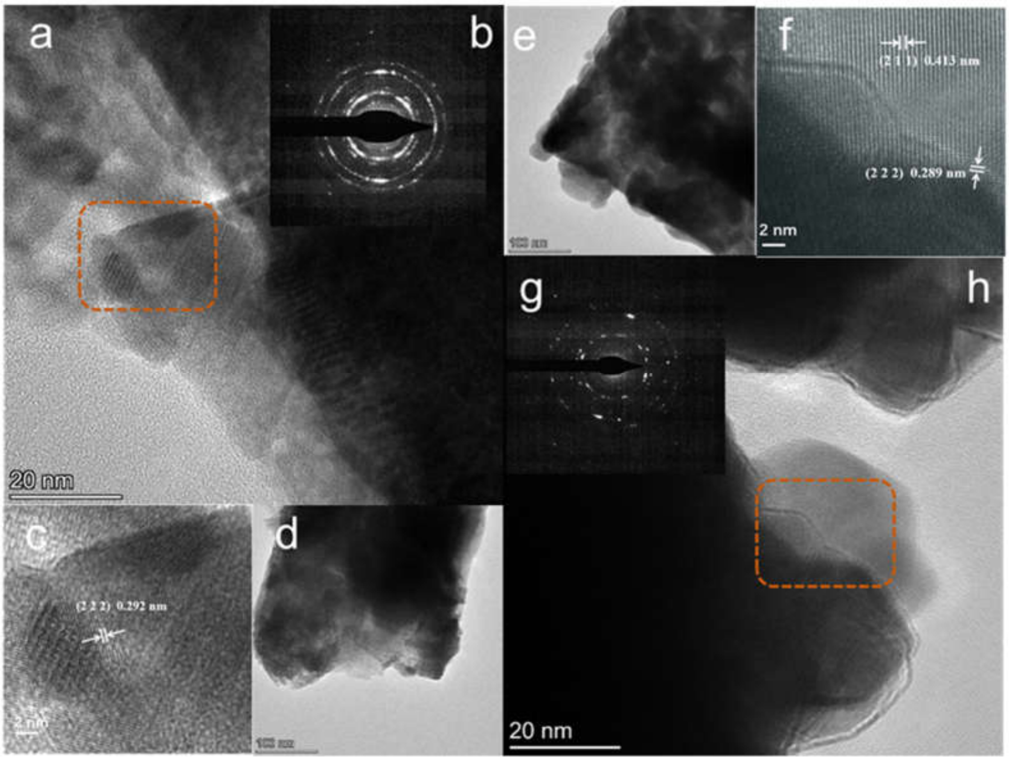

Figure 5.3 HRTEM images of In_2O_3-400 (a); The SAED pattern of In_2O_3-400 (b); magnified image of the circled area in Fig. 5.3a (c); TEM image of In_2O_3-400 (d); TEM image of In_2O_3-600 (e), magnified image of the circled area in Fig. 5.3h (f), the SAED pattern of In_2O_3-600 (g), HRTEM image of In_2O_3-600 (h).

5.3.2 Photocatalytic decomposition of PFOA by In_2O_3 catalysts

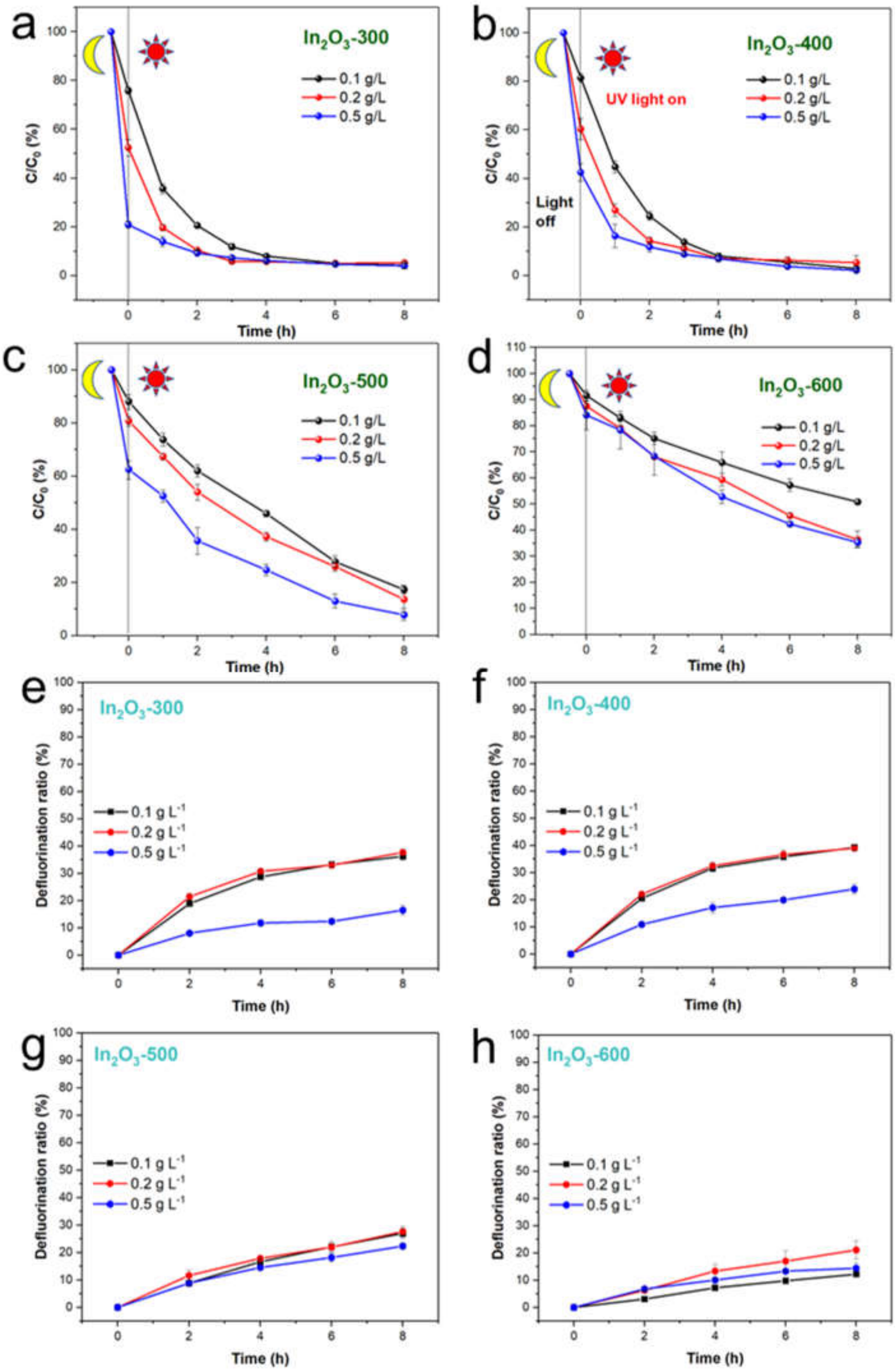

Figure 5.4 Time course of PFOA degradation and the defluorination ratio of PFOA in the presence of (a, e) In_2O_3-300, (b, f) In_2O_3-400, (c, g) In_2O_3-500 and (d, h) In_2O_3-600 of different dosages.

Figure 5.4a-d show the removal of PFOA from aqueous solution in the presence of In_2O_3 catalysts of different concentrations. Less PFOA was adsorbed onto In_2O_3 prepared at higher temperatures, during the dark adsorption period. The SSA of In_2O_3 decreased with the increase of calcination temperature. Less adsorption sites were provided due to lower SSA of In_2O_3-600, therefore less PFOA was adsorbed. About 80% of PFOA was adsorbed by In_2O_3-300 with the dosage of 0.5 g L^{-1}, while only less than 20% of PFOA was adsorbed by In_2O_3-600 under the same condition. Moreover, PFOA could be almost completely removed in 4 h in the presence of In_2O_3-300 or In_2O_3-400. For In_2O_3-500, about 80-90% of PFOA could be removed in 8h, and only 40-60% of PFOA could be removed in 8h with In_2O_3-600. Defluorination ratio is also one of the important indexes for the mineralization of PFOA. As shown in Figure 5.4e-h, In_2O_3-400/In_2O_3-300 show the best defluorination performance of PFOA (38% for In_2O_3-400 and 35% for In_2O_3-300). In_2O_3-600 demonstrated a poor performance with a defluorination ratio ~20%. To obtain a higher defluorination ratio of PFOA decomposition, 0.2 g L^{-1} is the optimal concentration for these four kinds of In_2O_3 catalysts (Fig. 5.4e-h). In_2O_3-400 and In_2O_3-600 were selected to investigate the effect of Fe^{3+} on the decomposition of PFOA, and $FeCl_3$ was used to provide Fe^{3+}.

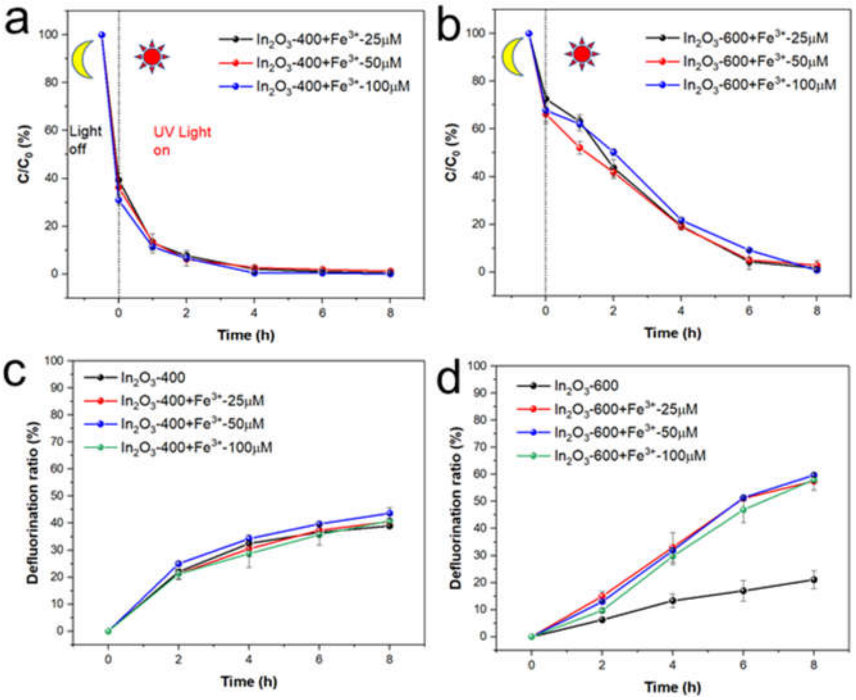

Figure 5.5 The effect of Fe^{3+} on the degradation of PFOA over (a) In_2O_3-400 and (b) In_2O_3-600. The defluorination ratio of PFOA in (c) Fe^{3+}/In_2O_3-400 and (d) Fe^{3+}/In_2O_3-600 systems.

5.3.3 Fe^{3+} Promoted the photocatalytic defluorination of PFOA over In_2O_3

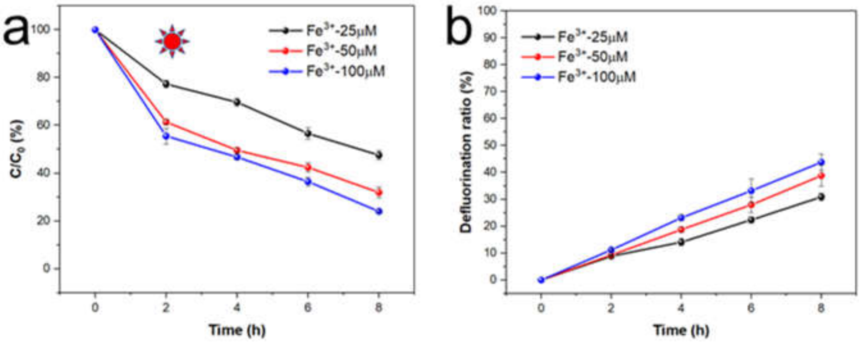

Figure 5.6 Time course of PFOA degradation (a) and the defluorination ratio of PFOA in Fe^{3+}/UV systems (b).

When Fe^{3+} was added in the aqueous solution, the adsorption of PFOA was enhanced (Fig. 5.5a-d). In the presence of Fe^{3+}, ~60% and 30% of PFOA was adsorbed by In_2O_3-400 and In_2O_3-600, respectively. PFOA was completely deprotonated when the solution pH ≥ 4 (Liu et al. 2020). With the decrease of solution pH, In_2O_3 surface became more positively charged, which facilitated the adsorption of anionic PFOA (Sahu et al. 2018). The addition of $FeCl_3$ decreased the solution pH, therefore enhancing the adsorption of PFOA (Fig. 5.5a-b). The concentration of Fe^{3+} (25, 50 and 100 μM) had little effect on the adsorption and decomposition of PFOA in Fe^{3+}/In_2O_3-600 system. While Fe^{3+} only slightly increased the defluorination efficiency of PFOA over In_2O_3-400 (Fig. 5.5c), with the defluorination ratio increased from 39% to 43%. Fe^{3+} markedly enhanced the photocatalytic degradation of PFOA over In_2O_3-600, with PFOA completely removed after UV irradiation for 8h. Moreover, a defluorination ratio of 60% was achieved in the Fe^{3+}/In_2O_3-600 system, three times higher than In_2O_3-600 (Fig. 5.5d). Fe^{3+} was used as the catalyst for the decomposition of PFOA under UV irradiation (Fig. 5.6a), the defluorination ratio increased from 30% to 43% with the concentration of Fe^{3+} increased from 25 to 100 μM (Fig. 5.6b), and the degradation ratio of PFOA increased from 53% to 76% (Fig. 5.6a).

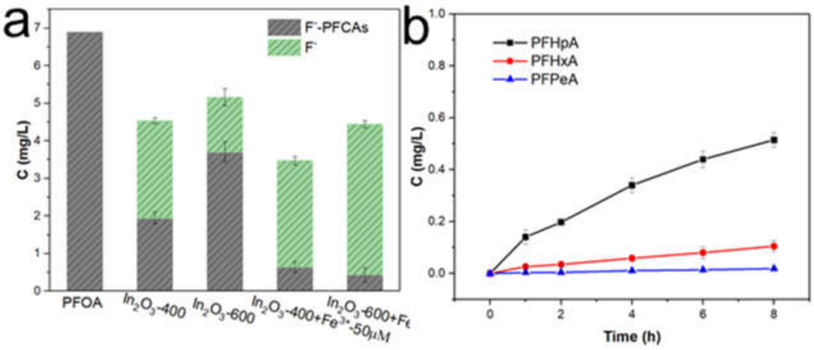

Figure 5.7 The mass balance of fluorine after UV irradiation for 8h (a); Time course of shorter-chain intermediates formation in the UV/Fe^{3+} (25 µM) system (b).

After irradiation with UV light for 8h, the fluorine mass balance was calculated (Fig. 5.7a). The F content in the decomposition intermediates of PFOA decreased with the assistance of Fe^{3+}, while the F content detected was less than 100 %, the reason could be that some of PFOA and its PFACs were adsorbed on the surface of In_2O_3. Figure 5.8 displayed the time-dependent concentrations of the decomposition intermediates of PFOA, i.e., perfluoroheptanoic acid ($C_6F_{13}COOH$, PFHpA), perfluorohexanoic acid ($C_5F_{11}COOH$, PFHxA) and perfluoropentanoic acid (C_4F_9COOH, PFPeA) during the UV light irradiation process. Shorter-chain perfluorocarboxylic acids (PFCAs), mainly C5-C7 PFCAs were detected in the decomposition processes. In In_2O_3-400 and In_2O_3-400/Fe^{3+} systems, PFHpA ($C_6F_{13}COOH$) increased firstly, reaching the maximum concentration in 2h, and started to decrease afterwards (Fig. 5.8a and Fig. 5.8c). PFHpA can be further decarboxylated and degraded into perfluorohexanoic acid (PFHxA, $C_5F_{11}COOH$), and finally mineralized to fluoride ion and carbon dioxide. While, in In_2O_3-600 system (Fig. 5.8b) and Fe^{3+}-25µM/UV system (Fig. 5.7b), the concentration of PFHpA kept increasing in 8h. When Fe^{3+} was added in the In_2O_3-600 system, the amount of PFHpA increased in the first 4h and then decreased (Fig. 5.7d), demonstrating the faster generation and elimination of PFHpA than in In_2O_3-600 Fe^{3+}/UV systems. These results indicated that Fe^{3+} greatly promoted the decomposition of PFOA over In_2O_3-600. The stepwise degradation of PFOA and shorter-chain PFCAs in In_2O_3 and In_2O_3/Fe^{3+} systems implied that Fe^{3+} did not affect the decomposition pathway, where one CF_2 was removed in one step.

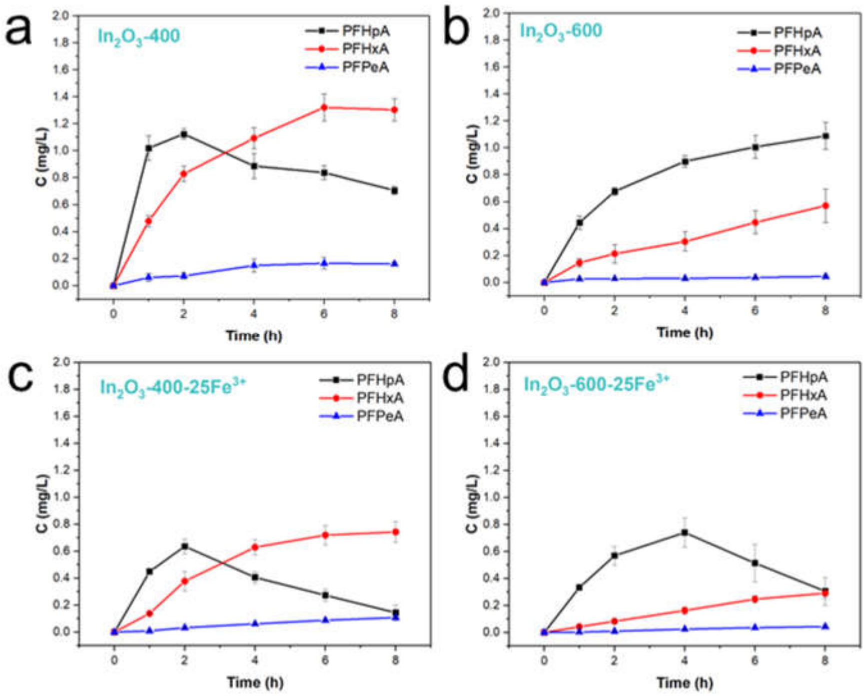

Figure 5.8 Time course of shorter-chain intermediates formation under UV irradiation over (a) In_2O_3-400, (b) In_2O_3-600, (c) In_2O_3-400 and (d) In_2O_3-600 in the presence of Fe^{3+}.

5.3.4 Mechanism of photocatalytic PFOA decomposition over In_2O_3 in the presence of or without Fe^{3+}

DRIFTS analysis was carried out to characterize the structural changes of adsorbed PFOA on In_2O_3 catalysts, as shown in Fig. 5.9a. PFOA adsorbed on In_2O_3 in the form of its carboxylate anions (Ekström and McQuillan 1999). The typical asymmetric and symmetric vibration of O=C-O- appeared in the DRIFTS spectra. The peak at 1662 cm^{-1} could be assigned to the asymmetric stretching (Δv_{as}) of O=C-O-, and the peak at 1440 cm^{-1} was due to the symmetric vibration (Δv_s) of O=C-O- group (Rotzinger et al. 2004b, Wang et al. 2019b). The lower Δv ($\Delta v_{as} - \Delta v_s$=222 cm^{-1}) of PFOA carboxylate indicated the bidentate coordination between PFOA and In_2O_3-300/In_2O_3-400(Song et al. 2019). While, when PFOA was adsorbed onto In_2O_3-500/In_2O_3-600, a shoulder peak appeared at 1692 cm^{-1}, which maybe due to the uncoordinated C=O group of PFOA. The asymmetric peak of O=C-O- at 1649 cm^{-1} and the shoulder peak appeared at 1692 cm^{-1} suggested that both bidentate and monodentate carboxylate coordination modes existed between PFOA and In_2O_3-

500/In_2O_3-600 (Fig. 5.9b-1, Fig. 5.9b-2) (Gao and Chorover 2012, Gu et al. 2016a). We suggested that the dangling C=O group of PFOA in the In_2O_3-600 system could coordinate with the added Fe^{3+}. A tight coordination between Fe^{3+}, PFOA and In_2O_3-600 was formed (Fig. 5.9b-3), facilitating the direct oxidation of PFOA by photo-generated holes in In_2O_3. Thus, the addition of Fe^{3+} could significantly enhance the defluorination of PFOA over In_2O_3-600.

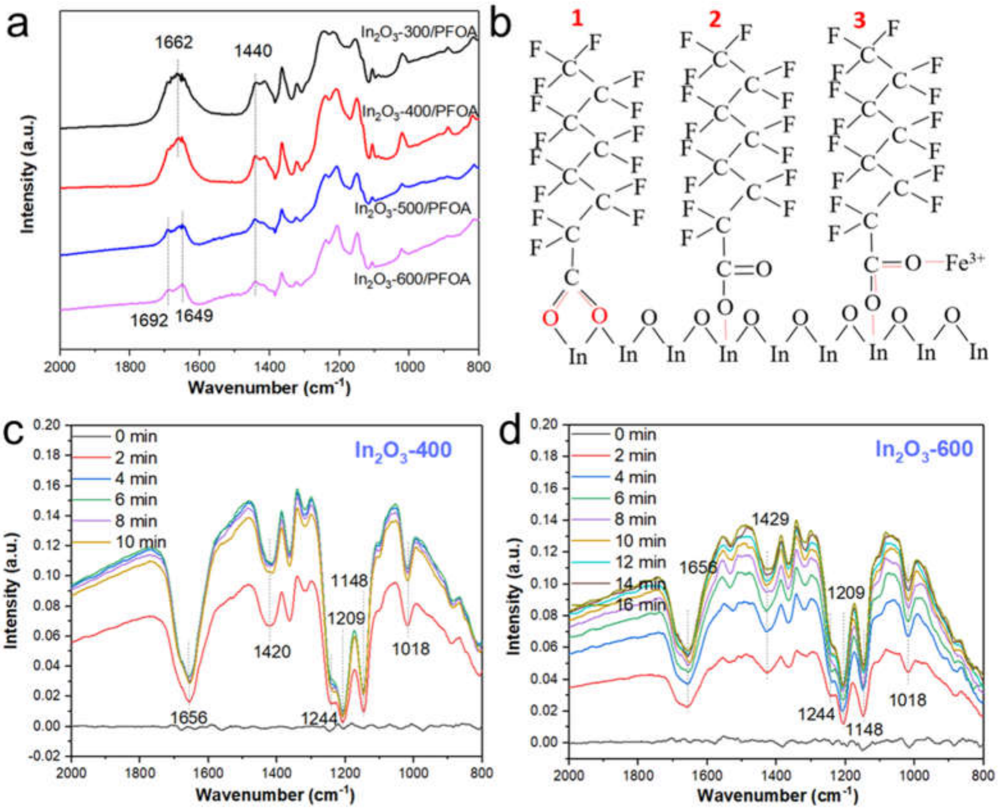

Figure 5.9 DRIFT spectra of PFOA adsorption equilibrium on In_2O_3 catalysts (a); The coordination modes of PFOA with In_2O_3 and the coordination mode of PFOA with In_2O_3 in the presence of Fe^{3+} (b); The in-situ DRIFTS spectra for the photocatalytic degradation processes of PFOA over (c) In_2O_3-400, (d) In_2O_3-600.

To further understand the degradation process of PFOA over In_2O_3, the in-situ DRIFTS was recorded. The processes over In_2O_3-400 and In_2O_3-600 were carried out to know if there were any differences of the decomposition processes due to their different coordination modes with PFOA. Figures 5.9c and 5.9d show the structural changes of PFOA during decomposition processes over In_2O_3-400 and In_2O_3-600, respectively. Peaks at 1656 cm^{-1} and 1420/1429 cm^{-1} could be attributed to the asymmetric and symmetric vibrations of carboxyl groups (Song et al. 2017), and peaks at 1148 cm^{-1}, 1209 cm^{-1} and 1286 cm^{-1} are assigned to C–F bonds. Peak at 1018 cm^{-1} corresponds to stretching of C–C bond. The reversed peaks demonstrate the consumption of –COOH group, C–F and C–C bonds, further verifying that the –COOH and C–F were attacked during the degradation process. PFOA was degraded on the surface of In_2O_3-400 more quickly than over In_2O_3-600, due to the higher concentration of oxygen vacancy (Gan et al. 2013, Li et al. 2013c). It only takes 4 min to reach the maximum peak intensity on the surface of In_2O_3-400 (Fig. 5.9b), while more than 10 min is required for In_2O_3-600 (Fig. 5.9c). In addition, the shoulder peak at 1690 cm^{-1} (Fig. 5.9a) was due to the vibration of C=O bond, demonstrating that the monodentate coordination mode influenced the decomposition process. Thus, the decarboxylation of PFOA over In_2O_3-600 became slower, and a lower defluorination ratio and decomposition rate was obtained. Which could also be observed in the in-situ spectra of PFOA decomposition. So, we supposed that Fe^{3+} could assist the coordination of PFOA with oxygen-vacancy-deficent In_2O_3 in the mode as shown in Fig. 5.9b-3. Moreover, similar intensities of PL spectra emission at 420 nm were observed (Fig. S11), demonstrating the similar generation rate of •OH radicals. These results indicated that calcination temperature (400 and 600 °C) and Fe^{3+} had little influence to produce •OH radicals. Therefore, the enhancement promoted by Fe^{3+} was not due to the higher production of •OH species. The decarboxylation was initiated by the hole oxidation. The tight coordination facilitated the decarboxylation. Ferric ion easily forms complex with carboxylate and the complex formed may photolyze to Fe^{2+} and an organic radical through the ligand-to-metal charge transfer. Both the Fe^{3+} ion and photo-induced holes on the surface of In_2O_3 could synergistically accelerate the decarboxylation of PFOA.

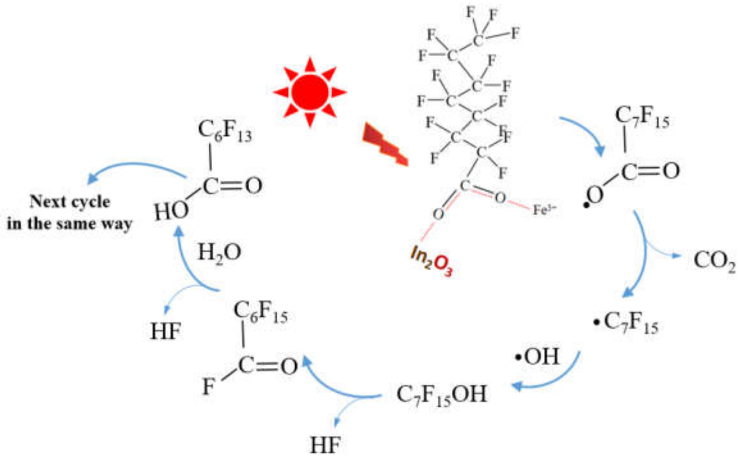

Figure 5.10 The proposed pathway of PFOA over oxygen-vacancy-deficient In_2O_3 in the presence of Fe^{3+}.

The coordination modes of –COOH with In_2O_3 is critical for the decarboxylation of PFOA (Li et al. 2020b), which is the initial step for PFOA decomposition (Qu et al. 2016). In the In_2O_3-600/Fe^{3+} system, Fe^{3+} participated in the complexation between In_2O_3-600 and PFOA (Figure 5.10), pacifying the dangling C=O group of PFOA (Liu et al. 2017a). Under UV light irradiation, C_7F_{15}• was generated from the decarboxylation of PFOA, and subsequently reacted with •OH radical to generate $C_7F_{15}OH$ (Song et al. 2017, Yang et al. 2020b). $C_7F_{15}OH$ would dissociate to HF and $C_6F_{13}COF$, which would then hydrolyze to generate $C_6F_{13}COOH$ and HF. $C_6F_{13}COOH$ then degraded the same way as PFOA, and finally to F^- and CO_2 (Liu et al. 2020, Trojanowicz et al. 2018).

5.4 Conclusion

In summary, In_2O_3 samples were prepared by the calcination of $In(OH)_3$ at different temperatures (300, 400, 500 and 600 °C) and used for the removal of PFOA from contaminated water under UV light irradiation. The experiment results show that the photocatalytic performance of In_2O_3 decreased with the increase of calcination temperature. Oxygen vacancy rich In_2O_3-300 and In_2O_3-400 possessed good performance for the decomposition and defluorination of PFOA, when further increasing the calcination temperature, the performance of obtained In_2O_3 deteriorate for the decomposition and defluorination of PFOA. However, when Fe^{3+} ion was added in the system, the defluorination ratio of PFOA over In_2O_3-600 significantly increased, from 20% to 60%, while only very slightly increased in the In_2O_3-400 system, from 39% to 43%. DRIFTS spectra demonstrated that uncoordinated C=O group existed when PFOA was adsorbed on In_2O_3-600. Therefore, we supposed that Fe^{3+} participated in the coordination between PFOA and oxygen-vacancy-deficient In_2O_3-600, therefore promoting the decomposition and defluorination of PFOA.

CHAPTER 6

High-performance photocatalytic decomposition of PFOA by BiOX/TiO$_2$ heterojunctions: self-induced inner electric fields and band alignment

6.1 Introduction

Perfluorooctanoic acid (PFOA) is one of the most spilled perfluoroalkyl substances (PFAS) which has been widely used in life and work supplies, such as fire retardants and waterproof textiles (Wang et al. 2017b). PFOA has been globally detected in aquatic and terrestrial environments (Xu et al. 2017a) and found in many organisms (Cui et al. 2020). Exposure to PFOA over certain levels may lead to many human diseases such as kidney cancer (Mulabagal et al. 2018), neurotoxicity and cardiotoxicity (Eriksen et al. 2010, Johansson et al. 2008). Moreover, most conventional remediation technologies demonstrate poor efficiency for PFOA degradation, due to the recalcitrant C-F bond (Trojanowicz et al. 2018). However, there are limited mild, efficient and easy-operational processes to completely break down PFOA. Therefore, efficient technologies are urgently required to ensure the complete mineralisation of the intractable PFOA (Tenorio et al. 2020).

The incomplete decomposition of PFOA results in shorter-chain perfluorocarboxylic acids (PFCAs), which would still pose environmental risks (Ochoa-Herrera et al. 2016). Reverse osmosis (RO) and adsorption can efficiently remove PFOA from the aqueous solution, but the residual needs further treatment by other chemical methods (Wang et al. 2017b). Biological approaches demonstrated low efficiency for the degradation of PFOA (Trojanowicz et al. 2018). Chemical technologies for PFOA degradation mainly include photochemical (Xiong et al. 2020), electrochemical and thermal treatment processes. Complete mineralisation generally requires incineration or high-temperature thermal treatments, which needed to be conducted under harsh conditions (Hao et al. 2021, Wu et al. 2019a). As a result, extensive research efforts are devoted to exploring photocatalysts of excellent efficiency to enable the complete defluorination and mineralisation of PFOA at mild conditions. Normally, PFOA was degraded under UV254 nm or UV185nm irradiation (Li et al. 2012c, Shao et al. 2013a), due to the recalcitrant C-F bond. The extension of spectral region would help to maximise the use of nature sunlight to treat PFOA.

BiOX (X= Cl, Br, and I) photocatalysts are p-type semiconductors (Song et al. 2021). BiOX have been reported to show good performance for photocatalytic degradation of PFOA (Song et al. 2017, Wang et al. 2019a, Yang et al. 2020b). The BiOX consists of tetragonal $[Bi_2O_2]^{2+}$ positive layers interleaved by negative halide layers, and the layers are connected through van der Waals interactions with X atoms along the *c*-axis, leading to 2D flexible ultrathin nanosheets (Ai et al. 2009, Li et al. 2017a, Zhang et al. 2006) (Li et al. 2017a). The internal electric field (IEF) in BiOX photocatalysts endows them with appealing photocatalytic activity because IEF will facilitate charge separation and migration from bulk to surface (Li et al. 2016a, Zhang et al. 2006). Construction of heterojunctions is also an efficient strategy to enhance the photocatalytic performances. The establishment of heterojunction interfaces would facilitate photo-induced charge separation and transfer, thus enhancing photocatalysis of the composites. The studies of BiOX-based heterojunctions mainly focused on p-n heterojunctions, type II and Z-scheme systems (Wang et al. 2019d). For example, $BiOI@Bi_{12}O_{17}Cl_{12}$ (Fan et al. 2016), $BiOBr/Bi_2WO_6$ (Hu et al. 2016), and g-C_3N_4/BiOX (Song et al. 2021) have been developed which demonstrated improved efficiencies than pure BiOX.

TiO_2 is a benchmark and commercial catalyst in photochemistry owing to its easy availability, photostability, and high redox capacity (Kapilashrami et al. 2014, Sun et al. 2020b). However, its photocatalytic activity is restricted by the rapid recombination of photo-induced electron-hole pairs (Choi et al. 1994). Built-in electric field (BIEF) can be created near the interfaces of p-n heterojunctions, which could enhance the separation efficiency of photo-induced electrons and holes, thus improving the photocatalytic activities (Ji et al. 2016). Specifically, p-type and n-type semiconductors are combined to prepare an effective p-n heterojunction (Duoerkun et al. 2020, Low et al. 2017). BIEF will guide the migration of photo-generated electrons to the conduction band (CB) of the n-type semiconductor and photo-generated holes to the valence band (VB) of the p-type semiconductor, respectively. Normally, in a p-n heterojunction photocatalyst, the positions of CB and VB of p-type semiconductor are higher than n-type semiconductors (Chen et al. 2010, Zhang et al. 2010b). Thus, the band alignment would also drive the photo-induced holes and electrons to VB of the p-type semiconductor and CB of the n-type semiconductor, respectively. Consequently, the synergistic effect between BIEF and band alignment would lead to a high charge separation efficiency and activity in photocatalysis.

Herein, BiOX/TiO_2 composites were prepared by a facile hydrothermal approach. The formation of p-n heterojunctions significantly enhanced the performance for photocatalytic decomposition of PFOA. PFOA was completely decomposed by BiOBr/TiO_2 and BiOCl/TiO_2 heterojunctions. A high defluorination ratio of 82% was obtained in the BiOCl/TiO_2/UV system. We applied advanced characterizations to reveal that IEF of BiOX and the band alignment regulated the photo-induced electrons transfer from BiOX to TiO_2, and facilitated the charge carrier shuttle between BiOX and TiO_2, thus improving the activity for generating reactive oxygen species (ROS) and enhancing PFOA decomposition.

6.2 Materials and methods

6.2.1 Preparation of BiOX and BiOX/TiO_2 catalysts

The BiOX (X=Cl, Br, I) and BiOX/TiO_2 photocatalysts were synthesized by hydrothermal approaches. Specifically, $Bi(NO_3)_3•5H_2O$ (1.33 mmol) and KX (1.66 mmol) were dissolved in 33.3 mL ethylene glycol, respectively. 106 mg TiO_2 was dispersed in $Bi(NO_3)_3•5H_2O$ solution by stirring to obtain a homogeneous suspension. Subsequently, the KX solution was added into the above suspension under vigorously stirring. The obtained mixture was kept stirring for another 1 h and then transferred to a 100 mL Teflon-lined autoclave, sealed and heated for 12 h at 120 ℃. Finally, the obtained composites were separated by centrifugation. The separated composites were then washed by ethanol and deionized water for several times. BiOX catalysts were synthesized with the same procedures without adding TiO_2.

6.2.2 Characterizations of BiOX and BiOX/TiO_2 catalysts

The UV-Vis absorption spectra of BiOX and BiOX/TiO_2 photocatalysts were recorded on a 950 UV/Vis-NIR spectrophotometer (Perkin Elmer Lambda). X-ray diffractions (XRD) (Bruker D8 Advance) were collected from 10° to 80°. X-ray photoelectron spectroscopy (XPS, ESCALab 250Xi, Thermo Fisher) was applied to investigate the compositions, quantities, and state of surface elements of the as-synthesized photocatalysts. The specific surface areas (SSAs) and the pore size distributions of the studied photocatalysts were investigated by a surface-area pore analyser. The morphologies of BiOX and BiOX/TiO_2 catalysts were observed by scanning electron microscopy (SEM, Zeiss Sigma 300). The transmission electron microscopy (TEM), high-resolution transmission electron microscopy (HRTEM) and the selected area electron diffraction (SAED) images were collected on a JEOL-2100F high-resolution transmission microscope. A Fourier transform infrared spectrometer (FTIR, Shimadzu Tracer-100) equipped with a high-sensitivity mercury cadmium telluride (MCT) detector was applied to collect the diffuse reflectance infrared Fourier transform spectroscopy (DRIFTS). Electron spin resonance (EPR) was conducted on an ESR spectrometer (JES-FA 200).

6.2.3 Photocatalytic degradation of PFOA

The reactors used and the pH conditions of the PFOA solution were the same as our previous work (Liu et al. 2021b). A certain amount of catalyst was added in the PFOA solution (initial concentration of 10 mg L^{-1}) and then stirred in dark for 30 min to observe the adsorption of PFOA onto the studied semiconductor photocatalysts. High-concentration PFOA have been detected in polluted water from PFAS related factories (Lin et al. 2010), and previous studies reported the concentration of PFOA up to 6.57 mg L^{-1} in surface waters after accidental spills of aqueous firefighting foam in the united States (Schultz et al. 2004). Therefore, we choose 10 mg L^{-1} as the initial PFOA concentration for performance evaluation of the photocatalysts. A 254 nm UV light (30 W) and Xenon lamp (300 W) were applied as the light sources. The Xenon lamp emission light spectrum was shown in Fig. S1 (the blue one). 2 mL liquid was taken at regular time intervals. Lastly, the samples were filtered to detect the concentrations of PFOA, degradation intermediates and fluoride ion. All the photocatalytic PFOA degradation experiments were conducted with triplicates.

6.2.4 Analysis of PFOA and its decomposition intermediates

PFOA and the degradation intermediates were quantified using high-performance liquid chromatography-tandem mass spectrometry (HPLC-MS/MS, Agilent). The organic species were firstly separated by an Agilent 1260 series equipped with a Poroshell 120 EC-C18 reversed-phase column (3 ×100 mm, 2.7 μm). Multiple reaction monitoring (MRM) mode with negative electrospray ionization were applied for the mass spectrometric analysis. Methanol (mobile phase A) and 0.1 % formic acid aqueous solution (mobile phase B) were used as the mobile phases for HPLC analysis. The elution gradients of this analysis method were set as follows: methanol gradient increased from 30% to 90% from 0 to 8.0 min; 8.0-10.0 min, held mobile phase B at 90%; 10.0-13.0 min, linearly increased mobile phase A from 90% to 100%; 13.0-15.0 min, held this proportion; 15.0-15.5 min, decreased the mobile phase A from 100% to 30% linearly.

6.3 Results and discussion

6.3.1 Characterizations of BiOX and BiOX/TiO_2 catalysts

Table 6.1 The SSA and the average pore sizes of BiOX and BiOX/TiO_2 catalysts.

Catalyst	BiOCl	BiOCl/ TiO_2	BiOBr	BiOBr/ TiO_2	BiOI	BiOI/ TiO_2	TiO_2
SSA (m^2 g^{-1})	58.6	45.1	41.2	61.2	67.1	55.8	122.9
Average pore size (nm)	3.3	6.6	4.4	6.6	4.4	5.6	4.1

The crystalline structures and phases of BiOX and BiOX/TiO_2 catalysts were identified by XRD patterns (Fig. 6.1a-c). The fingerprints of crystalline BiOCl, BiOBr and BiOI could be assigned to standard tetragonal phases (JCPDS Card No. of BiOCl: 06-0249; BiOBr: 09-0393 and BiOI: 73-2062). Better exposure of planes would cause increased intensity of the corresponding diffraction peaks (Chen et al. 2013). A typical [101] anatase phase (JCPDS file No. 21-1272) and some rutile phases were identified (JCPDS file No. 21-1276) in the XRD spectra of TiO_2 (P25). The characteristic peak of [110] phase exhibited the strongest intensity in BiOX. However, when combined with TiO_2, the intensity of peak [110] of BiOX became relatively weaker. The changes in XRD patterns suggested that the [110] facet of BiOX nanocrystals is inclined to grow on TiO_2 nanoparticles. A small peak of [101] lattice plane of TiO_2 could be observed in the diffraction patterns of BiOI/TiO_2. Also, a swell aside the [101] peak of BiOCl was found for BiOCl/TiO_2 composite which was attributed to the diffraction of TiO_2. These results indicated the successful preparation of BiOX/TiO_2 heterojunctions. The specific surface area (SSA) and pore size distribution of BiOX and BiOX/TiO_2 catalysts were analysed by N_2 adsorption-desorption process (Table 6.1). The SSA of BiOCl(I)/TiO_2 decreased by ~20%, compared with BiOCl(I). BiOBr/TiO_2 (61.2 m^2 g^{-1}) had larger SSA than BiOBr (41.2 m^2 g^{-1}). After combining with TiO_2, BiOX/TiO_2 possessed a larger average pore size than BiOX. The SSA of BiOX and BiOX/TiO_2 were in the range of 40-70 m^2 g^{-1}. It is not the significant impact factor on the photocatalytic efficiency in this study.

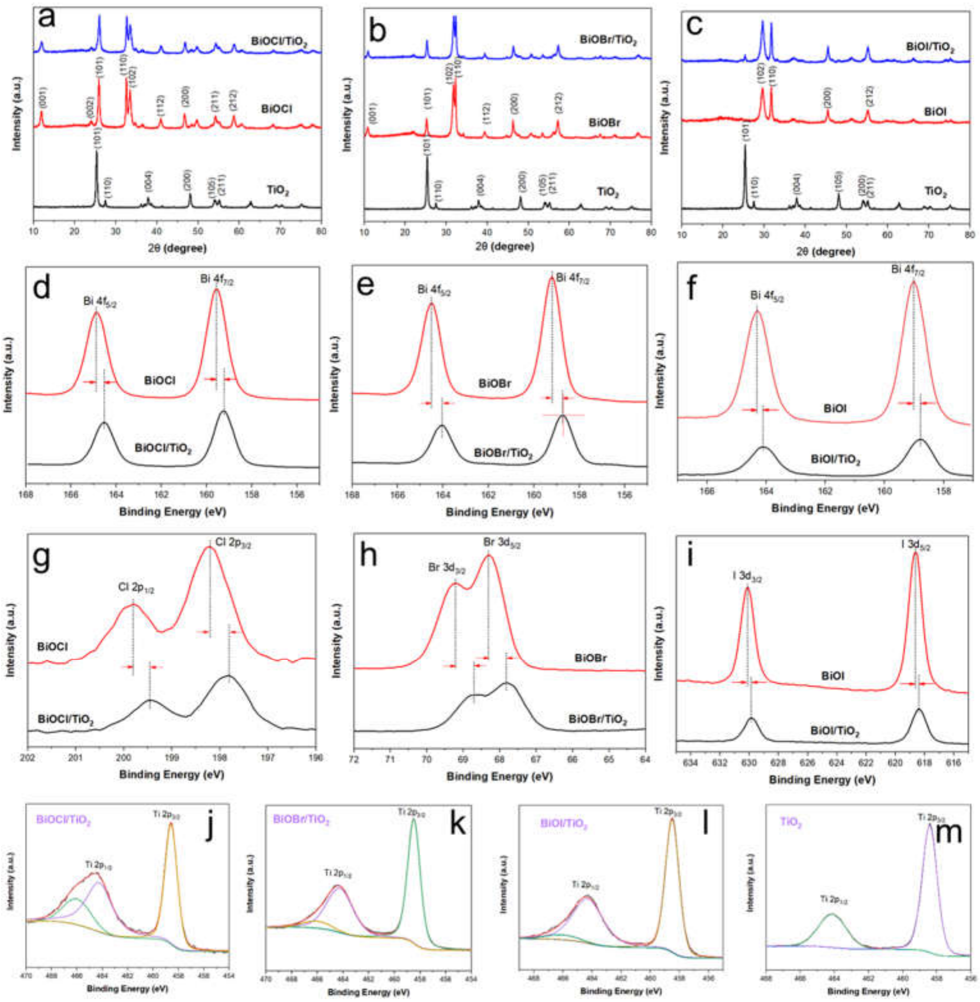

Figure 6.1 XRD spectra of BiOX and BiOX/TiO$_2$ catalysts (a-c); XPS spectra of Bi 4f (d-f), Cl 2p (g), Br 3d (h), I 3d (i) of BiOX and BiOX/TiO$_2$; XPS spectra of Ti 2p (j-m) of BiOX/TiO$_2$ and TiO$_2$.

XPS was conducted to study the compositions and the elemental states of BiOX, TiO$_2$ and BiOX/TiO$_2$ composites. Fig. 1d-m displayed the details of Bi4f, Cl2p, Br3d, I3d and Ti2p. The Bi4f$_{5/2}$ and Bi4f$_{7/2}$ peaks located at ~164.5 and ~159.2 eV are the characteristic peaks of Bi^{3+} (Fig. 6.1d-f) (Wang et al. 2017a). The peaks centered at ~199.8 and 198.2 eV are attributed to Cl 2p$_{1/2}$ and Cl 2p$_{3/2}$ signals, which are the characteristics of Cl^{-} in BiOCl (Fig. 6.1g) (Li et al. 2016c). The XPS peaks at 69.2 and 68.3 eV of Br 3d$_{3/2}$ and Br 3d$_{5/2}$ are the featured peaks of Br^{-} in BiOBr (Fig. 6.1h). Two primary peaks of the XPS spectra of I 3d are located at 630.1 and 618.6 eV, which could be attributed to I 3d$_{3/2}$ and I 3d$_{5/2}$, respectively (Fig. 6.1i). It should be noted that all binding energies of Bi and X for TiO$_2$/BiOX were 0.2 ~ 0.5 eV lower than those of

BiOX, indicating that electrons were transferred to BiOX from TiO_2 (Yu et al. 2021). As can be seen from Fig. 6.1j-m, the chemical binding energies located at 458.4 eV, and 464.1 eV could be ascribed to Ti^{4+} in TiO_2. The peak at ~ 466.0 eV of Ti^{4+} in BiOX/TiO_2 might be due to the formation of Ti-X bond (Akhavan and Ghaderi 2009, Wang et al. 2019c). Thus, BiOX connected with TiO_2 via strong chemical bonds, rather than forming a physical mixture. Especially, BiOCl connected with TiO_2 tightly due to the higher content of 466.1 eV of Ti^{4+} in BiOCl/TiO_2. The peak at 466.0 eV of Ti^{4+} in BiOBr(I)/TiO_2 seemed quite weak, due to the decreased negativity of Br and I, compared with Cl.

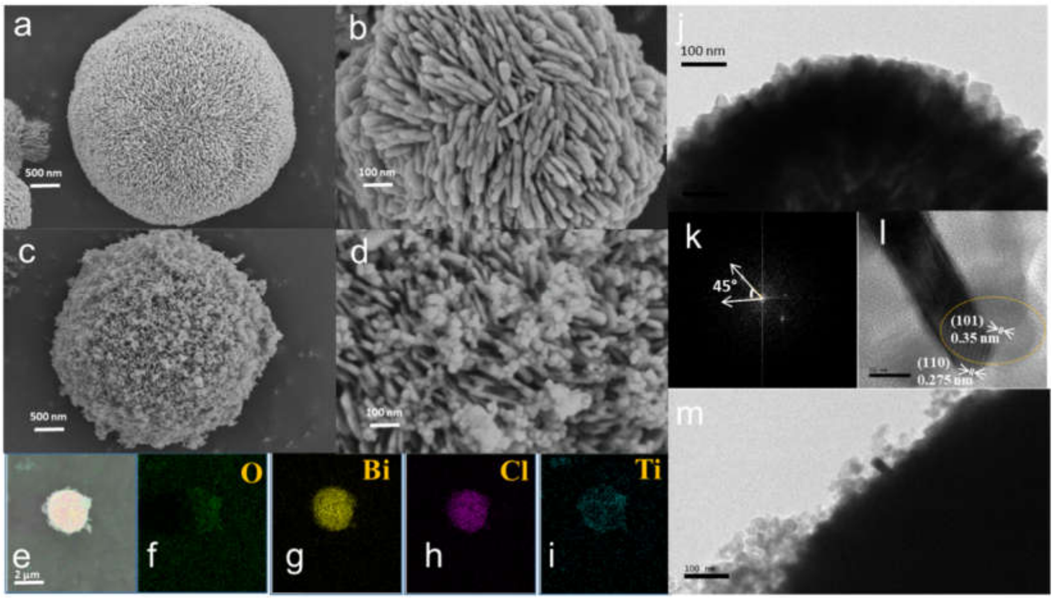

Figure 6.2 SEM images of BiOCl (a, b), BiOCl/TiO_2 (c, d) and element mapping of O (f), Cl (g), Bi (h) and Ti (i) in BiOCl/TiO_2; TEM image (j) and SAED pattern (k) of BiOCl; HRTEM image (l) and TEM image (m) of BiOCl/TiO_2

The morphologies of BiOX, TiO_2 and BiOX/TiO_2 were observed by SEM images (Fig. 6.2; Fig. 6.3; and Fig. 6.4). The prepared BiOCl and BiOBr samples are 3D flower-like microspheres, assembled by 2D nanorods (Fig. 6.2a-b; and Fig. 6.3a-b). After the introduction of TiO_2, BiOCl/TiO_2 and BiOBr/TiO_2 exhibit nonuniform flower-like spherical morphology. In addition, BiOCl and BiOBr nanorods of smaller sizes were observed in BiOCl/TiO_2 and BiOBr/TiO_2 composites (Fig. 6.2c-d; and Fig. 6.3c-d). The smaller BiOCl(Br) nanorods might facilitate the transfer of charge carriers from internal to surface for redox reactions (Linic et al. 2011). The morphology of BiOI is 3D flower-like microspheres assembled by 2D nanosheets (Fig. 6.4a-b). Moreover, more TiO_2 nanoparticles were also observed in the BiOI/TiO_2 composite (Fig. 6.4c-d). The elemental mapping images showed the evenly distributed Bi, O, X (Cl, Br, I) and Ti in the catalysts (Fig. 6.2e-i; Fig. 6.3e-i; and Fig. 6.4e-i), further demonstrating the successful preparation of BiOX/TiO_2 composites.

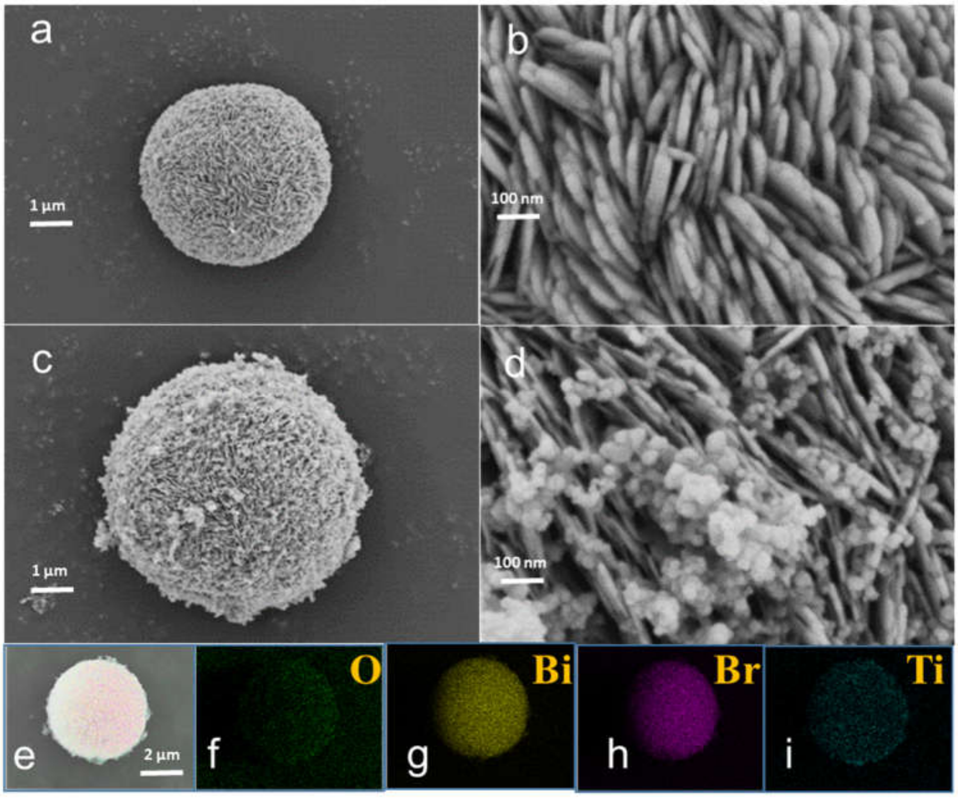

Figure 6.3 SEM images of BiOBr (a, b), BiOBr/TiO_2 (c, d) and element mapping of O (f), Br (g), Bi (h) and Ti (i) in BiOBr/TiO_2.

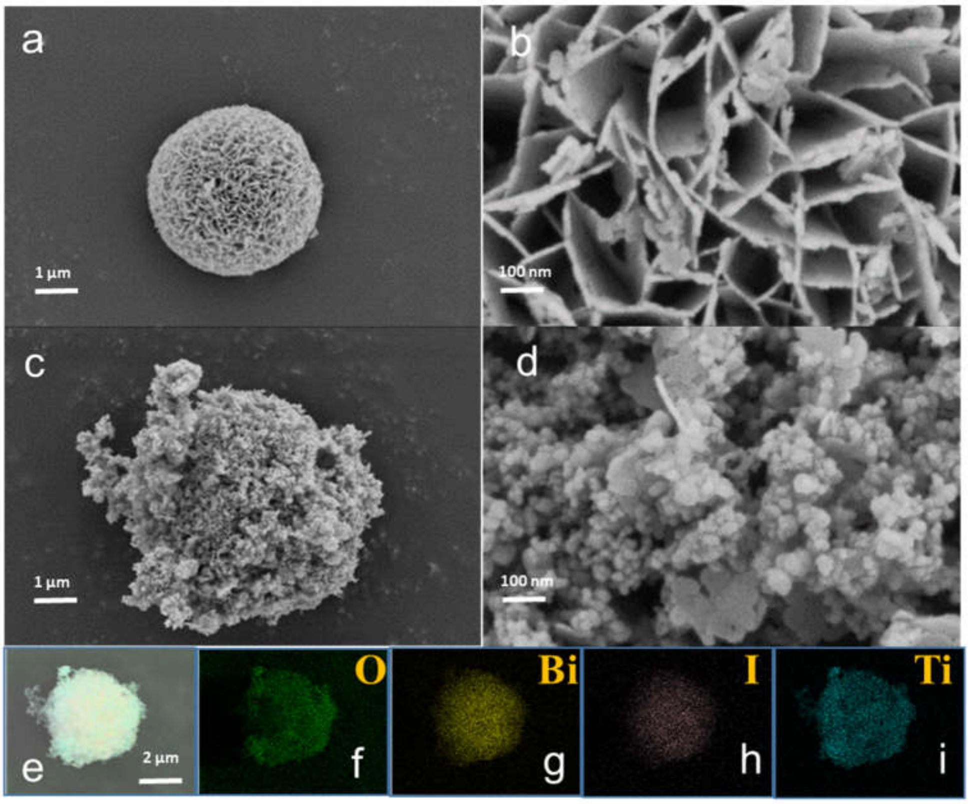

Figure 6.4 SEM images of BiOI (a, b), BiOI/TiO_2 (c, d) and element mapping of O (f), I (g), Bi (h) and Ti (i) in BiOI/TiO_2.

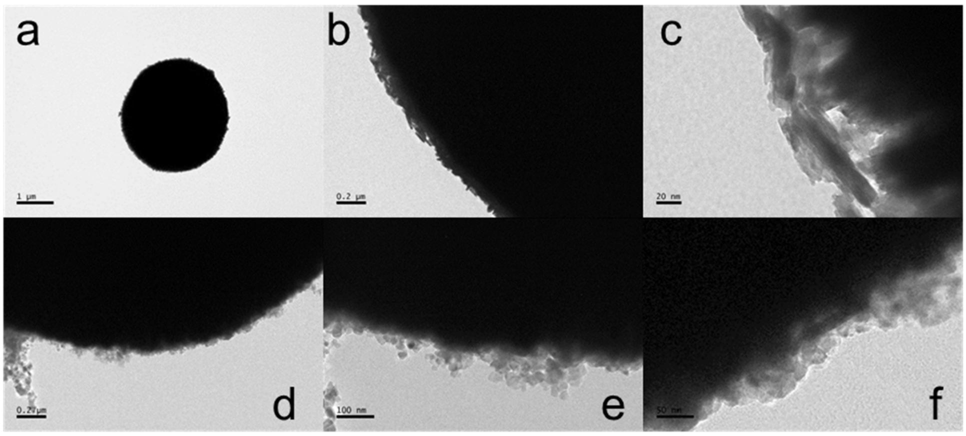

Figure 6.5 The TEM images of BiOBr (a-c) and BiOBr/TiO_2 (d-f) photocatalysts.

Fig. 2j-m displayed the TEM images of BiOCl and BiOCl/TiO_2 photocatalysts. The size of BiOCl nanorods became smaller when combined with TiO_2 (Fig. 6.2j and Fig. 6.2m), which is in accordance with the SEM results. The SAED pattern (Fig. 6.2k) indicated the single crystalline structure of BiOCl. The angle between [110] and [200] planes is calculated to be 45°, which is in accordance with the angle labelled in the SAED pattern (Guan et al. 2013, Jiang et al. 2012). Fig. 6.2l demonstrated the well crystalline structure of BiOCl nanorods. The typical TiO_2 [101] planes with the characteristic lattice fringes of 0.35 nm were observed which is shown in the circled area (Wei et al. 2018). The direct contact between TiO_2 and BiOCl was also noticed in Fig. 2d. The interplanar lattice spacing of 0.275 nm was found in the uncovered area of the nanorod, which corresponded to the [110] atomic facet of BiOCl. These results provided direct evidence that TiO_2 leaned on the [110] plane of BiOCl, consistent with the XRD results. The TEM images of BiOBr (Fig. 6.5a-c), BiOBr/TiO_2 (Fig. 6.5d-f), BiOI (Fig. 6.6a-c), BiOI/TiO_2 (Fig. 6.6d-f) were also listed. The combination of BiOI/BiOBr with TiO_2 can be clearly observed.

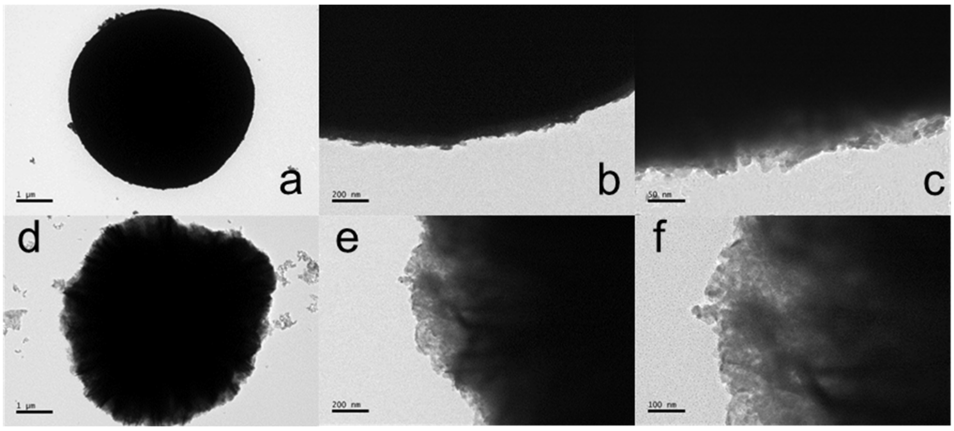

Figure 6.6 The TEM images of BiOI (a-c) and BiOI/TiO_2 (d-f) photocatalysts.

The photoluminescence spectroscopy (PL) of BiOX, TiO_2 and BiOX/TiO_2 catalysts was also collected with the excitation wavelength of 241 nm (Fig. 6.7). A wide peak between 340 nm and 480 nm was observed for these samples. The lowest fluorescence intensity of BiOCl/TiO_2 indicated that the lower recombination rate of photo-induced charge carriers in the composite. BiOBr(I) have similar fluorescence intensities with BiOBr(I)/TiO_2 (Fig. 6.7).

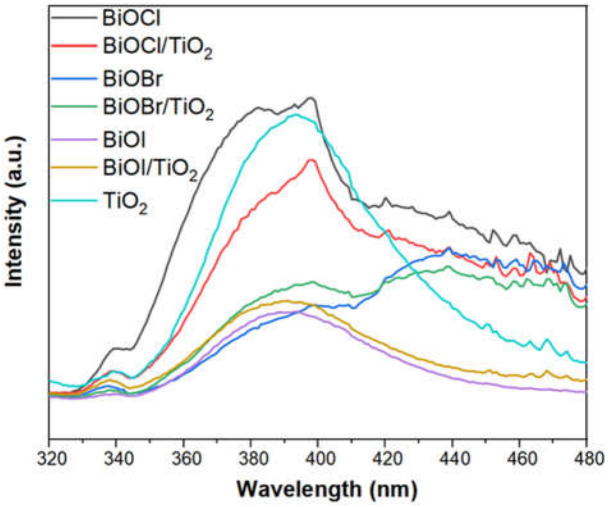

Figure 6.7 PL spectra of BiOX, TiO_2 and BiOX/TiO_2 photocatalysts.

6.3.2 Photocatalytic decomposition of PFOA by BiOX and BiOX/TiO_2 catalysts

BiOX and BiOX/TiO_2 catalysts were used to degrade PFOA under UV 254 nm light irradiation. As shown in Fig. 6.8a-c, BiOX/TiO_2 exhibited significantly enhanced performance than BiOX and TiO_2 for the degradation of PFOA. Only 18% of PFOA was decomposed by TiO_2, after irradiation for 8h. In the presence of BiOI, BiOBr and BiOCl, 48%, 33% and 50% of PFOA was degraded, respectively. While in the presence of BiOI/TiO_2, BiOBr/TiO_2 and BiOCl/TiO_2, the decomposition ratio of PFOA dramatically increased to 88%, 100% and 96%, respectively. These results well demonstrated that combining BiOX with TiO_2 could significantly intensify the photooxidation of PFOA.

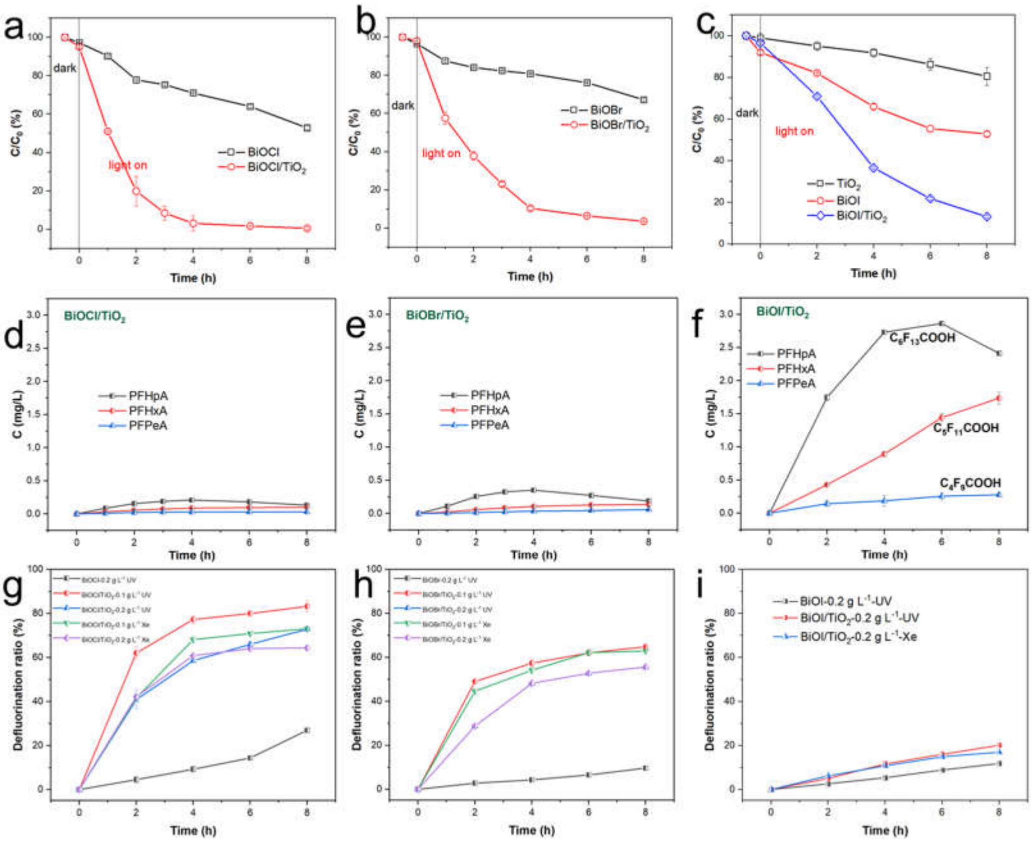

Figure 6.8 The kinetics of the photocatalytic degradation of PFOA (a-c) and the generation of shorter-chain intermediates (d-f) under UV irradiation in the presence of BiOX and BiOX/TiO_2 catalysts. (Reaction conditions: catalyst dosage, 0.2 g L^{-1}; 254 nm UV light); The defluorination ratios of PFOA in the presence of BiOX and BiOX/TiO_2 catalysts after 8h irradiation under UV 254 nm or Xe lamp (g-i).

In addition, shorter-chain intermediates were detected during the degradation of PFOA, as shown in Fig. 6.8d-f. PFHpA ($C_6F_{13}COOH$), PFHxA ($C_5F_{11}COOH$) and PFPeA (C_4F_9COOH) were detected as the primary intermediates of PFOA decomposition. Shor-chain PFCAs (C= 3, 2) were also detected at a low concentration (<0.02 mg L^{-1}). The concentration of PFHpA increased first during the first 4-h irradiation, reaching the maximum concentration in the presence of BiOCl(Br)/TiO_2 catalysts, and then gradually decreased, while other PFCAs ($C_5F_{11}COOH$ and C_4F_9COOH) increased continuously during 8-h irradiation. Differently, in the presence of BiOI/TiO_2, the concentration of PFHpA reached the maximum in 6 h. It indicates that PFOA degraded stepwise in BiOX/TiO_2/UV systems, with one CF_2 removed in one step. Moreover, it could be noticed that the concentrations of shorter-chain PFCAs in BiOI/TiO_2 system were significantly higher than the BiOCl(Br)/TiO_2 system.

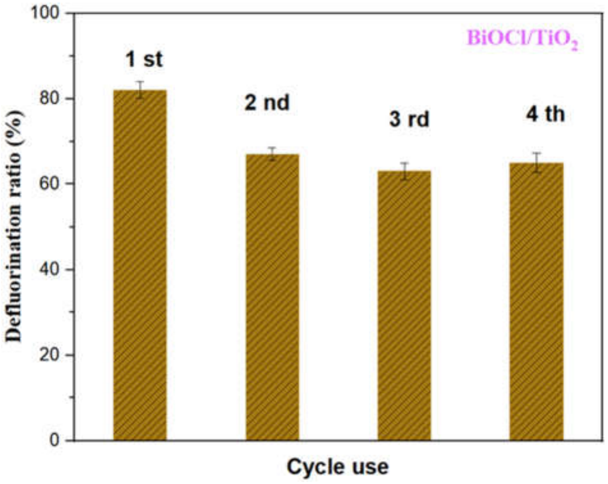

Figure 6.9 The cycle use of BiOCl/TiO_2 for the photocatalytic defluorination of PFOA.

Defluorination ratio is an important indicator to see whether PFOA is completely decomposed. After irradiation for 8h, the concentrations of fluoride ions were detected. The defluorination ratios in the presence of BiOX and BiOX/TiO_2 were listed in Fig. 6.8g-i. We can see that BiOCl/TiO_2 exhibited the best performance for PFOA defluorination under UV or Xe lamp irradiation (Fig. 3g). A defluorination ratio of 82% was obtained in the BiOCl/TiO_2/UV system, with the catalyst dosage of 0.1g L^{-1}. While the defluorination ratio slightly decreased to 73% when the concentration of BiOCl/TiO_2 increased to 0.2 g L^{-1}. The decrease of the defluorination ratio with the increase of the catalyst dosage, was due to the high dispersity of BiOCl/TiO_2 photocatalyst. The possible reason could be that the decrease of BiOCl/TiO_2 density in solution facilitated light transmission to the bottom level of the reactor (Egerton and Tooley 2004). Under Xe lamp irradiation, the defluorination ratio was 73% (or 63%) in the presence of 0.1 (or 0.2) g L^{-1} of BiOCl/TiO_2. BiOCl obtained a defluorination ratio of 27%, which was much lower than that of BiOCl/TiO_2. In the BiOBr/TiO_2/UV systems, the defluorination ratios were 65% and 59% for 0.1 g L^{-1} and 0.2 g L^{-1}, respectively (Fig. 3h). Under Xe lamp irradiation for 8h, the defluorination ratios were 63% and 55%, for 0.1 g L^{-1} and 0.2 g L^{-1}, respectively. Only a defluorination ratio of 10% was obtained in the presence of 0.2 g L^{-1} BiOBr under UV 254 nm irradiation for 8 h. BiOI/TiO_2 also demonstrated a higher defluorination ratio of ~20% compared with 12% of BiOI under UV 254 nm irradiation (Fig. 3i). BiOI/TiO_2 demonstrated a defluorination ratio of 16% under Xe lamp irradiation (Fig. 3i). The higher defluorination ratio obtained by BiOCl(Br)/TiO_2 systems led to the much lower concentrations of shorter-chain PFCAs than those in the BiOI/TiO_2 system. These results demonstrated the better performance of BiOX/TiO_2 than BiOX. Among BiOX/TiO_2 catalysts, BiOCl/TiO_2 was the most efficient for the decomposition and defluorination of PFOA. The electric energy required to treat 1000 L of PFOA solution is estimated to be 640 kW•h. As displayed in Table 6.2, BiOCl/TiO_2 exhibited better performance than the previously reported semiconductors for photocatalytic defluorination of PFOA. In addition, the cyclic test of BiOCl/TiO_2 manifested that it possessed good stability during the four cycles (Fig. 6.9). And BiOCl/TiO_2 achieved a high defluorination ratio of ~64% of PFOA in the 4th run.

Table 6.2 Photocatalytic removal of PFOA over different semiconductor photocatalysts.

Photochemical catalyst	Pollutant	Light wavelength	Power	Conditions	Reaction time	Degradation ratio &Defluorination ratio	Ref.
Sheaf-like Ga_2O_3	PFOA	254 nm	14 W	C_0=0.5 mg L^{-1}	45 min	100% & 60%	(Shao et al. 2013a)
Needle-like Ga_2O_3	PFOA	254 nm	14 W	C_0=0.5 mg L^{-1}	1 h	100% & 58%	(Shao et al. 2013b)
In_2O_3	PFOA	254 nm	23 W	C_0=40 mg L^{-1}	4 h	80% & 33%	(Li et al. 2012a)
Fe-zeolites	PFOA	365 nm	4W	C_0=48 μM	24h	100%&40%	(Qian et al. 2020)
BiOF	PFOA	Hg lamp	500 W	C_0=15 mg L^{-1}	6h	100%&–	(Wang et al. 2021a)
BiOCl/TiO_2	PFOA	254 nm	32 W	C_0=10 mg L^{-1}	8h	100%&82%	This work

6.3.3 The coordination mode and reactive oxygen species

The coordination mode of PFOA with TiO_2, BiOX and BiOX/TiO_2 catalysts were investigated by the DRIFTS spectra (Fig. 6.10a). The peaks at 1672 and 1425 cm^{-1} of TiO_2/PFOA corresponded to the asymmetric and symmetric stretching modes of –COO group (Li et al. 2012b, Rotzinger et al. 2004b). Upon adsorption on BiOI, BiOI/TiO_2 and BiOCl/TiO_2, the peaks of –COO group appeared at 1624 and 1418 cm^{-1}. According to the stretching frequencies of carboxylate, a smaller Δv value ($\Delta v = v_{as}$ (COO$^-$) - v_s (COO$^-$)) was correlated with a tighter coordination mode of PFOA with catalysts (Gao et al. 2009, Song et al. 2017). The smaller Δv value (206 cm^{-1}) for PFOA adsorbed on BiOX, and BiOX/TiO_2 than the Δv value (247 cm^{-1}) of PFOA adsorbed on TiO_2, indicated that a bidentate coordination mode was formed between PFOA and BiOX or BiOX/TiO_2.

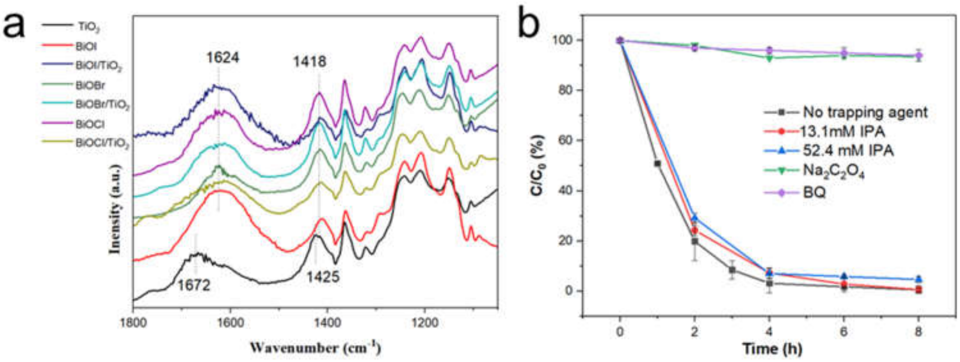

Figure 6.10 The DRIFTS spectra of PFOA adsorbed on TiO_2, BiOX and BiOX/TiO_2 photocatalysts (a); and the effects of different scavengers on the photocatalytic degradation of PFOA in the presence of BiOCl/TiO_2 (b). (Reaction conditions: BiOCl/TiO_2 dosage: 0.2 g L^{-1}; $Na_2C_2O_4$: 5 mM; BQ: 5 mM; PFOA: 10 mg L^{-1})

Scavenging experiments were carried out to probe the categories of reactive oxygen species (ROS) and identify their roles during the photocatalytic decomposition of PFOA (Fig. 6.10b). The addition of $Na_2C_2O_4$ (5 mM, a quencher for h$^+$) or *p*-benzoquinone (BQ, 5mM, a quencher for $O_2^{\bullet-}$) completely inhibited PFOA decomposition, demonstrating the important roles of photo-induced holes and $O_2^{\bullet-}$. In contrast, when isopropanol (IPA, 13.1 mM & 52.4 mM, a quencher for •OH) was added in the system, there was no significant deterioration of PFOA removal, suggesting that •OH did not participate in the decarboxylation process of PFOA.

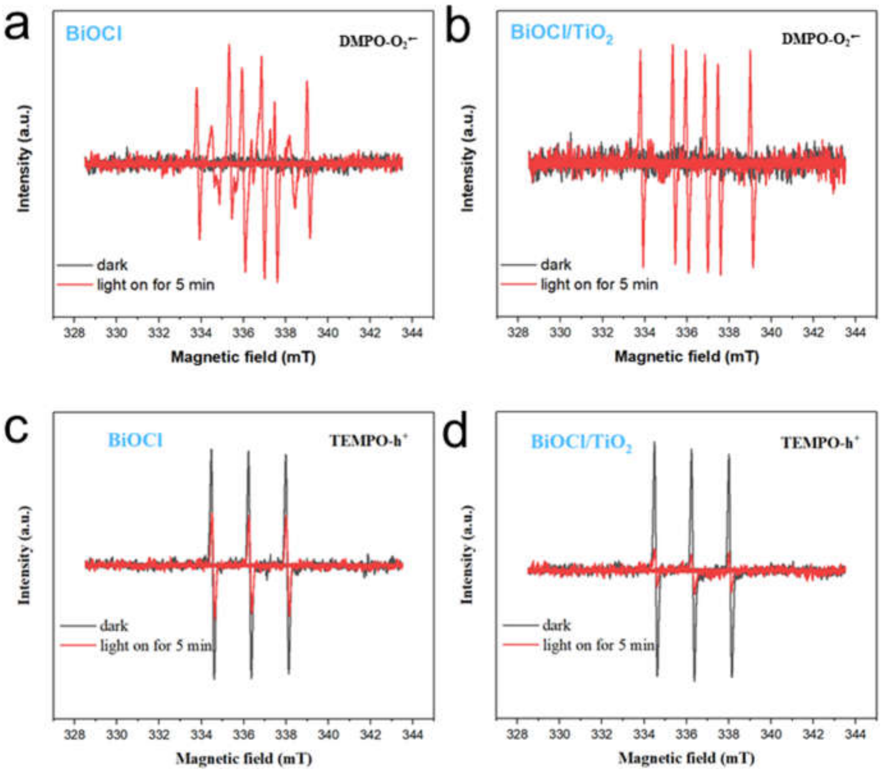

Figure 6.11 ESR signals for the detection of $O_2^{\bullet-}$ in the presence of BiOCl (a) and BiOCl/TiO_2 (b); and TEMPO signals for the records of h^+ in BiOCl (c) and BiOCl/TiO_2 (d) systems.

Active species generated during photocatalytic processes of the BiOCl/TiO_2 system were detected by ESR (Fig. 6.11). 2,2,6,6-tetramethylpiperidine-1-oxyl free radical (TEMPO) was adopted as the h^+ scavenger, and 5,5-dimethyl-1-pyrroline-N-oxide (DMPO) was used for scavenging $O_2^{\bullet-}$ (Peng et al. 2020). No signals of $O_2^{\bullet-}$ were detected in the absence of light. When light was on, $O_2^{\bullet-}$ were generated in the BiOCl/TiO_2 system (Fig. 6.11a). While in the BiOCl system, the irregular signals maybe caused by other oxidative products generated under light irradiation (Fig. 6.11b). The regular signals of $O_2^{\bullet-}$ in the BiOCl/TiO_2 system may be due to the generation of ample photo-induced electrons, which could reduce O_2 to $O_2^{\bullet-}$ (Clément et al. 2005). The signals of TEMPO were strong under dark conditions. After irradiation for 5 min, the intensities of TEMPO became weaker due to the decomposition of TEMPO by photo-induced holes (Peng et al. 2020). The sharp decrease of TEMPO in the presence of BiOCl/TiO_2 indicated that more photo-induced holes were generated on BiOX/TiO_2 than BiOX (Fig. 6.11c; and Fig. 6.11d).

6.3.4 Self-Induced Inner Electric Fields in BiOX and Band Alignment between BiOX and TiO_2

When illuminated under the light, photo-induced electrons could be generated in BiOX and then injected into TiO_2 nanoparticles along the [001] direction of BiOX, guided by the driving forces of IEF in BiOX (Li et al. 2021). Simultaneously, the photo-generated holes in TiO_2 nanoparticles will flow into BiOCl in the perpendicular direction of [001] slabs of BiOX (Ouyang et al. 2018). The holes reaching the surface of BiOCl would attack the carboxyl group of PFOA molecules. According to the XRD patterns, TiO_2 combined with BiOX nanosheets along the [110] facet, which was the pathway of hole transfer from TiO_2 to BiOX.

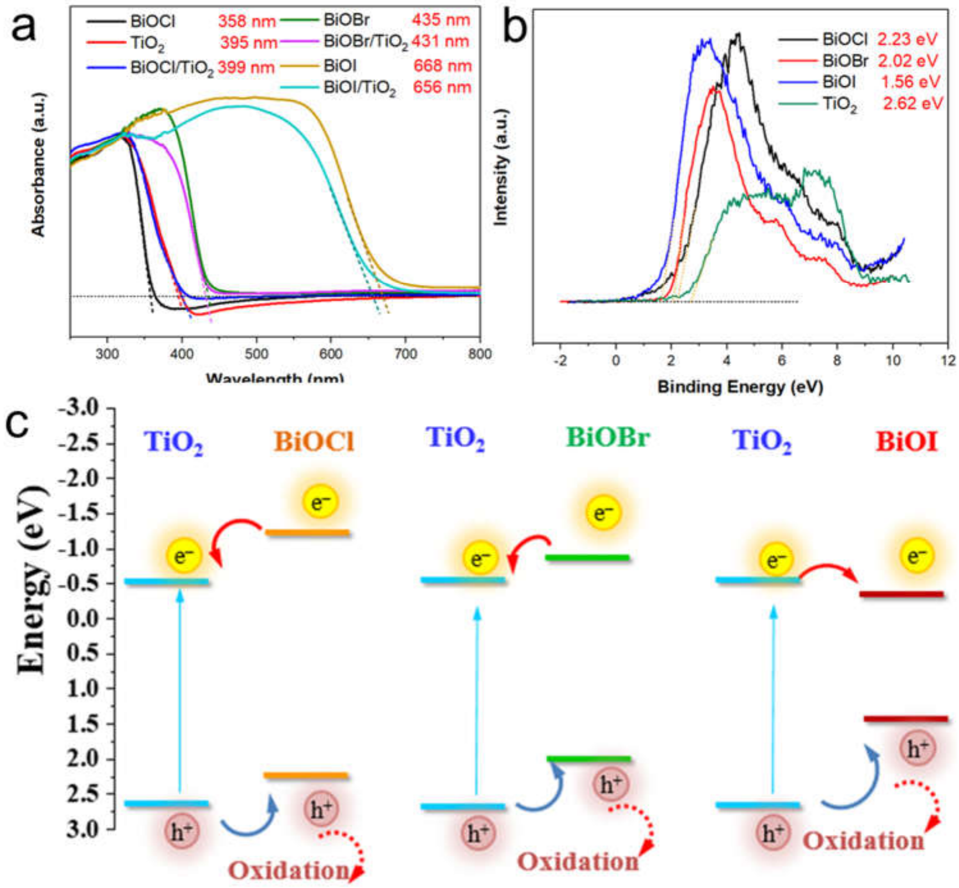

Figure 6.12 UV-vis absorption spectra of BiOX and BiOX/TiO_2 catalysts (a); valance band XPS spectra of BiOX and TiO_2 catalysts (b); The illustration of band structures of BiOX/TiO_2 heterostructures (c).

The UV/Vis diffuse absorption spectra of BiOX and BiOX/TiO_2 catalysts were recorded to investigate their light-harvesting abilities. As indicated in Fig. 6.12a, the

TiO_2 nanoparticles presented negligible absorption in the visible light range, exhibiting a steep absorption edge situated at around 395 nm. The absorption wavelengths for pure BiOCl and BiOCl/TiO_2 were 358 nm, and 399 nm, respectively. Pure BiOBr exhibits an absorption wavelength of 435 nm. Consequently, the BiOBr/TiO_2 composite presented an absorption edge of 431 nm. The absorption edge of BiOI was extended up to 668 nm, demonstrating excellent visible light absorption ability. Different from TiO_2, the absorption of BiOI/TiO_2 composition was greatly extended to the visible light range with the light absorption edge up to 656 nm. The band gap values of these semiconductor photocatalysts can be calculated based on the formula $E_g = 1240/\lambda_g$, where λ_g is the band gap wavelength (Shenawi-Khalil et al. 2012, Xue et al. 2017). Accordingly, the band gap energies of TiO_2, BiOX and BiOX/TiO_2 were determined to be 3.14 eV for TiO_2, 3.46 eV for BiOCl, 2.85 eV for BiOBr, and 1.86 for BiOI.

The valence band (VB) of BiOX and TiO_2 catalysts were determined by XPS valence spectra, (Fig. 6.12b). BiOCl, BiOBr, BiOI and TiO_2 displayed a VB with the edge at ~2.23, 2.02, 1.56 and 2.62 eV, respectively. The conduction band (CB) position could be estimated according to $E_{\mathrm{CB}}=E_{\mathrm{VB}}-E_{\mathrm{g}}$. The corresponding CB minimum for BiOCl, BiOBr, BiOI and TiO_2 would occur at about –1.23, –0.83, –0.30 and –0.52 eV. The band gap estimated from the UV-vis spectra and the band positions estimated from XPS results are in good agreement the values reported in the literatures (Chen et al. 2014, Guo et al. 2018, Wang et al. 2015). Therefore, the band alignment of TiO_2 and BiOX were demonstrated in Fig. 6.12c. When n-type TiO_2 contacted with p-type BiOX, the p-n junction was formed. For BiOCl/TiO_2 and BiOBr/TiO_2, the photo-induced electrons were transferred from CB of BiOCl/BiOBr to TiO_2, and the photo-induced holes form VB of TiO_2 to BiOCl/BiOBr. Thus, the photo-induced holes would accumulate in VB of BiOCl/BiOBr, which subsequently oxidized PFOA coordinated with BiOX. While for BiOI/TiO_2, CB of BiOI was higher than TiO_2 and VB of BiOI was lower than TiO_2. Both the photo-induced electrons and holes would flow from TiO_2 to BiOI, leading to the accumulation of photo-induced electrons and holes in CB and VB of BiOI. However, the accumulated carriers in BiOI would result in a higher recombination rate. BiOCl(Br)/TiO_2 achieved better performance for photocatalytic degradation of PFOA compared with BiOI/TiO_2, because of the spatial separation of carriers in each component to mitigate recombination.

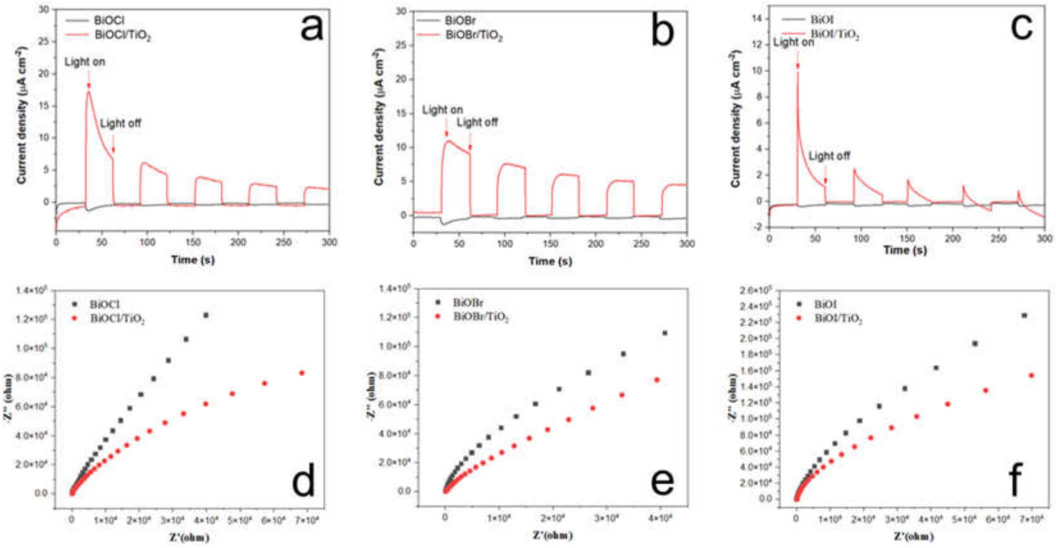

Figure 6.13 Photocurrent enhancements of BiOX/TiO_2 compared with BiOX (a-c), and the EIS spectra of BiOX and BiOX/TiO_2.

The i-t curves and EIS spectra of BiOX and BiOX/TiO_2 photocatalysts were recorded to further investigate the separation and transfer of photo-generated electrons and holes. As shown in Fig. 6.13a-c, the photo-induced current density of BiOX/TiO_2 composites largely suppressed that of the pure BiOX photocatalyst. In addition, the semicircle radius of BiOX/TiO_2 was smaller than that of BiOX in the EIS plots (Fig. 6.13d-f), which reflected faster charge migration of BiOX/TiO_2 (Sun et al. 2015). All these results demonstrated the more efficient separation and transfer of photo-induced charges of BiOX/TiO_2, thus leading to the generation of more ROS and higher defluorination ratio of PFOA.

6.3.5 Mechanisms for the photocatalytic degradation of PFOA

The photocatalytic degradation pathway of PFOA is illustrated in Figure 6.14.Photo-induced holes and electrons were generated by the irradiation of UV or UV-visible light. The electrons generated would then react with O_2 to produce $O_2^{\bullet -}$. The decomposition was initiated by the decarboxylation of PFOA induced by the photo-induced holes and $O_2^{\bullet -}$, which was a thermal-dynamically favourable process (Wang et al. 2021a). $C_7F_{15}\bullet$ was formed and then reacted with H_2O/O_2 to produce unstable $C_7F_{15}OH$, following the loss of a HF to form $C_6F_{13}COF$. $C_6F_{13}COF$ was further hydrolysed and converted to $C_6F_{13}COOH$ (PFHpA). $C_6F_{13}COOH$ would undergo similar ways to generate $C_5F_{11}COOH$ (PFHxA), and then to PFPeA. Every time a CF_2

was removed until finally mineralized to fluoride ions and carbon dioxide (CO_2). Previous studies showed that it was thermodynamically favourable to form $C_6F_{13}^-$, $C_5F_{11}^-$ and $C_4F_9^-$; therefore PFHpA, PFHxA and PFPeA were mainly detected as PFOA decomposition intermediates (Gu et al. 2016b). Moreover, the concentrations of these degradation intermediates detected in BiOCl(Br)/TiO_2 systems were significantly lower than that in the BiOI/TiO_2 system, indicating the high efficiency of BiOCl(Br)/TiO_2 for both short-chain PFCAs and PFOA.

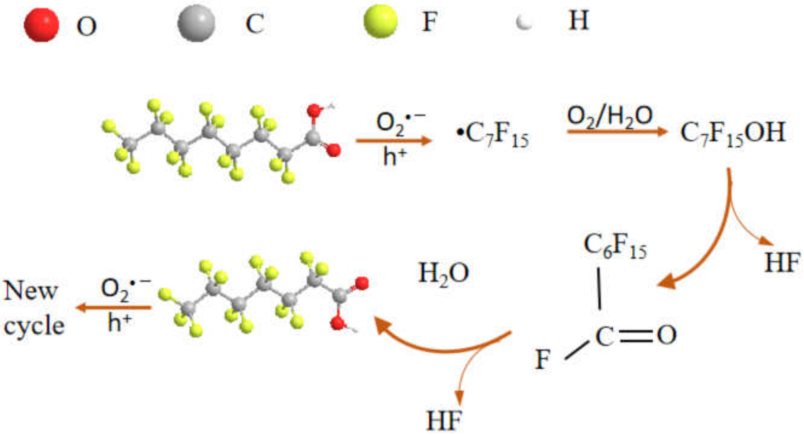

Figure 6.14 Illustration of the photocatalytic degradation pathway of PFOA over BiOCl/TiO_2.

6.4 Conclusion

The BiOX/TiO_2 composites were synthesized by a hydrothermal approach and demonstrated significantly enhanced performance for photocatalytic degradation of PFOA. The highest defluorination ratio was obtained in the BiOCl/TiO_2 system because of the efficient charge separation efficiency. Inner electric field in BiOX could shuttle the photo-induced electron from BiOX to TiO_2 in the [001] direction, which is perpendicular to the [110] facet. Photo-induced electrons would react with O_2 and produced $O_2^{\bullet-}$ to decompose PFOA, and the photo-induced hole could transfer from TiO_2 to BiOX through the [110] facet, which was verified by the characterizations. Therefore, the formation of BiOX/TiO_2 heterojunction could benefit charge transfer and facilitate PFOA decomposition.

CHAPTER 7

Photo-induced bismuth single atoms on TiO_2 for highly efficient photocatalytic defluorination of PFOA: the ionization of the C-F bond.

7.1 Introduction

Perfluoroalkyl substances (PFAS) are a group of persistent and mobile fluoro-organic chemicals that have been detected in many water bodies, and their recommended sage concentrations in drinking water are as low as 6 ng L^{-1} (Costanza et al. 2019, Post et al. 2009). Perfluorooctanoic acid (PFOA) has various utilizations in life and work supplies, and it is widely detected in surroundings. Developing efficient photocatalysts for the removal of PFOA in wastewater and natural water systems are urgently required (Xu et al. 2020a). In general, PFOA is stable in the environment and resists natural degradation or artificial treatment processes (Liu et al. 2020). As a result, these chemicals persist and accumulate in the environment, particularly in water, soil, and sediment. Photocatalytic approaches have been demonstrated to be an efficient method for the mineralization of PFASs under mild conditions (Qu et al. 2016). The key of the technology is to develop photocatalysts of high efficiency and low cost.

Single-atom catalysts (SACs) have gained extensive and increasing attention in recent years (Gao et al. 2020). Compared with conventional catalysts with nano sizes, the atomically dispersed active sites of SACs afford the maximum atomic utilization efficiency, optimised electronic properties, and consequently excellent catalytic activity (Lee et al. 2019). The unique features and well-defined coordination structures make SACs an ideal platform to understand the catalytic mechanism from the molecule level. The outstanding catalytic activity of SACs stems from the unique electronic structure of single metal atoms and the coupling of single metal atoms and supports (electronic metal–support interaction) (Gao et al. 2016). In addition to serving as active sites, incorporating sing-atom metals into catalysts can modulate the electronic structure of the support (Chu et al. 2021b). Further studies revealed that atomically controlled ultrafine metal clusters possessed unprecedently high activity, such as Pt_2 dimers(Yan et al. 2017) and neighbouring Pd atoms (Chu et al. 2021a). However, the synthesis of atomically controlled SACs and ultrafine metal clusters remains a grand challenge.

TiO_2 is a chemically stable, economically feasible commercial semiconductor. However, the low quantum efficiency of pristine TiO_2, low visible light utilization efficiency and the rapid charge carrier recombination further deteriorates its activity in photocatalysis (Grabowska et al. 2012). Construction of metal/TiO_2 heterojunctions would promote the charge carrier separation, enhance the light absorption ability of TiO_2, therefore significantly promoting the photocatalytic performances (Daghrir et al.

2013). Single atom noble metals, such as palladium (Pd) and platinum (Pt), have been loaded onto semiconductors to optimize the physical and optical properties. Huang et. al demonstrated that the single-atom Pt (Pt_1) decorated silicon carbide can reductively cleave C-F bonds of PFOA under UV light irradiation (Huang et al. 2018). Site-specifically deposited Pt_1 on TiO_2 could enhance hydrogen spill over onto the TiO_2 surface. Then, PFOA can be decomposed via hydrodefluorination by the generated hydrogen (Weon et al. 2021). Moreover, Pt_1 would selectively deposit onto the reductive sites of tailored TiO_2 to attract the photo-induced electrons. Considering the high price of precious metals, some inexpensive metals (e.g., bismuth (Bi)) with similar properties have been considered as the potential alternative (Karimi-Nazarabad et al. 2021). Since the compositions and structures of SACs have great impacts on the catalytic performances, rationally manipulating the structures with atomic-level precision is of great importance (Pan et al. 2020).

Bi is a non-precious semimetal and has great potential to be used as an alternative cocatalyst in photocatalysis due to its surface plasmon resonance (SPR) effect (Dong et al. 2015). Nanoscale Bi demonstrated superior performance than bulk Bi, due to the larger specific surface area (SSA), strong light absorption, and locally-intensified SPR effect of nanoscale Bi (He et al. 2018). In comparison, Bi single atom (SA) catalysts were expected to demonstrate enhanced activity due to the monodispersity of Bi SA. However, only a few studies have been reported to investigate the catalytic performance of Bi single atoms and the associated mechanisms (Yang et al. 2020a, Zhang et al. 2019b). Up to date, there yet been any studies on the photocatalytic performance of Bi single atoms as a cocatalyst in semiconductors. Bi single atom-based materials are typically synthesized via high-temperature pyrolysis (up to 900 or 1000 °C) (Xi et al. 2021, Zhang et al. 2019a), which is energy-intensive and requires harsh reaction conditions. A facile green method is needed for the preparation of Bi-based photocatalysts of low cost and high efficiency. Moreover, previous studies typically prepared BiOCl by hydrothermal methods, which require relatively high temperature and organic solvents (Jiang et al. 2012, Yang et al. 2021).

Wet chemistry method has attracted various attention due to easy operation and feasibility for up-scale synthesis (Chen et al. 2018). Generally, the voids or defects in supports are constructed to anchor single atoms (Ida et al. 2015). Molecular structure cages are also considered for the confinement of single atoms (Kistler et al. 2014). Other spatial confinement strategies have also been demonstrated for the construction of SACs. Wu et al. reported an iced-photochemical reduction method for the preparation of Pt_1/TiO_2, which firstly freeze the metal precursor solution to inhibit the motion and aggregation of metal ions (Wei et al. 2017).

In this study, we found that Bi single atoms can be generated on the surface of TiO_2 using $Bi(NO_3)_3$ as the precursor with the help of UV light irradiation at room temperature, denoted as N-Bi/TiO_2. BiOCl nanoclusters were generated over TiO_2 under UV light irradiation (denoted as Cl-Bi/TiO_2), when $BiCl_3$ was used as the precursor. Cl-Bi/TiO_2 and N-Bi/TiO_2 demonstrated excellent photocatalytic activities for the efficient photocatalytic decomposition and defluorination of PFOA. We investigated the primary reactive oxygen reactive species (ROS) accounting for PFOA removal, such as photo-induced holes and superoxide radical ($O_2^{\bullet-}$). Bi-SA/TiO_2 heterojunctions exhibited excellent photocatalytic activity and stability for applications in the remediation of PFOA and associated micropollutants.

7.2 Experimental section

7.2.1 Preparation of photocatalysts

The Bi-doped TiO_2 catalysts were prepared by a modified photochemical route (Liu et al. 2016). Typically, P25 powder (TiO_2, 200 mg) were dispersed in deionized water for ultrasound treatment of 5 min to obtain a highly dispersed suspension. $Bi(NO_3)_3$ was firstly dissolved in HNO_3 solution (0.85 M). Then $Bi(NO_3)_3$ solution (4 mM) was added into the TiO_2 dispersion under stirring (weight ratio TiO_2/Bi = 135:1 (N-Bi), total volume = 150 mL). After sonicating for another 5 min, the mixture was kept stirring at 600 rpm with a magnetic stirrer under UV treatment of a Xenon-lamp parallel light source system (CEL-S500, Beijing Ceaulight Co., Ltd. China) with the power density was about 100 mW cm^{-2}. After 10-min irradiation, the obtained products were collected via centrifugation and washed with deionized water for several times. Finally, the prepared catalysts can be obtained after drying in a vacuum oven. By varying the concentration of $Bi(NO_3)_3$ solution, the weight ratios of $Bi(NO_3)_3$:TiO_2 were settled as 135:10 (N-10Bi) and 135:20 (N-20Bi). The catalysts adopted $Bi(NO_3)_3$ as the precursor were totally denoted as N-Bi/TiO_2. When $BiCl_3$ was used as the Bi precursor, $BiCl_3$ was firstly dissolved in HCl solution (0.85 M). The weight ratio of $BiCl_3$:TiO_2 were also 1:135 (Cl-1Bi), 10:135 (Cl-10Bi) and 20:135 (Cl-20Bi). The obtained catalysts prepared from $BiCl_3$ were totally denoted as Cl-Bi/TiO_2. As for other metal-modified TiO_2 (e.g., Pt, Fe), the synthesis method is the same as the procedure of preparation of Cl-Bi/TiO_2 by replacing Bi with the corresponding metal precursors.

7.2.2 Characterization of as-prepared photocatalysts

X-ray diffraction (XRD) results were collected from 10° to 80° (Bruker D8 Advance). The UV-Vis absorption spectra of as-prepared photocatalysts were measured on a 950 UV/Vis-NIR spectrophotometer (Perkin Elmer Lambda). X-ray photoelectron spectroscopy (XPS, ESCALab 250Xi, Thermo Fisher) was conducted with C as the internal standard (C1s = 284.8 eV). High angle annular dark field (HAADF)-scanning transmission electron microscopy (STEM) images (Themis Z, Thermo scientific) were collected to observe the morphologies of as-prepared photocatalysts. The x-ray absorption near-edge structure (XANES spectra) (C K-edge and N K-edge) were measured at beamline BL12B of National Synchrotron Radiation Laboratory (NSRL) of China. The samples were deposited onto double-sided carbon tape for analysis on the X-ray spectroscopy. Extended x-ray absorption fine structure (EXAFS) measurement and data analysis: EXAFS spectra at the Bi L-edge were collected at BL14W1 station in Shanghai Synchrotron Radiation Facility (SSRF). The Bi L-edge XANES data were recorded in a fluorescence mode. Diffuse reflectance infrared Fourier transform spectroscopy (DRIFTS) was recorded on a Shimadzu Tracer-100 FTIR spectrometer equipped with a high-sensitivity mercury cadmium telluride (MCT) detector. The method for recording in-situ DRIFTS spectra of PFOA decomposition has been described in our previous study (Liu et al. 2021b).

7.2.3 Photocatalytic degradation of PFOA

The reactor and reaction conditions were the same as our previous work (Liu et al. 2021b). 20 mg of the as-prepared photocatalyst was firstly mixed with PFOA solution (100 mL, 10 mg L^{-1}) by sonication. The light sources used were a 254 nm UV light (30 W) and a Xenon lamp (300 W). The Xenon lamp used mainly emits light spectrum in the range of 300-1100 nm. The samples were taken out at regular time intervals and filtered for further analysis. Then, the filtered samples were detected for the concentrations of PFOA and the degradation intermediates. The concentrations of fluoride ion were also quantified to calculate the defluorination ratio. The photocatalytic experiments were carried out in triplicates and presented with mean values and standard deviations.

7.2.4 Analysis of PFOA and its decomposition intermediates

PFOA and the degradation intermediates were quantified using high-performance liquid chromatography-tandem mass spectrometry (HPLC-MS/MS, Agilent). The method was the same as detailed in our previous study (Liu et al. 2021b).

7.3 Results and discussion

7.3.1 Characterization of Bi/TiO$_2$.

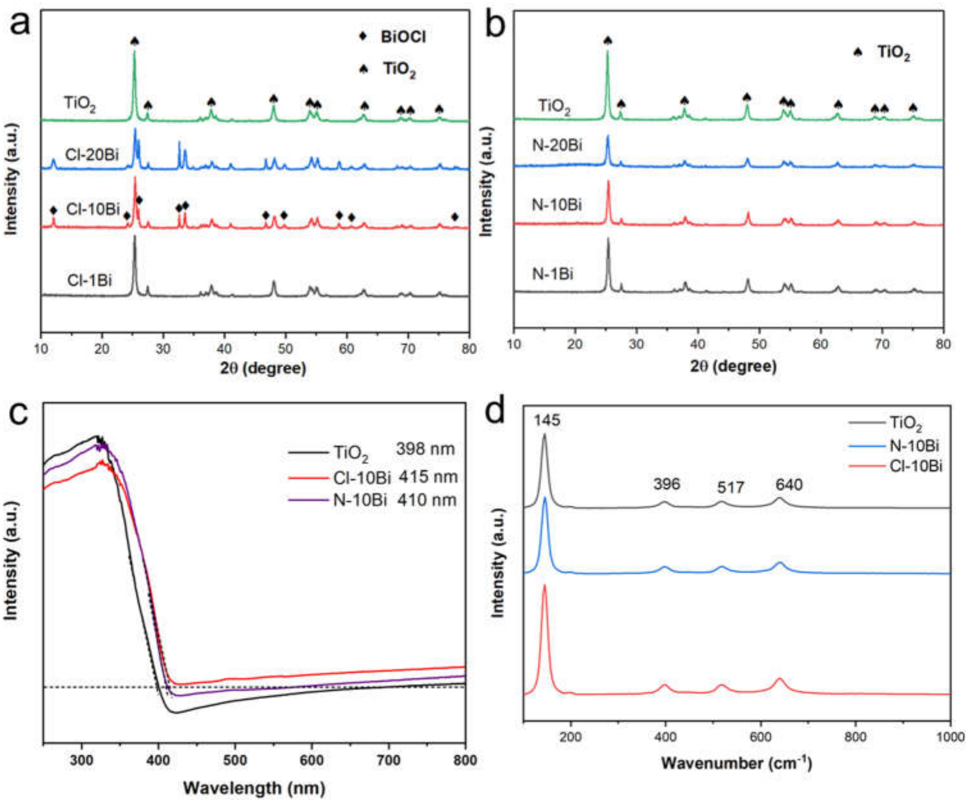

Figure 7. 1 The XRD data of Cl-Bi/TiO$_2$ (a); and N-Bi/TiO$_2$ photocatalysts; Uv-vis absorption spectra (c) and Raman spectra (d) of TiO$_2$, N-10Bi, Cl-10Bi.

XRD, XPS and XAFS characterizations were carried out to investigate the structures, surface composition and chemical states of Cl-Bi/TiO$_2$ and N-Bi/TiO$_2$. The XRD results indicate that when the ratio of BiCl$_3$:TiO$_2$ is 1:135, only the diffraction patterns of TiO$_2$ is observed (Fig. 7.1a). While, with the increased ratio to 10:135 and 20:135, the diffraction patterns of BiOCl appear, implying the formation of BiOCl under UV irradiation. When $Bi(NO_3)_3$ was used as the precursor, no BiOCl signal is observed (Fig. 7.1a). The characteristic diffraction peaks of hexagonal-close-packed (hcp) Bi were not detected in N-Bi/TiO_2. Similar results were reported in the previous reports that single Bi atoms on N-doped carbon networks (Bi SAs/NC) and Bi clusters on N-doped carbon networks (Bi Cs/NC) were generated (Zhang et al. 2019b) (Yang et al. 2020a). UV-vis absorption spectra of Bi/TiO_2 are recorded to investigate their absorption capacity (Fig. 7.1c). After the deposition of Bi on the surface of TiO_2, there are slight increase of the absorption for UV and visible light. The absorption edge of N-10Bi, Cl-10Bi and TiO_2 situated at 410, 413 and 398 nm. The band gap values of these semiconductor photocatalysts can be calculated based on the formula $E_g = 1240/\lambda_g$, where λ_g is the band gap wavelength (Xue et al. 2017). Accordingly, the estimated band gaps for N-10Bi, Cl-10Bi and TiO_2, are 3.02, 3.00, and 3.12 eV. In the Raman spectra, the bands at 145, 396, 517 and 640 cm^{-1} were attributed to the characteristic peaks of TiO_2 (Wen et al. 2018). XRD and Raman spectra suggest that Bi doping did not destroy the crystal structure of TiO_2 (Fig. 7.1d).

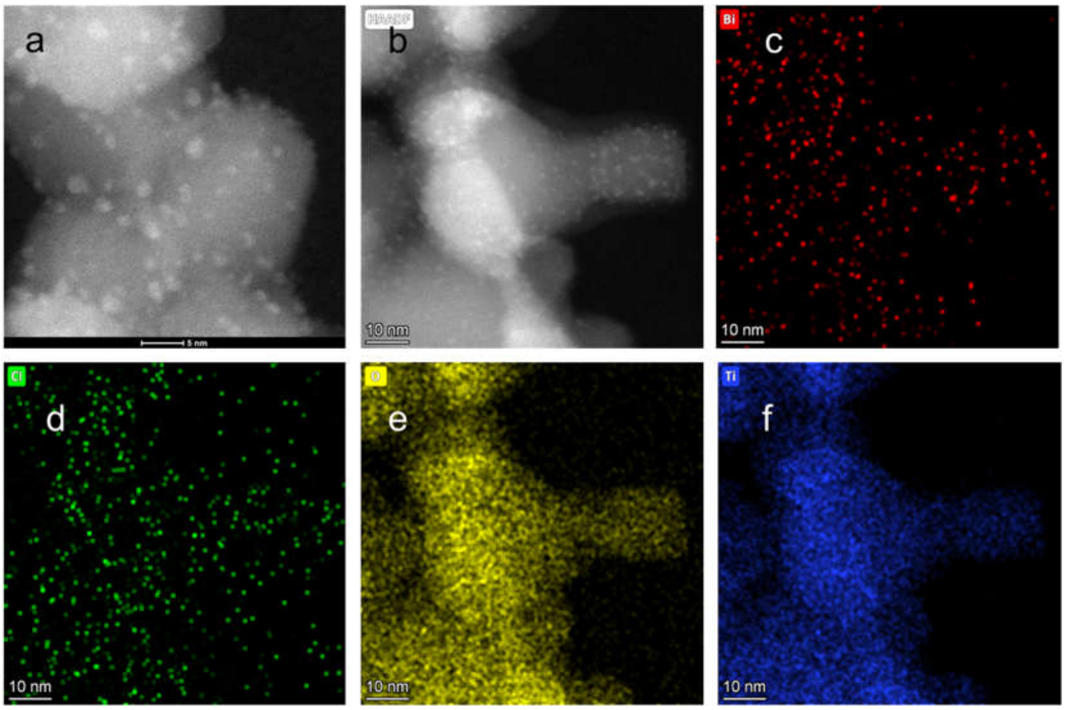

Figure 7. 2 The STEM image of Cl-10Bi (a, b) and its corresponding mapping spectra for the Bi (c), Cl (d), O (e) and Ti (f) elements.

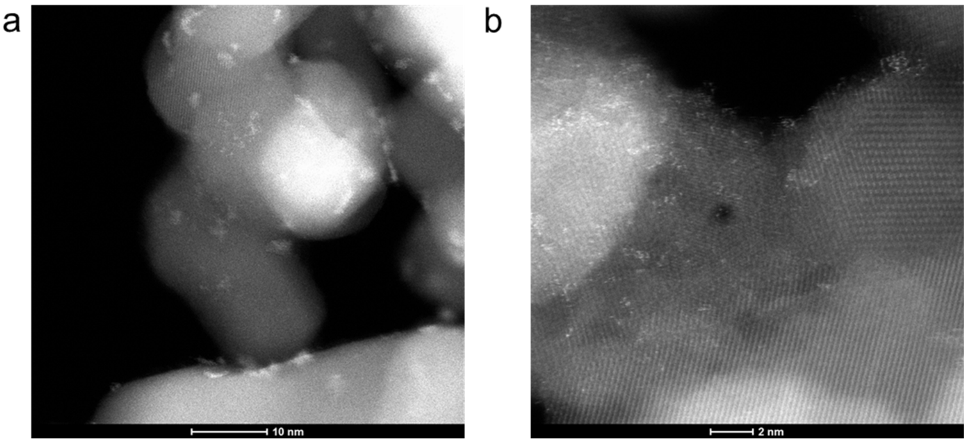

Figure 7. 3 The STEM images of N-10Bi at different magnifications (a, b).

STEM images depicted a cluster morphology of BiOCl with the size of ~2 nm on the surface of TiO_2 (Fig. 7.2 and Fig. 7.4a). The mapping results indicated that Bi, Cl, O and Ti elements were distributed evenly on the surface (Fig. 7.2a-f), which may be due to the formation of BiOCl on the surface of TiO_2, which was consistent with the XRD results. The STEM image of N-10Bi (Fig. 7.3a-b) revealed the cluster morphology with a size of ~ 2 nm. When the image is further magnified, Bi single atoms can be observed on the surface of TiO_2. Figure 7.4b displayed the dispersion of Bi single atoms on the surface of TiO_2. When adopting $Bi(NO_3)_3$ as the precursor, light spot sites on the surface of TiO_2 indicate that single Bi atoms are generated and dispersed on the surface of TiO_2. The intimate contact between Bi and TiO_2 is favourable for the charge transfer between Bi and TiO_2. XPS spectra were conducted to investigate the chemical composition and valance state of the surface elements. As shown in Fig. 7.4c, the Bi 4f peaks located at 164.9 and 159.6 eV could be attributed to Bi^{3+} in Cl-Bi/TiO_2 (Hu et al. 2014). Except the peaks of Bi^{3+}, two more peaks situated at 157.5 eV and 162.8 eV were found, which could be ascribed to the generation of Bi^0 in N-Bi/TiO_2 (Fig. 7.4d). These results indicated that both Bi^0 and Bi^{3+} existed in N-Bi/TiO_2 (Li et al. 2020d, Morgan et al. 1973). XPS results also show that, with a further increase of Bi content, the content of incorporated Bi only slightly increased, indicating that a small content of Bi precursor was enough for the deposition of Bi on TiO_2, and the substrate cannot host an ultrahigh Bi loading.

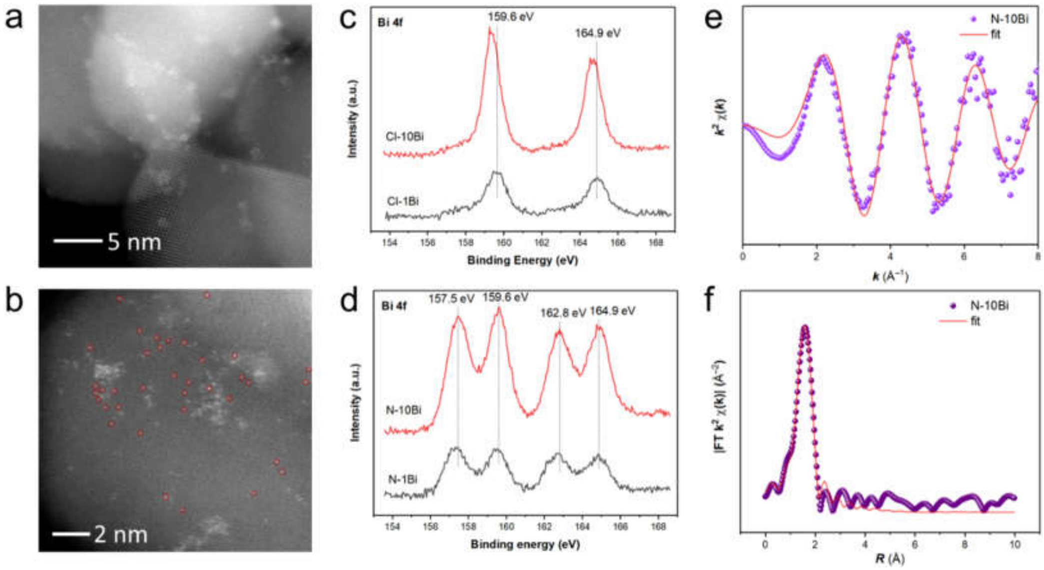

Figure 7.4 The STEM image of Cl-10Bi (a) and N-10Bi (b); XPS spectra of Bi 4f of Cl-10Bi (c) and N-10Bi (d); Fourier-transformed magnitudes of Bi K-edge EXAFS fitting in K space (e) and R space (f) for N-10Bi.

To further disclose the coordination environment of single Bi atoms, X-ray absorption near-edge structure and extended X-ray absorption fine structure (EXAFS) spectroscopy are performed (Fig. 7.4e and 7.4f) (Zhang et al. 2020). The EXAFS spectrum of R space for N-10Bi/TiO$_2$ exhibited a dominant Bi-O coordination at 1.56 Å (Fig. 7.4f), indicating that isolated Bi atoms were dispersed on the support. The absence of Bi-Bi coordination for N-Bi/TiO$_2$ further revealed the fine dispersion of isolated Bi atoms, instead of clusters or nanoparticles.

7.3.2 The efficient photocatalytic defluorination of PFOA by Bi/TiO$_2$

Pure TiO$_2$ demonstrated poor activity for the photocatalytic decomposition and defluorination of PFOA, only ~15% of PFOA was degraded with a low defluorination ratio of 2% (Fig. 7.5a and 7.5b). The incorporation of Fe showed little enhancement on the activity for the photocatalytic defluorination performance of TiO$_2$. Pd-doping enhanced the defluorination ratio of PFOA to ~10% because of the accelerated charge-transfer of Pd/TiO$_2$ (Huang et al. 2013, Yilmaz et al. 2017). In contrast, the incorporation of Bi SAs significantly promoted the photocatalytic activity of TiO$_2$ achieving defluorination efficiency of more than 60%. These results indicate that Bi SAs has great potential as the cocatalyst of TiO$_2$ to improve the photocatalytic performance.

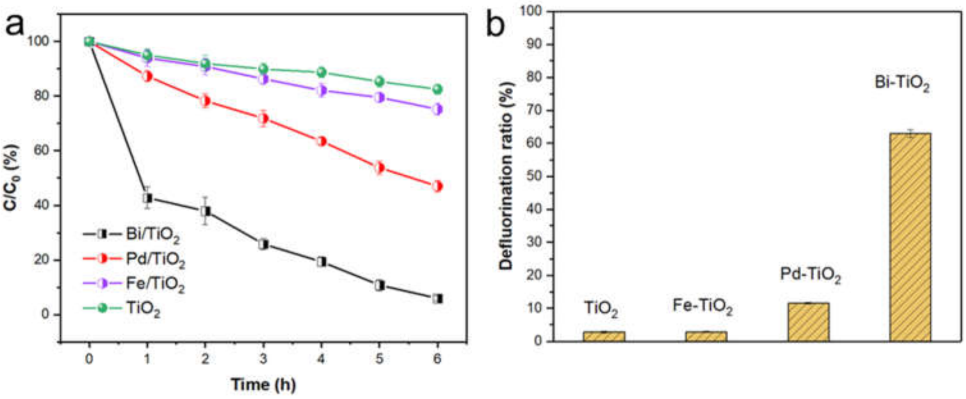

Figure 7.5 The degradation (a) and defluorination (b) of PFOA over various metal-modified TiO_2 (weight ratio (TiO_2: metal= 135:1)) photocatalysts. Reaction conditions: (Catalyst dosage: 20 mg L^{-1}; Initial PFOA concentration: 10 mg L^{-1}; UV 254 nm irradiation).

Both N-Bi/TiO_2 and Cl-Bi/TiO_2 demonstrate high efficiency for the defluorination of PFOA under UV light irradiation (Fig. 7.6). Cl-1Bi shows good efficiency for the photocatalytic defluorination of PFOA with a defluorination of 60%. With the increase of the Bi content, a higher defluorination ratio of 70% is obtained with Cl-10Bi and Cl-20Bi as the photocatalysts (Fig. 7.6a). For N-Bi/TiO_2, the photocatalytic efficiency increased with the increase of the Bi amount. The defluorination ratio of PFOA increased from 55% to 70% for N-1Bi to N-20Bi (Fig. 7.6b).

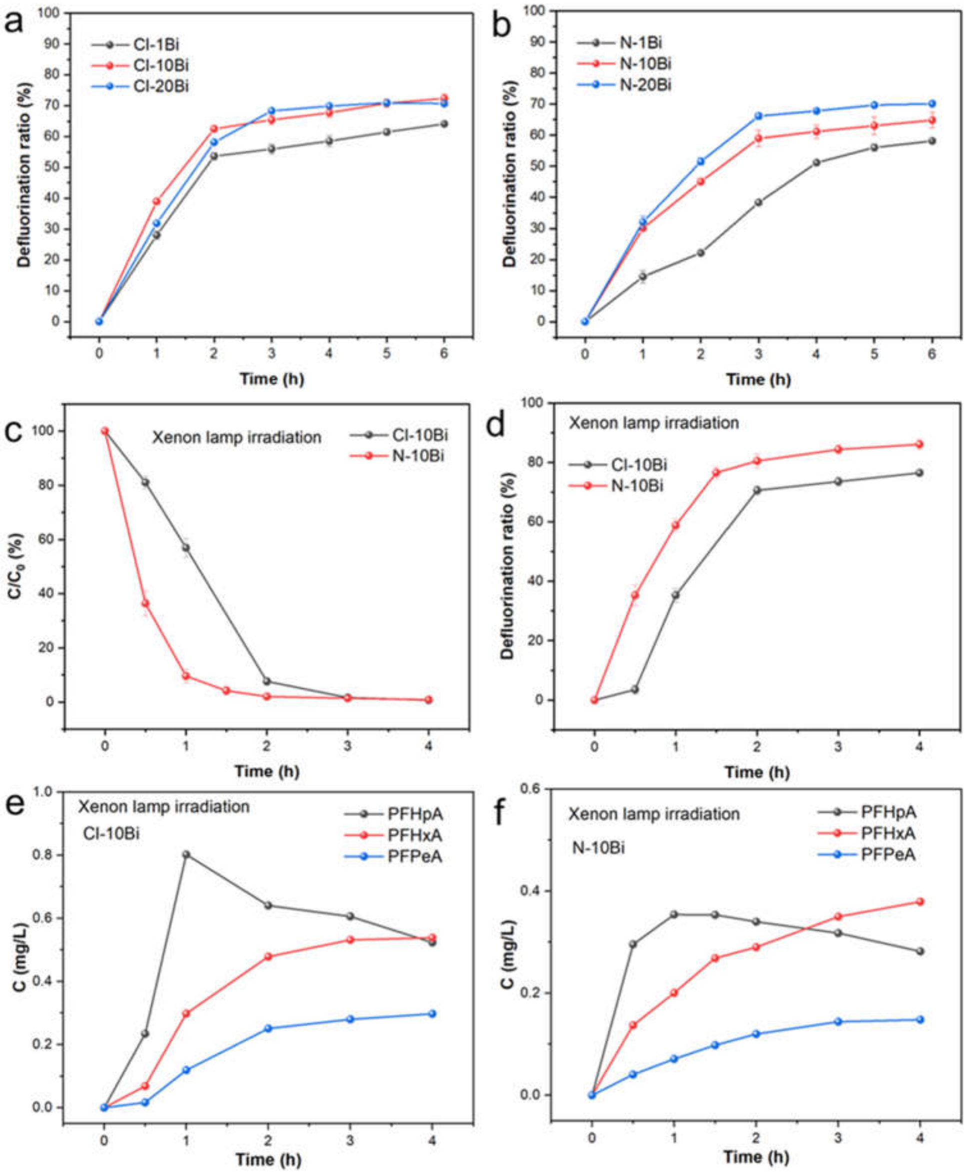

Figure 7.6 The photocatalytic defluorination ratio of PFOA over Cl-Bi/TiO_2 (a) and N-Bi/TiO_2 (b) catalysts. Reaction conditions: (Catalyst dosage: 20 mg L^{-1}; Initial PFOA concentration: 10 mg L^{-1}; UV 254 nm irradiation); The photocatalytic decomposition (c) and defluorination (d) of PFOA over Cl-10Bi and N-10Bi under Xenon lamp irradiation, the other conditions were the same with those reactions in a and b; The detected intermediates during the decomposition of PFOA over Cl-10Bi (e) and N-10Bi (f).

When irradiated under Xenon lamp irradiation, the photocatalytic defluorination of N-10Bi exhibited better performance. PFOA could be completely removed within 2 h and a deep defluorination ratio of 85% was obtained after irradiation for 4 h. The high defluorination ratio obtained were superior to almost all the photocatalysts reported(Liu et al. 2020). When Cl-10Bi was used as the photocatalyst, a defluorination ratio of 76% was obtained after irradiation by Xenon lamp for 4 h. The higher photocatalytic activity of N-10Bi under Xenon lamp irradiation than Cl-10Bi indicated that N-10Bi had better light utilization efficiency of the full spectrum (Fig. 7.6c and 7.6d). Moreover, the decomposition intermediates of PFOA were detected during the irradiation period (Fig. 7.6e and 7.6f). The degradation of PFOA followed a stepwise way, the same as most previously reported studies (Liu et al. 2021c, Qian et al. 2020, Shao et al. 2013a). The concentration of perfluoroheptanoic acid ($C_6F_{13}COOH$, PFHpA) increased firstly in the first one hour and decreased afterwards. Then, the concentrations of PFHpAperfluorohexanoic acid ($C_5F_{11}COOH$, PFHxA) and perfluoropentanoic acid (C_4F_9COOH, PFPeA) increased subsequently.

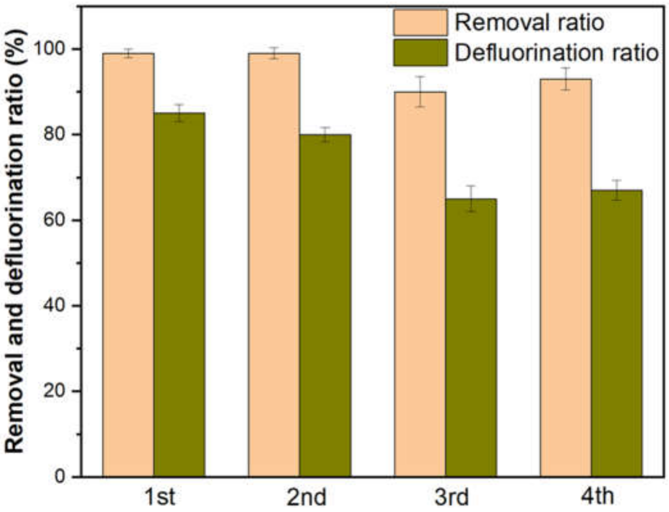

Figure 7. 7 The cycle use of N-10Bi for the photocatalytic defluorination under Xenon lamp irradiation.

Moreover, the stability of N-10Bi was also tested for four successive runs (Fig. 7.7). More than 90% of PFOA could be removed by N-10Bi with the defluorination ratio slightly decreased to 65%. These results indicate that N-10Bi exhibited good stability with great potential for practical applications.

7.3.3 The photocatalytic mechanism of PFOA

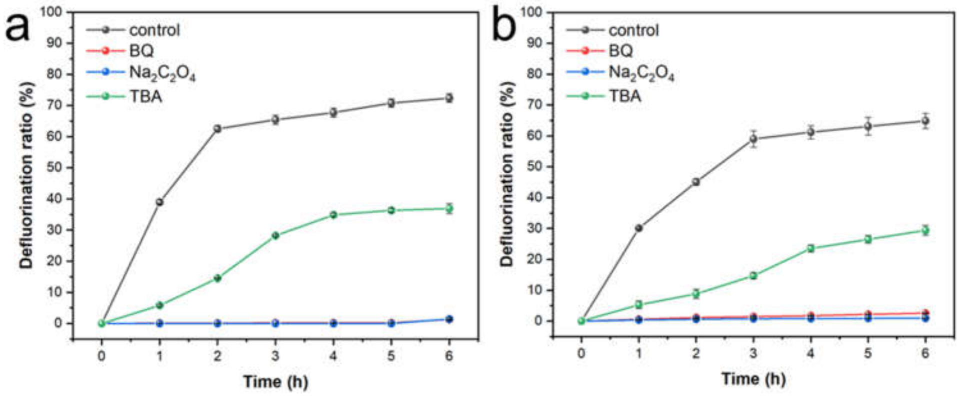

Figure 7. 8 The scavenging effects on the photocatalytic defluorination of PFOA over Cl-10Bi (a) and N-10Bi (b) under UV 254 nm irradiation.

Scavenging experiments are conducted to investigate the reactive oxygen species (ROS) that involved in the photodecomposition of PFOA (Fig. 7.8a and Fig. 7.8b). Sodium oxalate ($Na_2C_2O_4$, 2 mM), p-benzoquinone (p-BQ, 2 mM) and tertbutyl alcohol (TBA, 52.4 mM) are applied to selectively quench photo-induced holes, superoxide radical ($O_2^{\bullet-}$) and $^{\bullet}$OH, respectively. The results show that the decomposition of PFOA could be completely inhibited by $Na_2C_2O_4$ and P-BQ both in N-Bi/TiO_2 and Cl-Bi/TiO_2 systems. These phenomena indicate that photo-induced holes and $O_2^{\bullet-}$ are the crucial active species responsible for the degradation of PFOA. Different from the reported results, where $O_2^{\bullet-}$ contributed little to the photocatalytic degradation of PFOA (Li et al. 2020b). The scavenging experiment results also indicated that PFOA degraded in an oxidative way, where the decarboxylation initiated the degradation, followed by the removal of CF_2 group stepwise. This is quite different from the report that Pt_1 on TiO_2 degrade PFOA via a reductive pathway (Weon et al. 2021). The reason maybe the high valance band position of Bi/TiO2 photocatalysts (2.95-3.15 eV, Fig. 7.9).

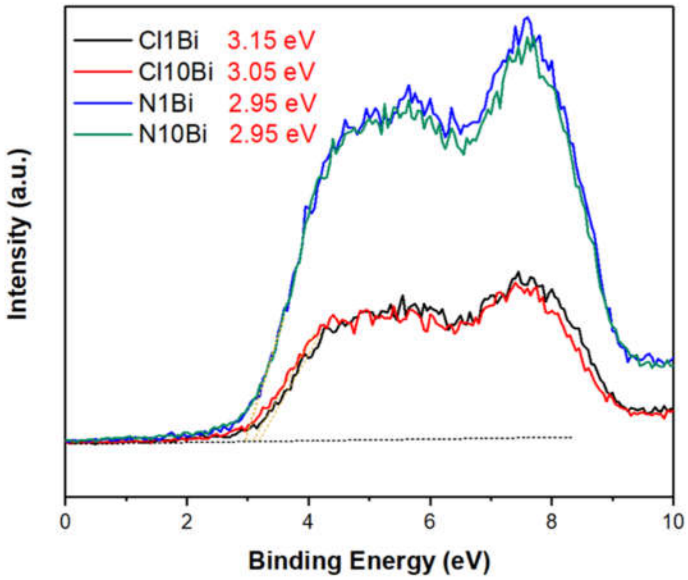

Figure 7. 9 Valance band XPS spectra of Bi/TiO_2 photocatalysts.

The adsorption of PFOA on the prepared photocatalysts were investigated by the DRIFTS spectra (Fig. 7.10a). The peaks at 1672 and 1418 cm^{-1} of PFOA adsorbed on TiO_2 were attributed to the asymmetric and symmetric stretching modes of –COOH group. Upon adsorption on Cl-10Bi and N-10Bi, the peaks of –COO group appeared at 1634 and 1418 cm^{-1}. The smaller Δv value ($\Delta v = v_{as}$ (COO^{-}) - v_s (COO^{-})) for PFOA adsorbed on the surface of Cl-10Bi and N-10Bi, was due to the formation of bidentate coordination between PFOA and Cl-10Bi/N-10Bi. Moreover, we can see that when PFOA was adsorbed on N-10Bi. The C-F bond shifted to lower wavenumbers, compared with that adsorbed on TiO_2 or Cl-10Bi. The shift of C-F bond to lower wavenumbers was due to the ionization of C-F bond (Li et al. 2004, Wang et al. 2012), which was probably induced by the Bi single atoms.

Moreover, in-situ DRIFTS spectra of photocatalytic degradation of PFOA over Cl-10Bi or N-10Bi were recorded to explore the decomposition processes. When Cl-10Bi was used as the catalyst (Fig. 7.10b), the peaks at 1207 cm^{-1}, 1240 cm^{-1} and 1260 cm^{-1} were assigned to C–F bonds. The peak at 1020 cm^{-1} was attributed to the stretching of C–C bond (Liu et al. 2021b). The reversed peaks were due to the consumption of –COOH group, C–F and C–C bonds, further verifying that the –COOH and C–F groups were attacked during the degradation. When PFOA was degraded over N-10Bi (Fig. 7.10c), the vibration of C-F mainly located at 1166 cm^{-1}. The possible reasons were that Bi single atoms deposited on TiO_2 caused the ionization of C-F bond (Li et al. 2004, Palchan et al. 1989), further leading to the defluorination of PFOA.

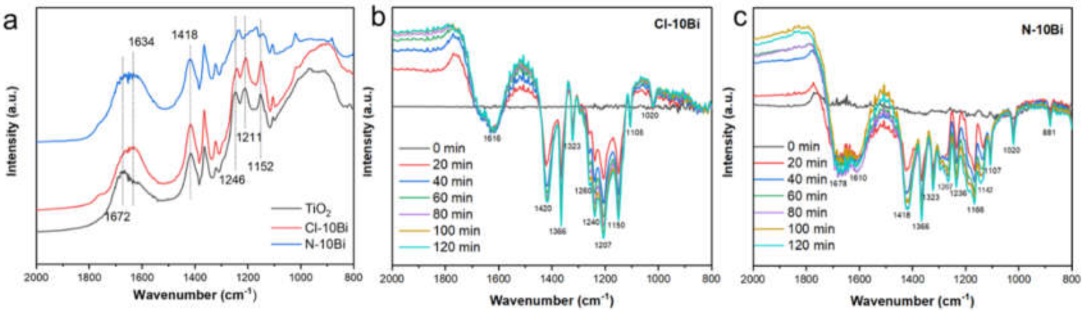

Figure 7.10 DRIFTS spectra of PFOA adsorbed on TiO_2, Cl-10Bi and N-10Bi (a); In-situ DRIFTS spectra of PFOA decomposition over Cl-10Bi (b) and N-10Bi (c).

7.4 Conclusion

In this study, we firstly reported the synthesis of Bi SAs/TiO_2 composite under UV irradiation at room temperature. Bi SAs were generated on the surface of TiO_2 when adopting $Bi(NO_3)_3$ as the precursor. While, BiOCl nanoclusters were formed over TiO_2, when $BiCl_3$ was used as the Bi source. Both N-Bi/TiO_2 Cl-Bi/TiO_2 demonstrated outstanding performance for the photocatalytic degradation and defluorination of PFOA under UV 254 nm irradiation and Xenon lamp irradiation. Further studies indicate that photo-induced holes and $O_2^{\bullet-}$ are responsible for the decarboxylation process, which initiated the decomposition of PFOA. Moreover, the as-prepared N-Bi/TiO_2 show good stability in multiple runs. In addition, in-situ DRIFTS spectra demonstrated that the Bi single atoms in N-Bi/TiO_2 induced the ionization of C-F bond of PFOA, leading to the deep defluorination of PFOA. This study provides a novel way for the preparation of Bi SAs and BiOCl at room temperature without using organic solvents.

CHAPTER 8

Conclusions and perspectives

8.1 Conclusions

Efficient semiconductor photocatalysts have been developed in this study for the deep defluorination of PFOA. This study firstly used metal-organic-frameworks (MOFs) derived In_2O_3 for the photocatalytic degradation of PFOA. MOFs derived In_2O_3 demonstrated significantly enhanced performance for PFOA decomposition than commercial In_2O_3. The hydrophilicity of MOFs derived In_2O_3 is much better than commercial In_2O_3 which enables a better dispersion in the PFOA solution. The uniform dispersion of the photocatalysts is beneficial to the photocatalytic evolution of reactive oxygen species and degradation of PFOA. Overall, the present study helps to broaden the overview of purposely developing efficient photocatalysts to remediate PFOA.

In_2O_3 photocatalysts were prepared at 300, 400, 500 and 600°C. The results In_2O_3-300 and In_2O_3-400 demonstrated the best performance for the decomposition and defluorination of PFOA due to rich oxygen vacancy reserved, with the defluorination ratio of 35% and 38%. Further increasing the calcination temperature, the activity of In_2O_3 deteriorated and a defluorination ratio of less than 20% was obtained for In_2O_3-600. While, when Fe^{3+} was added, the defluorination ratio significantly increased to 60%. But, Fe^{3+} has little effect on the defluorination ratio of PFOA over In_2O_3-400. Combined with diffuse reflectance infrared Fourier transform spectroscopy (DRIFTS) and in-situ DRIFTS tracking the decomposition process of PFOA, the mechanisms for Fe^{3+} promoting the defluorination of PFOA over oxygen-vacancy-deficient In_2O_3-600 was proposed.

BiOX (X = Cl, Br and I) and BiOX/TiO_2 photocatalysts were prepared by a facile hydrothermal approach. The BiOX/TiO_2 heterojunctions demonstrated significantly enhanced performance for photocatalytic degradation of PFOA compared with sole BiOX or TiO_2. PFOA of 10 mg L^{-1} could be completely decomposed by BiOCl(Br)/TiO_2, and ~90% of PFOA could be removed by BiOI/TiO_2. While, under the same conditions, only 20%, 50%, 37% and 48% of PFOA was degraded by TiO_2, BiOCl, BiOBr, and BiOI, respectively. Moreover, BiOCl/TiO_2 attained deep decomposition of PFOA with a high defluorination ratio of 82 % under UV 254 nm illumination for 8 h. BiOCl/TiO_2 presented excellent performance for decomposing PFOA under Xenon lamp irradiation with a defluorination ratio of 73%. The p-n heterojunctions between BiOX and TiO_2 were confirmed by a series of characterizations. The photo-induced holes would migrate from the valance band (VB) of TiO_2 to BiOX, driven by the built-in electric field (BIEF) near the interfaces of p-n heterojunctions, the inner electric fields (IEF) in BiOX and the higher VB position of BiOX. The X-ray diffraction (XRD) and TEM characterizations indicated that TiO_2 combined with BiOX along the [110] facet, which facilitated photo-induced electron transfer in the [001] direction, thus benefiting PFOA decomposition.

Bi SAs deposited on TiO_2 were firstly prepared by irradiation and demonstrated ultra-high performance for the photocatalytic defluorination of PFOA. A deep defluorination of PFOA with a defluorination ratio of 85% was obtained after irradiation for 4 h. Various characterizations confirmed the generation of Bi SAs on the surface of TiO_2. DRIFTS and in-situ DRIFTS spectra indicated that Bi SAs induced the ionization of C-F bond, thus leading to the deep defluorination of PFOA.

8.2 Perspectives

Despite great efforts devoted to the treatment of PFCs, there are still many problems needed to be dissolved. Firstly, the advanced treatment of PFCs degradation products has yet been reported until now. Secondary pollution induced by the PFOA degradation, including the produced fluoride ions, degradation intermediates remains to be a great challenge for wastewater treatment.

Secondly, visible-light-responsive photocatalysts are required for efficient degradation and defluorination of PFCs. Developing noble metal-free photocatalysts with high activity, good stability and recoverability is essential for the treatment of practical PFCs-containing wastewaters. Moreover, recent studies for heterogeneous photocatalytic degradation of PFCs only focused on PFOA. However, PFCs are a diverse class of compounds with different structures. Therefore, more research is desired for the treatment of different kinds of PFCs.

Thirdly, most of the reported studies are about synthetic wastewater, which contain much higher concentration (mg L^{-1}) of PFCs than those in real contaminated water (ng L^{-1} - μg L^{-1}). And the constituents of real wastewater are much more complex than that of synthetic wastewater. The interfering factors (e.g., dissolved oxygen, pH, NOMs, NO_3^-, Cl^-, etc.) could significantly influence the PFCs removal. Thus, both homogenous and heterogeneous photocatalytic processes should be applied for the remediation of PFCs in real wastewater.

Lastly, Continuous-flow reactors are required to treat the PFCs-contained wastewater. We need to explore how to effectively deposit the photocatalysts on the continuous-flow rectors to further treat the real wastewater. Moreover, the photocatalytic processes can be combined with other treatment techniques to achieve synergistically effect for the efficient treatment of PFCs-contained wastewater.

REFERENCES

Adamek, E., Baran, W. and Sobczak, A. (2015) Effect of $FeCl_3$ on the photocatalytic processes initiated by UVa and vis light in the presence of TiO_2–P25. Applied Catalysis B: Environmental 172-173, 136-144.

Ai, Z., Ho, W., Lee, S. and Zhang, L. (2009) Efficient Photocatalytic Removal of NO in Indoor Air with Hierarchical Bismuth Oxybromide Nanoplate Microspheres under Visible Light. Environmental Science & Technology 43(11), 4143-4150.

Akhavan, O. and Ghaderi, E. (2009) Photocatalytic Reduction of Graphene Oxide Nanosheets on TiO_2 Thin Film for Photoinactivation of Bacteria in Solar Light Irradiation. The Journal of Physical Chemistry C 113(47), 20214-20220.

Baduel, C., Paxman, C.J. and Mueller, J.F. (2015) Perfluoroalkyl substances in a firefighting training ground (FTG), distribution and potential future release. Journal of hazardous materials 296, 46-53.

Benskin, J.P., Yeung, L.W.Y., Yamashita, N., Taniyasu, S., Lam, P.K.S. and Martin, J.W. (2010) Perfluorinated Acid Isomer Profiling in Water and Quantitative Assessment of Manufacturing Source. Environmental Science & Technology 44(23), 9049-9054.

Bhui, D.K., Bar, H., Sarkar, P., Sahoo, G.P., De, S.P. and Misra, A. (2009) Synthesis and UV–vis spectroscopic study of silver nanoparticles in aqueous SDS solution. Journal of Molecular Liquids 145(1), 33-37.

Brandsma, S., Koekkoek, J., van Velzen, M. and de Boer, J. (2019) The PFOA substitute GenX detected in the environment near a fluoropolymer manufacturing plant in the Netherlands. Chemosphere 220, 493-500.

Butenhoff, J.L., Chang, S.-C., Olsen, G.W. and Thomford, P.J. (2012) Chronic dietary toxicity and carcinogenicity study with potassium perfluorooctanesulfonate in Sprague Dawley rats. Toxicology 293(1-3), 1-15.

Chandrasekaran, S., Yao, L., Deng, L., Bowen, C., Zhang, Y., Chen, S., Lin, Z., Peng, F. and Zhang, P. (2019) Recent advances in metal sulfides: from controlled fabrication to electrocatalytic, photocatalytic and photoelectrochemical water splitting and beyond. Chemical Society Reviews 48(15), 4178-4280.

Chen, C., Cai, W., Long, M., Zhou, B., Wu, Y., Wu, D. and Feng, Y. (2010) Synthesis of Visible-Light Responsive Graphene Oxide/TiO_2 Composites with p/n Heterojunction. ACS Nano 4(11), 6425-6432.

Chen, D., Hao, Q., Wang, Z., Ding, H. and Zhu, Y. (2016) Influence of phase structure and morphology on the photocatalytic activity of bismuth molybdates. CrystEngComm 18(11), 1976-1986.

Chen, F., Yang, Q., Li, X., Zeng, G., Wang, D., Niu, C., Zhao, J., An, H., Xie, T. and Deng, Y. (2017) Hierarchical assembly of graphene-bridged Ag_3PO_4/Ag/$BiVO_4$ (040) Z-scheme photocatalyst: An efficient, sustainable and heterogeneous catalyst with enhanced visible-light photoactivity towards tetracycline degradation under visible light irradiation. Applied Catalysis B: Environmental 200, 330-342.

Chen, J., Guan, M., Cai, W., Guo, J., Xiao, C. and Zhang, G. (2014) The dominant {001} facet-dependent enhanced visible-light photoactivity of ultrathin BiOBr nanosheets. Physical Chemistry Chemical Physics 16(38), 20909-20914.

Chen, L., Huang, R., Xiong, M., Yuan, Q., He, J., Jia, J., Yao, M.-Y., Luo, S.-L., Au, C.-T. and Yin, S.-F. (2013) Room-Temperature Synthesis of Flower-Like BiOX (X═Cl, Br, I) Hierarchical Structures and Their Visible-Light Photocatalytic Activity. Inorganic Chemistry 52(19), 11118-11125.

Chen, M.-J., Lo, S.-L., Lee, Y.-C. and Huang, C.-C. (2015) Photocatalytic decomposition of perfluorooctanoic acid by transition-metal modified titanium dioxide. Journal of hazardous materials 288, 168-175.

Chen, Y., Ji, S., Chen, C., Peng, Q., Wang, D. and Li, Y. (2018) Single-Atom Catalysts: Synthetic Strategies and Electrochemical Applications. Joule 2(7), 1242-1264.

Chen, Z., Liu, Y., Wei, W. and Ni, B.-J. (2019) Recent advances in electrocatalysts for halogenated organic pollutant degradation. Environmental Science: Nano 6(8), 2332-2366.

Cho, W., Lee, H.J. and Oh, M. (2008) Growth-controlled formation of porous coordination polymer particles. Journal of the American Chemical Society 130(50), 16943-16946.

Cho, W., Lee, Y.H., Lee, H.J. and Oh, M. (2009) Systematic transformation of coordination polymer particles to hollow and non-hollow In_2O_3 with pre-defined morphology. Chem Commun (Camb) (31), 4756-4758.

Choi, W., Termin, A. and Hoffmann, M.R. (1994) The Role of Metal Ion Dopants in Quantum-Sized TiO_2: Correlation between Photoreactivity and Charge Carrier Recombination Dynamics. The Journal of Physical Chemistry 98(51), 13669-13679.

Chu, C., Huang, D., Gupta, S., Weon, S., Niu, J., Stavitski, E., Muhich, C. and Kim, J.-H. (2021a) Neighboring Pd single atoms surpass isolated single atoms for selective hydrodehalogenation catalysis. Nature communications 12(1), 5179.

Chu, C., Huang, D., Gupta, S., Weon, S., Niu, J., Stavitski, E., Muhich, C. and Kim, J.-H. (2021b) Neighboring Pd single atoms surpass isolated single atoms for selective hydrodehalogenation catalysis. Nature Communications 12(1), 1-7.

Clément, J.-L., Ferré, N., Siri, D., Karoui, H., Rockenbauer, A. and Tordo, P. (2005) Assignment of the EPR spectrum of 5, 5-dimethyl-1-pyrroline N-oxide (DMPO) superoxide spin adduct. The Journal of organic chemistry 70(4), 1198-1203.

Colmenares, J.C. and Luque, R. (2014a) Heterogeneous photocatalytic nanomaterials: prospects and challenges in selective transformations of biomass-derived compounds. Chem Soc Rev 43(3), 765-778.

Colmenares, J.C. and Luque, R.J.C.S.R. (2014b) Heterogeneous photocatalytic nanomaterials: prospects and challenges in selective transformations of biomass-derived compounds. 43(3), 765-778.

Costanza, J., Arshadi, M., Abriola, L.M. and Pennell, K.D. (2019) Accumulation of PFOA and PFOS at the air–water interface. Environmental Science & Technology Letters 6(8), 487-491.

Cui, J., Gao, P. and Deng, Y. (2020) Destruction of Per- and Polyfluoroalkyl Substances (PFAS) with Advanced Reduction Processes (ARPs): A Critical Review. Environ Sci Technol 54(7), 3752-3766.

Cui, Q., Pan, Y., Zhang, H., Sheng, N., Wang, J., Guo, Y. and Dai, J. (2018) Occurrence and Tissue Distribution of Novel Perfluoroether Carboxylic and Sulfonic Acids and Legacy Per/Polyfluoroalkyl Substances in Black-Spotted Frog (Pelophylax nigromaculatus). Environmental Science & Technology 52(3), 982-990.

Daghrir, R., Drogui, P. and Robert, D. (2013) Modified TiO_2 for environmental photocatalytic applications: a review. Industrial & Engineering Chemistry Research 52(10), 3581-3599.

Deacon, G.B. and Phillips, R.J. (1980) Relationships between the carbon-oxygen stretching frequencies of carboxylato complexes and the type of carboxylate coordination. Coordination Chemistry Reviews 33(3), 227-250.

Dhakshinamoorthy, A., Li, Z. and Garcia, H. (2018) Catalysis and photocatalysis by metal organic frameworks. Chem Soc Rev 47(22), 8134-8172.

Dillert, R., Bahnemann, D. and Hidaka, H. (2007) Light-induced degradation of perfluorocarboxylic acids in the presence of titanium dioxide. Chemosphere 67(4), 785-792.

Dong, F., Zhao, Z., Sun, Y., Zhang, Y., Yan, S. and Wu, Z. (2015) An advanced semimetal–organic Bi spheres–g-C_3N_4 nanohybrid with SPR-enhanced visible-light photocatalytic performance for NO purification. Environmental Science & Technology 49(20), 12432-12440.

Duan, L., Wang, B., Heck, K., Guo, S., Clark, C.A., Arredondo, J., Wang, M., Senftle, T.P., Westerhoff, P., Wen, X., Song, Y. and Wong, M.S. (2020) Efficient Photocatalytic PFOA Degradation over Boron Nitride. Environmental Science & Technology Letters.

Duoerkun, G., Zhang, Y., Shi, Z., Shen, X., Cao, W., Liu, T., Liu, J., Chen, Q. and Zhang, L. (2020) Construction of n-TiO_2/p-Ag_2O Junction on Carbon Fiber Cloth with Vis–NIR Photoresponse as a Filter-Membrane-Shaped Photocatalyst. Advanced Fiber Materials 2(1), 13-23.

Egerton, T.A. and Tooley, I.R. (2004) Effect of Changes in TiO_2 Dispersion on Its Measured Photocatalytic Activity. The Journal of Physical Chemistry B 108(16), 5066-5072.

Ekström, G.N. and McQuillan, A.J. (1999) In Situ Infrared Spectroscopy of Glyoxylic Acid Adsorption and Photocatalysis on TiO_2 in Aqueous Solution. The Journal of Physical Chemistry B 103(48), 10562-10565.

Eriksen, K.T., Raaschou-Nielsen, O., Sørensen, M., Roursgaard, M., Loft, S. and Møller, P. (2010) Genotoxic potential of the perfluorinated chemicals PFOA, PFOS, PFBS, PFNA and PFHxA in human HepG2 cells. Mutation Research/Genetic Toxicology and Environmental Mutagenesis 700(1), 39-43.

Fan, J.C.C. and Goodenough, J.B. (1977) X-ray photoemission spectroscopy studies of Sn-doped indium-oxide films. Journal of Applied Physics 48(8), 3524-3531.

Fan, W., Li, H., Zhao, F., Xiao, X., Huang, Y., Ji, H. and Tong, Y. (2016) Boosting the photocatalytic performance of (001) BiOI: enhancing donor density and separation efficiency of photogenerated electrons and holes. Chemical Communications 52(30), 5316-5319.

Gan, J., Lu, X., Wu, J., Xie, S., Zhai, T., Yu, M., Zhang, Z., Mao, Y., Wang, S.C., Shen, Y. and Tong, Y. (2013) Oxygen vacancies promoting photoelectrochemical performance of In_2O_3 nanocubes. Sci Rep 3, 1021.

Gao, C., Low, J., Long, R., Kong, T., Zhu, J. and Xiong, Y. (2020) Heterogeneous single-atom photocatalysts: Fundamentals and applications. Chemical Reviews 120(21), 12175-12216.

Gao, G., Jiao, Y., Waclawik, E.R. and Du, A. (2016) Single Atom (Pd/Pt) Supported on Graphitic Carbon Nitride as an Efficient Photocatalyst for Visible-Light Reduction of Carbon Dioxide. Journal of the American Chemical Society 138(19), 6292-6297.

Gao, X. and Chorover, J. (2012) Adsorption of perfluorooctanoic acid and perfluorooctanesulfonic acid to iron oxide surfaces as studied by flow-through ATR-FTIR spectroscopy. Environmental Chemistry 9(2), 148-157.

Gao, X., Metge, D.W., Ray, C., Harvey, R.W. and Chorover, J. (2009) Surface Complexation of Carboxylate Adheres Cryptosporidium parvum Öocysts to the Hematite−Water Interface. Environmental Science & Technology 43(19), 7423-7429.

Gnayem, H. and Sasson, Y. (2013) Hierarchical nanostructured 3D flowerlike BiOCl x Br1–x semiconductors with exceptional visible light photocatalytic activity. ACS Catalysis 3(2), 186-191.

Goss, K.-U. (2008) The p K a Values of PFOA and Other Highly Fluorinated Carboxylic

Acids. Environmental Science & Technology 42(2), 456-458.

Grabowska, E., Reszczyńska, J. and Zaleska, A. (2012) RETRACTED: Mechanism of phenol photodegradation in the presence of pure and modified-TiO_2: a review. Water Research 46(17), 5453-5471.

Gu, C., Wang, Z., Kubicki, J.D., Wang, X. and Zhu, M. (2016a) X-ray Absorption Spectroscopic Quantification and Speciation Modeling of Sulfate Adsorption on Ferrihydrite Surfaces. Environmental science & technology 50(15), 8067-8076.

Gu, Y., Dong, W., Luo, C. and Liu, T. (2016b) Efficient Reductive Decomposition of Perfluorooctanesulfonate in a High Photon Flux UV/Sulfite System. Environ Sci Technol 50(19), 10554-10561.

Guan, M., Xiao, C., Zhang, J., Fan, S., An, R., Cheng, Q., Xie, J., Zhou, M., Ye, B. and Xie, Y. (2013) Vacancy Associates Promoting Solar-Driven Photocatalytic Activity of Ultrathin Bismuth Oxychloride Nanosheets. Journal of the American Chemical Society 135(28), 10411-10417.

Guo, L., Xiao, Y., Xu, Z., Lin, S.-Y., Wang, H., Chu, X., Gao, X., Zhou, L., Chi, Y. and Yang, X. (2018) Band alignment of BiOCl/ZnO core shell nanosheets by X-ray photoelectron spectroscopy measurements. Ferroelectrics 531(1), 31-37.

Hao, D., Liu, C., Xu, X., Kianinia, M., Aharonovich, I., Bai, X., Liu, X., Chen, Z., Wei, W., Jia, G. and Ni, B.-J. (2020) Surface defect-abundant one-dimensional graphitic carbon nitride nanorods boost photocatalytic nitrogen fixation. New Journal of Chemistry 44(47), 20651-20658.

Hao, S., Choi, Y.-J., Wu, B., Higgins, C.P., Deeb, R. and Strathmann, T.J. (2021) Hydrothermal Alkaline Treatment for Destruction of Per- and Polyfluoroalkyl Substances in Aqueous Film-Forming Foam. Environmental Science & Technology 55(5), 3283-3295.

He, R., Xu, D., Cheng, B., Yu, J. and Ho, W. (2018) Review on nanoscale Bi-based photocatalysts. Nanoscale Horizons 3(5), 464-504.

He, Y., Zhang, L., Teng, B. and Fan, M. (2014) New application of Z-scheme Ag3PO4/g-C3N4 composite in converting CO2 to fuel. Environmental science & technology 49(1), 649-656.

Herrmann, J.-M. (1999) Heterogeneous photocatalysis: fundamentals and applications to the removal of various types of aqueous pollutants. Catalysis Today 53(1), 115-129.

Heydebreck, F., Tang, J., Xie, Z. and Ebinghaus, R. (2016) Emissions of Per- and Polyfluoroalkyl Substances in a Textile Manufacturing Plant in China and Their Relevance for Workers' Exposure. Environmental science & technology 50(19), 10386-10396.

Hoffmann, M.R., Martin, S.T., Choi, W. and Bahnemann, D.W. (1995) Environmental Applications of Semiconductor Photocatalysis. Chemical reviews 95(1), 69-96.

Hori, H., Nagaoka, Y., Yamamoto, A., Sano, T., Yamashita, N., Taniyasu, S., Kutsuna, S., Osaka, I. and Arakawa, R. (2006) Efficient Decomposition of Environmentally Persistent Perfluorooctanesulfonate and Related Fluorochemicals Using Zerovalent Iron in Subcritical Water. Environmental Science & Technology 40(3), 1049-1054.

Hori, H., Takano, Y., Koike, K., Takeuchi, K. and Einaga, H. (2003) Decomposition of environmentally persistent trifluoroacetic acid to fluoride ions by a homogeneous photocatalyst in water. Environmental science & technology 37(2), 418-422.

Hori, H., Yamamoto, A., Koike, K., Kutsuna, S., Murayama, M., Yoshimoto, A. and Arakawa, R. (2008) Photocatalytic decomposition of a perfluoroether carboxylic acid by tungstic heteropolyacids in water. Applied Catalysis B: Environmental

82(1-2), 58-66.

Houtz, E.F., Higgins, C.P., Field, J.A. and Sedlak, D.L. (2013) Persistence of Perfluoroalkyl Acid Precursors in AFFF-Impacted Groundwater and Soil. Environmental science & technology 47(15), 8187-8195.

Hu, J., An, W., Wang, H., Geng, J., Cui, W. and Zhan, Y. (2016) Synthesis of a hierarchical BiOBr nanodots/Bi_2WO_6 p–n heterostructure with enhanced photoinduced electric and photocatalytic degradation performance. RSC Advances 6(35), 29554-29562.

Hu, J., Fan, W., Ye, W., Huang, C. and Qiu, X. (2014) Insights into the photosensitivity activity of BiOCl under visible light irradiation. Applied Catalysis B: Environmental 158-159, 182-189.

Huang, D., de Vera, G.A., Chu, C., Zhu, Q., Stavitski, E., Mao, J., Xin, H., Spies, J.A., Schmuttenmaer, C.A., Niu, J., Haller, G.L. and Kim, J.-H. (2018) Single-Atom Pt Catalyst for Effective C–F Bond Activation via Hydrodefluorination. ACS Catalysis 8(10), 9353-9358.

Huang, D., Yin, L. and Niu, J. (2016a) Photoinduced Hydrodefluorination Mechanisms of Perfluorooctanoic Acid by the SiC/Graphene Catalyst. Environmental Science & Technology 50(11), 5857-5863.

Huang, H., Ye, X., Huang, H., Zhang, L. and Leung, D.Y.C. (2013) Mechanistic study on formaldehyde removal over Pd/TiO2 catalysts: Oxygen transfer and role of water vapor. Chemical Engineering Journal 230, 73-79.

Huang, J., Wang, X., Pan, Z., Li, X., Ling, Y. and Li, L. (2016b) Efficient degradation of perfluorooctanoic acid (PFOA) by photocatalytic ozonation. Chemical Engineering Journal 296, 329-334.

Huang, S. and Jaffé, P.R. (2019) Defluorination of Perfluorooctanoic Acid (PFOA) and Perfluorooctane Sulfonate (PFOS) by Acidimicrobium sp. Strain A6. Environmental science & technology 53(19), 11410-11419.

Huang, Y., Yu, Y., Yu, Y. and Zhang, B. (2020) Oxygen Vacancy Engineering in Photocatalysis. Solar RRL 4(8), 2000037.

Ida, S., Kim, N., Ertekin, E., Takenaka, S. and Ishihara, T. (2015) Photocatalytic Reaction Centers in Two-Dimensional Titanium Oxide Crystals. Journal of the American Chemical Society 137(1), 239-244.

Ji, T., Liu, Q., Zou, R., Sun, Y., Xu, K., Sang, L., Liao, M., Koide, Y., Yu, L. and Hu, J. (2016) An Interface Engineered Multicolor Photodetector Based on n-Si(111)/TiO2 Nanorod Array Heterojunction. Advanced Functional Materials 26(9), 1400-1410.

Jiang, F., Zhao, H., Chen, H., Xu, C. and Chen, J. (2016) Enhancement of photocatalytic decomposition of perfluorooctanoic acid on CeO_2/In_2O_3. RSC Advances 6(76), 72015-72021.

Jiang, J., Zhao, K., Xiao, X. and Zhang, L. (2012) Synthesis and Facet-Dependent Photoreactivity of BiOCl Single-Crystalline Nanosheets. Journal of the American Chemical Society 134(10), 4473-4476.

Jiao, L. and Jiang, H.-L. (2019) Metal-Organic-Framework-Based Single-Atom Catalysts for Energy Applications. Chem.

Jin, L.-N., Liu, Q. and Sun, W.-Y. (2013) Size-controlled indium(iii)–benzenedicarboxylate hexagonal rods and their transformation to In_2O_3 hollow structures. CrystEngComm 15(23).

Johansson, N., Fredriksson, A. and Eriksson, P. (2008) Neonatal exposure to perfluorooctane sulfonate (PFOS) and perfluorooctanoic acid (PFOA) causes neurobehavioural defects in adult mice. NeuroToxicology 29(1), 160-169.

Kannan, K., Corsolini, S., Falandysz, J., Fillmann, G. and Aldoust, K.M. (2004) Perfluorooctanesulfonate and Related Fluorochemicals in Human Blood from Several Countries. Environmental Science & Technology 38(17), 4489-4495.

Kapilashrami, M., Zhang, Y., Liu, Y.-S., Hagfeldt, A. and Guo, J. (2014) Probing the Optical Property and Electronic Structure of TiO_2 Nanomaterials for Renewable Energy Applications. Chemical Reviews 114(19), 9662-9707.

Karimi-Nazarabad, M., Ahmadzadeh, H. and Goharshadi, E.K. (2021) Porous perovskite-lanthanum cobaltite as an efficient cocatalyst in photoelectrocatalytic water oxidation by bismuth doped g-C3N4. Solar energy 227, 426-437.

Kistler, J.D., Chotigkrai, N., Xu, P., Enderle, B., Praserthdam, P., Chen, C.Y., Browning, N.D. and Gates, B.C.J.A.C.I.E. (2014) A single-site platinum CO oxidation catalyst in zeolite KLTL: microscopic and spectroscopic determination of the locations of the platinum atoms. 53(34), 8904-8907.

Kuriki, R., Yamamoto, M., Higuchi, K., Yamamoto, Y., Akatsuka, M., Lu, D., Yagi, S., Yoshida, T., Ishitani, O. and Maeda, K.J.A.C. (2017) Robust binding between carbon nitride nanosheets and a binuclear ruthenium (II) complex enabling durable, selective CO2 reduction under visible light in aqueous solution. 129(17), 4945-4949.

Lau, C., Anitole, K., Hodes, C., Lai, D., Pfahles-Hutchens, A. and Seed, J. (2007) Perfluoroalkyl acids: a review of monitoring and toxicological findings. Toxicological sciences 99(2), 366-394.

Lee, B.-H., Park, S., Kim, M., Sinha, A.K., Lee, S.C., Jung, E., Chang, W.J., Lee, K.-S., Kim, J.H. and Cho, S.-P. (2019) Reversible and cooperative photoactivation of single-atom Cu/TiO_2 photocatalysts. Nature materials 18(6), 620-626.

Lee, J., Farha, O.K., Roberts, J., Scheidt, K.A., Nguyen, S.T. and Hupp, J.T. (2009) Metal–organic framework materials as catalysts. Chemical Society Reviews 38(5), 1450-1459.

Lehmler, H.-J. (2005) Synthesis of environmentally relevant fluorinated surfactants—a review. Chemosphere 58(11), 1471-1496.

Lei, F., Sun, Y., Liu, K., Gao, S., Liang, L., Pan, B. and Xie, Y. (2014) Oxygen vacancies confined in ultrathin indium oxide porous sheets for promoted visible-light water splitting. J Am Chem Soc 136(19), 6826-6829.

Li, F., Duan, J., Tian, S., Ji, H., Zhu, Y., Wei, Z. and Zhao, D. (2020a) Short-chain per- and polyfluoroalkyl substances in aquatic systems: Occurrence, impacts and treatment. Chemical Engineering Journal 380.

Li, F., Wei, Z., He, K., Blaney, L., Cheng, X., Xu, T., Liu, W. and Zhao, D. (2020b) A concentrate-and-destroy technique for degradation of perfluorooctanoic acid in water using a new adsorptive photocatalyst. Water Res 185, 116219.

Li, J., Cai, L., Shang, J., Yu, Y. and Zhang, L. (2016a) Giant Enhancement of Internal Electric Field Boosting Bulk Charge Separation for Photocatalysis. Advanced Materials 28(21), 4059-4064.

Li, J., Li, H., Zhan, G. and Zhang, L. (2017a) Solar Water Splitting and Nitrogen Fixation with Layered Bismuth Oxyhalides. Accounts of Chemical Research 50(1), 112-121.

Li, K., Fang, X., Fu, Z., Yang, Y., Nabi, I., Feng, Y., Bacha, A.-U.-R. and Zhang, L. (2020c) Boosting photocatalytic chlorophenols remediation with addition of sulfite and mechanism investigation by in-situ DRIFTs. Journal of hazardous materials 398, 123007.

Li, M., Yu, Z., Liu, Q., Sun, L. and Huang, W. (2016b) Photocatalytic decomposition of perfluorooctanoic acid by noble metallic nanoparticles modified TiO_2.

Chemical Engineering Journal 286, 232-238.

Li, Q., Wang, T., Zhu, Z., Meng, J., Wang, P., Suriyanarayanan, S., Zhang, Y., Zhou, Y., Song, S., Lu, Y. and Yvette, B. (2017b) Using hydrodynamic model to predict PFOS and PFOA transport in the Daling River and its tributary, a heavily polluted river into the Bohai Sea, China. Chemosphere 167, 344-352.

Li, R., Luan, Q., Dong, C., Dong, W., Tang, W., Wang, G. and Lu, Y. (2021) Light-facilitated structure reconstruction on self-optimized photocatalyst TiO_2@BiOCl for selectively efficient conversion of CO_2 to CH_4. Applied Catalysis B: Environmental 286, 119832.

Li, S., Chang, L., Peng, J., Gao, J., Lu, J., Zhang, F., Zhu, G. and Hojamberdiev, M. (2020d) Bi0 nanoparticle loaded on Bi^{3+}-doped $ZnWO_4$ nanorods with oxygen vacancies for enhanced photocatalytic NO removal. Journal of Alloys and Compounds 818, 152837.

Li, T., Wang, C., Wang, T. and Zhu, L. (2019) Highly efficient photocatalytic degradation toward perfluorooctanoic acid by bromine doped BiOI with high exposure of (001) facet. Applied Catalysis B: Environmental, 118442.

Li, W., Tian, Y., Li, H., Zhao, C., Zhang, B., Zhang, H., Geng, W. and Zhang, Q. (2016c) Novel BiOCl/TiO_2 hierarchical composites: Synthesis, characterization and application on photocatalysis. Applied Catalysis A: General 516, 81-89.

Li, X., Zhang, P., Jin, L., Shao, T., Li, Z. and Cao, J. (2012a) Efficient Photocatalytic Decomposition of Perfluorooctanoic Acid by Indium Oxide and Its Mechanism. Environmental Science & Technology 46(10), 5528-5534.

Li, X., Zhang, P., Jin, L., Shao, T., Li, Z. and Cao, J. (2012b) Efficient photocatalytic decomposition of perfluorooctanoic acid by indium oxide and its mechanism. Environ Sci Technol 46(10), 5528-5534.

Li, Z., Del Cul, G.D., Yan, W., Liang, C. and Dai, S. (2004) Fluorinated Carbon with Ordered Mesoporous Structure. Journal of the American Chemical Society 126(40), 12782-12783.

Li, Z., Zhang, P., Li, J., Shao, T. and Jin, L. (2013a) Synthesis of In_2O_3-graphene composites and their photocatalytic performance towards perfluorooctanoic acid decomposition. Journal of Photochemistry and Photobiology A: Chemistry 271, 111-116.

Li, Z., Zhang, P., Li, J., Shao, T., Wang, J. and Jin, L. (2014) Synthesis of In_2O_3 porous nanoplates for photocatalytic decomposition of perfluorooctanoic acid (PFOA). Catalysis Communications 43, 42-46.

Li, Z., Zhang, P., Shao, T. and Li, X. (2012c) In_2O_3 nanoporous nanosphere: A highly efficient photocatalyst for decomposition of perfluorooctanoic acid. Applied Catalysis B: Environmental 125, 350-357.

Li, Z., Zhang, P., Shao, T., Wang, J., Jin, L. and Li, X. (2013b) Different nanostructured In_2O_3 for photocatalytic decomposition of perfluorooctanoic acid (PFOA). Journal of hazardous materials 260, 40-46.

Li, Z., Zhang, P., Shao, T., Wang, J., Jin, L. and Li, X. (2013c) Different nanostructured In_2O_3 for photocatalytic decomposition of perfluorooctanoic acid (PFOA). J Hazard Mater 260, 40-46.

Lin, A.Y.-C., Panchangam, S.C. and Ciou, P.-S.J.C. (2010) High levels of perfluorochemicals in Taiwan's wastewater treatment plants and downstream rivers pose great risk to local aquatic ecosystems. 80(10), 1167-1174.

Linic, S., Christopher, P. and Ingram, D.B. (2011) Plasmonic-metal nanostructures for efficient conversion of solar to chemical energy. Nature Materials 10(12), 911-921.

Liu, D., Xiu, Z., Liu, F., Wu, G., Adamson, D., Newell, C., Vikesland, P., Tsai, A.L. and

Alvarez, P.J. (2013) Perfluorooctanoic acid degradation in the presence of Fe(III) under natural sunlight. J Hazard Mater 262, 456-463.

Liu, G., Feng, C. and Shao, P. (2021a) Degradation of Perfluorooctanoic Acid with Hydrated Electron by a Heterogeneous Catalytic System. Environmental Science & Technology.

Liu, G., Wang, T., Ouyang, S., Liu, L., Jiang, H., Yu, Q., Kako, T. and Ye, J. (2015) Band-structure-controlled BiO (ClBr)(1− x)/2 I x solid solutions for visible-light photocatalysis. Journal of Materials Chemistry A 3(15), 8123-8132.

Liu, J., Qu, R., Wang, Z., Mendoza-Sanchez, I. and Sharma, V.K. (2017a) Thermal- and photo-induced degradation of perfluorinated carboxylic acids: Kinetics and mechanism. Water Res 126, 12-18.

Liu, P., Zhao, Y., Qin, R., Mo, S., Chen, G., Gu, L., Chevrier, D.M., Zhang, P., Guo, Q., Zang, D., Wu, B., Fu, G. and Zheng, N. (2016) Photochemical route for synthesizing atomically dispersed palladium catalysts. Science 352(6287), 797-800.

Liu, X.-Q., Chen, W.-J. and Jiang, H. (2017b) Facile synthesis of Ag/Ag_3PO_4/AMB composite with improved photocatalytic performance. Chemical Engineering Journal 308, 889-896.

Liu, X., Chen, Z., Tian, K., Zhu, F., Hao, D., Cheng, D., Wei, W., Zhang, L. and Ni, B.-J. (2021b) Fe^{3+} Promoted the Photocatalytic Defluorination of Perfluorooctanoic Acid (PFOA) over In_2O_3. ACS ES&T Water 1(11), 2431-2439.

Liu, X., Wei, W., Xu, J., Wang, D., Song, L. and Ni, B.-J. (2020) Photochemical decomposition of perfluorochemicals in contaminated water. Water Research 186, 116311.

Liu, X., Xu, B., Duan, X., Hao, Q., Wei, W., Wang, S. and Ni, B.-J. (2021c) Facile preparation of hydrophilic In_2O_3 nanospheres and rods with improved performances for photocatalytic degradation of PFOA. Environmental Science: Nano 8(4), 1010-1018.

Liu, X., Zhou, K., Wang, L., Wang, B. and Li, Y. (2009) Oxygen vacancy clusters promoting reducibility and activity of ceria nanorods. Journal of the American Chemical Society 131(9), 3140-3141.

Long, J.R. and Yaghi, O.M. (2009) The pervasive chemistry of metal–organic frameworks. Chemical Society Reviews 38(5), 1213-1214.

Low, J., Yu, J., Jaroniec, M., Wageh, S. and Al-Ghamdi, A.A. (2017) Heterojunction Photocatalysts. Adv Mater 29(20).

Makowski, P., Demir Cakan, R., Antonietti, M., Goettmann, F. and Titirici, M.-m. (2008) Selective partial hydrogenation of hydroxy aromatic derivatives with palladium nanoparticles supported on hydrophilic carbon. Chemical Communications (8), 999-1001.

Martin, J.W., Mabury, S.A., Solomon, K.R. and Muir, D.C. (2003) Dietary accumulation of perfluorinated acids in juvenile rainbow trout (Oncorhynchus mykiss). Environmental Toxicology and Chemistry: An International Journal 22(1), 189-195.

Morgan, W.E., Stec, W.J. and Van Wazer, J.R. (1973) Inner-orbital binding-energy shifts of antimony and bismuth compounds. Inorganic Chemistry 12(4), 953-955.

Mulabagal, V., Liu, L., Qi, J., Wilson, C. and Hayworth, J.S. (2018) A rapid UHPLC-MS/MS method for simultaneous quantitation of 23 perfluoroalkyl substances (PFAS) in estuarine water. Talanta 190, 95-102.

Munirathinam, B., Pydimukkala, H., Ramaswamy, N. and Neelakantan, L. (2015) Influence of crystallite size and surface morphology on electrochemical properties of annealed TiO_2 nanotubes. Applied Surface Science 355, 1245-1253.

Nakamoto, K. (2009) Infrared and Raman spectra of inorganic and coordination compounds, Wiley, Hoboken, N.J.

Nie, M., Lu, S., Lei, D., Yang, C. and Zhao, Z. (2017) Rapid synthesis of ZIF-8 nanocrystals for electrochemical detection of dopamine. Journal of The Electrochemical Society 164(13), H952-H957.

Ochoa-Herrera, V., Field, J.A., Luna-Velasco, A. and Sierra-Alvarez, R. (2016) Microbial toxicity and biodegradability of perfluorooctane sulfonate (PFOS) and shorter chain perfluoroalkyl and polyfluoroalkyl substances (PFASs). Environmental Science: Processes & Impacts 18(9), 1236-1246.

Ouyang, W., Teng, F. and Fang, X. (2018) High Performance BiOCl Nanosheets/TiO_2 Nanotube Arrays Heterojunction UV Photodetector: The Influences of Self-Induced Inner Electric Fields in the BiOCl Nanosheets. Advanced Functional Materials 28(16), 1707178.

Palchan, I., Crespin, M., Estrade-Szwarckopf, H. and Rousseau, B. (1989) Graphite fluorides: An XPS study of a new type of C-F bonding. Chemical Physics Letters 157(4), 321-327.

Pan, Y., Zhang, C., Liu, Z., Chen, C. and Li, Y. (2020) Structural Regulation with Atomic-Level Precision: From Single-Atomic Site to Diatomic and Atomic Interface Catalysis. Matter 2(1), 78-110.

Panchangam, S.C., Lin, A.Y., Shaik, K.L. and Lin, C.F. (2009) Decomposition of perfluorocarboxylic acids (PFCAs) by heterogeneous photocatalysis in acidic aqueous medium. Chemosphere 77(2), 242-248.

Peng, D., Zhang, Y., Xu, G., Tian, Y., Ma, D., Zhang, Y. and Qiu, P. (2020) Synthesis of Multilevel Structured MoS2@Cu/Cu2O@C Visible-Light-Driven Photocatalyst Derived from MOF–Guest Polyhedra for Cyclohexane Oxidation. ACS Sustainable Chemistry & Engineering 8(17), 6622-6633.

Post, G.B., Louis, J.B., Cooper, K.R., Boros-Russo, B.J. and Lippincott, R.L. (2009) Occurrence and Potential Significance of Perfluorooctanoic Acid (PFOA) Detected in New Jersey Public Drinking Water Systems. Environmental Science & Technology 43(12), 4547-4554.

Prevedouros, K., Cousins, I.T., Buck, R.C. and Korzeniowski, S.H. (2006) Sources, Fate and Transport of Perfluorocarboxylates. Environmental Science & Technology 40(1), 32-44.

Qian, L., Georgi, A., Gonzalez-Olmos, R. and Kopinke, F.-D. (2020) Degradation of perfluorooctanoic acid adsorbed on Fe-zeolites with molecular oxygen as oxidant under UV-A irradiation. Applied Catalysis B: Environmental 278, 119283.

Qian, L., Kopinke, F.-D. and Georgi, A. (2021) Photodegradation of Perfluorooctanesulfonic Acid on Fe-Zeolites in Water. Environmental science & technology 55(1), 614-622.

Qin, Q., Guo, Y., Zhou, D., Yang, Y. and Guo, Y. (2016) Facile growth and composition-dependent photocatalytic activity of flowerlike BiOCl1− xBrx hierarchical microspheres. Applied Surface Science 390, 765-777.

Qu, R., Liu, J., Li, C., Wang, L., Wang, Z. and Wu, J. (2016) Experimental and theoretical insights into the photochemical decomposition of environmentally persistent perfluorocarboxylic acids. Water Res 104, 34-43.

Ren, J., Woo, Y.C., Yao, M., Lim, S., Tijing, L.D. and Shon, H.K. (2019) Nanoscale zero-valent iron (nZVI) immobilization onto graphene oxide (GO)-incorporated electrospun polyvinylidene fluoride (PVDF) nanofiber membrane for groundwater remediation via gravity-driven membrane filtration. Science of the Total

Environment 688, 787-796.

Rotzinger, F.P., Kesselman-Truttmann, J.M., Hug, S.J., Shklover, V. and Gratzel, M. (2004a) Structure and vibrational spectrum of formate and acetate adsorbed from aqueous solution onto the TiO2 rutile (110) surface. Journal of Physical Chemistry B 108(16), 5004-5017.

Rotzinger, F.P., Kesselman-Truttmann, J.M., Hug, S.J., Shklover, V. and Grätzel, M. (2004b) Structure and vibrational spectrum of formate and acetate adsorbed from aqueous solution onto the TiO2 rutile (110) surface. The Journal of Physical Chemistry B 108(16), 5004-5017.

Sahu, S.P., Qanbarzadeh, M., Ateia, M., Torkzadeh, H., Maroli, A.S. and Cates, E.L. (2018) Rapid Degradation and Mineralization of Perfluorooctanoic Acid by a New Petitjeanite Bi3O(OH)(PO4)2 Microparticle Ultraviolet Photocatalyst. Environmental Science & Technology Letters 5(8), 533-538.

Schultz, M.M., Barofsky, D.F., Field, J.A.J.E.s. and technology (2004) Quantitative determination of fluorotelomer sulfonates in groundwater by LC MS/MS. 38(6), 1828-1835.

Schultz, M.M., Higgins, C.P., Huset, C.A., Luthy, R.G., Barofsky, D.F. and Field, J.A. (2006) Fluorochemical Mass Flows in a Municipal Wastewater Treatment Facility. Environmental Science & Technology 40(23), 7350-7357.

Shang, H., Li, M., Li, H., Huang, S., Mao, C., Ai, Z. and Zhang, L. (2019) Oxygen Vacancies Promoted the Selective Photocatalytic Removal of NO with Blue TiO2 via Simultaneous Molecular Oxygen Activation and Photogenerated Hole Annihilation. Environmental science & technology 53(11), 6444-6453.

Shao, T., Zhang, P., Jin, L. and Li, Z. (2013a) Photocatalytic decomposition of perfluorooctanoic acid in pure water and sewage water by nanostructured gallium oxide. Applied Catalysis B: Environmental 142-143, 654-661.

Shao, T., Zhang, P., Li, Z. and Jin, L. (2013b) Photocatalytic decomposition of perfluorooctanoic acid in pure water and wastewater by needle-like nanostructured gallium oxide. Chinese Journal of Catalysis 34(8), 1551-1559.

Shenawi-Khalil, S., Uvarov, V., Fronton, S., Popov, I. and Sasson, Y. (2012) A Novel Heterojunction BiOBr/Bismuth Oxyhydrate Photocatalyst with Highly Enhanced Visible Light Photocatalytic Properties. The Journal of Physical Chemistry C 116(20), 11004-11012.

Shi, S., Zhang, F., Lin, H., Wang, Q., Shi, E. and Qu, F. (2018) Enhanced triethylamine-sensing properties of P-N heterojunction Co3O4/In2O3 hollow microtubes derived from metal–organic frameworks. Sensors and Actuators B: Chemical 262, 739-749.

Song, T., Yu, X., Tian, N. and Huang, H.-w. (2021) Preparation, structure and application of g-C3N4/BiOX composite photocatalyst. International Journal of Hydrogen Energy 46(2), 1857-1878.

Song, Z., Dong, X., Fang, J., Xiong, C., Wang, N. and Tang, X. (2019) Improved photocatalytic degradation of perfluorooctanoic acid on oxygen vacancies-tunable bismuth oxychloride nanosheets prepared by a facile hydrolysis. J Hazard Mater 377, 371-380.

Song, Z., Dong, X., Wang, N., Zhu, L., Luo, Z., Fang, J. and Xiong, C. (2017) Efficient photocatalytic defluorination of perfluorooctanoic acid over BiOCl nanosheets via a hole direct oxidation mechanism. Chemical Engineering Journal 317, 925-934.

Sun, H., Li, F., Zhang, T., Zhang, X., He, N., Song, Q., Zhao, L., Sun, L. and Sun, T. (2011) Perfluorinated compounds in surface waters and WWTPs in Shenyang, China: Mass flows and source analysis. Water Research 45(15), 4483-4490.

Sun, K., Rui, N., Zhang, Z., Sun, Z., Ge, Q. and Liu, C.-J. (2020a) A highly active Pt/In2O3 catalyst for CO2 hydrogenation to methanol with enhanced stability. Green Chemistry 22(15), 5059-5066.

Sun, L., Xiang, L., Zhao, X., Jia, C.-J., Yang, J., Jin, Z., Cheng, X. and Fan, W. (2015) Enhanced Visible-Light Photocatalytic Activity of BiOI/BiOCl Heterojunctions: Key Role of Crystal Facet Combination. ACS Catalysis 5(6), 3540-3551.

Sun, Y., Li, G., Wang, W., Gu, W., Wong, P.K. and An, T. (2019) Photocatalytic defluorination of perfluorooctanoic acid by surface defective BiOCl: Fast microwave solvothermal synthesis and photocatalytic mechanisms. J Environ Sci (China) 84, 69-79.

Sun, Y., Mwandeje, J.B., Wangatia, L.M., Zabihi, F., Nedeljković, J. and Yang, S. (2020b) Enhanced Photocatalytic Performance of Surface-Modified TiO2 Nanofibers with Rhodizonic Acid. Advanced Fiber Materials 2(2), 118-122.

Sun, Y., Zhao, Z., Suematsu, K., Li, P., Yu, Z., Zhang, W., Hu, J. and Shimanoe, K. (2020c) Rapid and Stable Detection of Carbon Monoxide in Changing Humidity Atmospheres Using Clustered In2O3/CuO Nanospheres. ACS Sensors 5(4), 1040-1049.

Surdhar, P.S., Mezyk, S.P. and Armstrong, D.A. (1989) Reduction potential of the carboxyl radical anion in aqueous solutions. The Journal of Physical Chemistry 93(8), 3360-3363.

Teng, W., Li, X., Zhao, Q. and Chen, G. (2013) Fabrication of Ag/Ag 3 PO 4/TiO 2 heterostructure photoelectrodes for efficient decomposition of 2-chlorophenol under visible light irradiation. Journal of Materials Chemistry A 1(32), 9060-9068.

Tenorio, R., Liu, J., Xiao, X., Maizel, A., Higgins, C.P., Schaefer, C.E. and Strathmann, T.J. (2020) Destruction of Per- and Polyfluoroalkyl Substances (PFASs) in Aqueous Film-Forming Foam (AFFF) with UV-Sulfite Photoreductive Treatment. Environ Sci Technol 54(11), 6957-6967.

Trojanowicz, M., Bojanowska-Czajka, A., Bartosiewicz, I. and Kulisa, K. (2018) Advanced Oxidation/Reduction Processes treatment for aqueous perfluorooctanoate (PFOA) and perfluorooctanesulfonate (PFOS) – A review of recent advances. Chemical Engineering Journal 336, 170-199.

Wan, Z., Mao, Q. and Chen, Q. (2021) Proton-dependent photocatalytic dehalogenation activities caused by oxygen vacancies of In2O3. Chemical Engineering Journal 403, 126389.

Wang, F., Jiang, Y., Lawes, D.J., Ball, G.E., Zhou, C., Liu, Z. and Amal, R. (2015) Analysis of the Promoted Activity and Molecular Mechanism of Hydrogen Production over Fine Au–Pt Alloyed TiO2 Photocatalysts. ACS Catalysis 5(7), 3924-3931.

Wang, H., Jiang, S.L., Chen, S.C., Li, D.D., Zhang, X.D., Shao, W., Sun, X.S., Xie, J.F., Zhao, Z., Zhang, Q., Tian, Y.P. and Xie, Y. (2016) Enhanced Singlet Oxygen Generation in Oxidized Graphitic Carbon Nitride for Organic Synthesis. Advanced Materials 28(32), 6940-+.

Wang, J., Cao, C., Wang, Y., Wang, Y., Sun, B. and Zhu, L. (2019a) In situ preparation of pn BiOI@ Bi5O7I heterojunction for enhanced PFOA photocatalytic degradation under simulated solar light irradiation. Chemical Engineering Journal, 123530.

Wang, J., Cao, C., Zhang, Y., Zhang, Y. and Zhu, L. (2021a) Underneath mechanisms into the super effective degradation of PFOA by BiOF nanosheets with tunable oxygen vacancies on exposed (101) facets. Applied Catalysis B: Environmental 286, 119911.

Wang, J., Liu†, Z. and Cai, R. (2008a) A New Role for Fe3+ in TiO2 Hydrosol: Accelerated Photodegradation of Dyes under Visible Light. Environmental science & technology 42(15), 5759-5764.

Wang, L., Dong, Y., Yan, T., Hu, Z., Jelle, A.A., Meira, D.M., Duchesne, P.N., Loh, J.Y.Y., Qiu, C., Storey, E.E., Xu, Y., Sun, W., Ghoussoub, M., Kherani, N.P., Helmy, A.S. and Ozin, G.A. (2020a) Black indium oxide a photothermal CO2 hydrogenation catalyst. Nat Commun 11(1), 2432.

Wang, L., Dong, Y., Yan, T., Hu, Z., Jelle, A.A., Meira, D.M., Duchesne, P.N., Loh, J.Y.Y., Qiu, C., Storey, E.E., Xu, Y., Sun, W., Ghoussoub, M., Kherani, N.P., Helmy, A.S. and Ozin, G.A. (2020b) Black indium oxide a photothermal CO2 hydrogenation catalyst. Nature communications 11(1), 2432.

Wang, N., Lv, H., Zhou, Y., Zhu, L., Hu, Y., Majima, T. and Tang, H. (2019b) Complete Defluorination and Mineralization of Perfluorooctanoic Acid by a Mechanochemical Method Using Alumina and Persulfate. Environ Sci Technol 53(14), 8302-8313.

Wang, P., Wang, J., An, X., Shi, J., Shangguan, W., Hao, X., Xu, G., Tang, B., Abudula, A. and Guan, G. (2021b) Generation of abundant defects in Mn-Co mixed oxides by a facile agar-gel method for highly efficient catalysis of total toluene oxidation. Applied Catalysis B: Environmental 282, 119560.

Wang, Q., Li, P., Zhang, Z., Jiang, C., Zuojiao, K., Liu, J. and Wang, Y. (2019c) Kinetics and mechanism insights into the photodegradation of tetracycline hydrochloride and ofloxacin mixed antibiotics with the flower-like BiOCl/TiO2 heterojunction. Journal of Photochemistry and Photobiology A: Chemistry 378, 114-124.

Wang, S., Hai, X., Ding, X., Chang, K., Xiang, Y., Meng, X., Yang, Z., Chen, H. and Ye, J. (2017a) Light-switchable oxygen vacancies in ultrafine Bi5O7Br nanotubes for boosting solar-driven nitrogen fixation in pure water. Advanced Materials 29(31), 1701774.

Wang, S., Yang, Q., Chen, F., Sun, J., Luo, K., Yao, F., Wang, X., Wang, D., Li, X. and Zeng, G. (2017b) Photocatalytic degradation of perfluorooctanoic acid and perfluorooctane sulfonate in water: A critical review. Chemical Engineering Journal 328, 927-942.

Wang, T., Liu, Y., Deng, Y., Fu, H., Zhang, L. and Chen, J. (2018) The influence of temperature on the heterogeneous uptake of SO2 on hematite particles. Science of the Total Environment 644, 1493-1502.

Wang, W.J., Chen, Y., Li, G.Y., Gu, W.Q. and An, T.C. (2020c) Photocatalytic reductive defluorination of perfluorooctanoic acid in water under visible light irradiation: the role of electron donor. Environmental Science-Water Research & Technology 6(6), 1638-1648.

Wang, Y., Lee, W.C., Manga, K.K., Ang, P.K., Lu, J., Liu, Y.P., Lim, C.T. and Loh, K.P. (2012) Fluorinated Graphene for Promoting Neuro-Induction of Stem Cells. Advanced Materials 24(31), 4285-4290.

Wang, Y. and Zhang, P. (2011) Photocatalytic decomposition of perfluorooctanoic acid (PFOA) by TiO2 in the presence of oxalic acid. J Hazard Mater 192(3), 1869-1875.

Wang, Y., Zhang, P., Pan, G. and Chen, H. (2008b) Ferric ion mediated photochemical decomposition of perfluorooctanoic acid (PFOA) by 254nm UV light. J Hazard Mater 160(1), 181-186.

Wang, Z., Chen, M., Huang, D., Zeng, G., Xu, P., Zhou, C., Lai, C., Wang, H., Cheng, M. and Wang, W. (2019d) Multiply structural optimized strategies for bismuth oxyhalide photocatalysis and their environmental application. Chemical Engineering Journal 374, 1025-1045.

Wei, H., Huang, K., Wang, D., Zhang, R., Ge, B., Ma, J., Wen, B., Zhang, S., Li, Q., Lei, M., Zhang, C., Irawan, J., Liu, L.-M. and Wu, H. (2017) Iced photochemical reduction to synthesize atomically dispersed metals by suppressing nanocrystal growth. Nature Communications 8(1), 1490.

Wei, L., Yu, C., Zhang, Q., Liu, H. and Wang, Y. (2018) TiO2-based heterojunction photocatalysts for photocatalytic reduction of CO2 into solar fuels. Journal of Materials Chemistry A 6(45), 22411-22436.

Wen, H., Long, Y., Han, W., Wu, W., Yang, Y. and Ma, J. (2018) Preparation of a novel bimetallic AuCu-P25-rGO ternary nanocomposite with enhanced photocatalytic degradation performance. Applied Catalysis A: General 549, 237-244.

Weon, S., Suh, M.-J., Chu, C., Huang, D., Stavitski, E. and Kim, J.-H. (2021) Site-Selective Loading of Single-Atom Pt on TiO2 for Photocatalytic Oxidation and Reductive Hydrodefluorination. ACS ES&T Engineering 1(3), 512-522.

WookáLee, Y. and WooáHan, S. (2010) The direct growth of gold rods on graphene thin films. Chemical Communications 46(18), 3185-3187.

Wu, B., Hao, S., Choi, Y., Higgins, C.P., Deeb, R., Strathmann, T.J.J.E.S. and Letters, T. (2019a) Rapid destruction and defluorination of perfluorooctanesulfonate by alkaline hydrothermal reaction. 6(10), 630-636.

Wu, Q., Shen, C., Rui, N., Sun, K. and Liu, C.-j. (2021) Experimental and theoretical studies of CO2 hydrogenation to methanol on Ru/In2O3. Journal of CO2 Utilization 53, 101720.

Wu, Y., Li, Y., Fang, C. and Li, C. (2019b) Highly Efficient Degradation of Perfluorooctanoic Acid over a MnOx-Modified Oxygen-Vacancy-Rich In2O3 Photocatalyst. ChemCatChem 11(9), 2297-2303.

Wu, Y., Li, Y., Fang, C. and Li, C. (2019c) Highly Efficient Degradation of Perfluorooctanoic Acid over a MnOx-Modified Oxygen-Vacancy-Rich In2O3 Photocatalyst. ChemCatChem 11(9), 2297-2303.

Xi, Z., Shi, K., Xu, X., Jing, P., Liu, B., Gao, R. and Zhang, J. (2021) Boosting Nitrogen Reduction Reaction via Electronic Coupling of Atomically Dispersed Bismuth with Titanium Nitride Nanorods. Advanced Science n/a(n/a), 2104245.

Xie, Y., Chen, Y., Yang, J., Liu, C., Zhao, H. and Cao, H. (2018) Distinct synergetic effects in the ozone enhanced photocatalytic degradation of phenol and oxalic acid with Fe3+/TiO2 catalyst. Chinese Journal of Chemical Engineering 26(7), 1528-1535.

Xiong, S.-w., Yu, Y., Wang, P., Liu, M., Chen, S.-h., Yin, X.-z., Wang, L.-x. and Wang, H. (2020) Growth of AgBr/Ag3PO4 Heterojunction on Chitosan Fibers for Degrading Organic Pollutants. Advanced Fiber Materials 2(5), 246-255.

Xu, B., Ahmed, M.B., Zhou, J.L., Altaee, A., Wu, M. and Xu, G. (2017a) Photocatalytic removal of perfluoroalkyl substances from water and wastewater: Mechanism, kinetics and controlling factors. Chemosphere 189, 717-729.

Xu, B., Zhou, J.L., Altaee, A., Ahmed, M.B., Johir, M.A.H., Ren, J. and Li, X. (2019) Improved photocatalysis of perfluorooctanoic acid in water and wastewater by Ga2O3/UV system assisted by peroxymonosulfate. Chemosphere 239, 124722.

Xu, C., Qiu, P., Chen, H. and Jiang, F. (2017b) Platinum modified indium oxide nanorods with enhanced photocatalytic activity on degradation of perfluorooctanoic acid (PFOA). Journal of the Taiwan Institute of Chemical Engineers 80, 761-768.

Xu, J., Wu, M., Yang, J., Wang, Z., Chen, M. and Teng, F. (2017c) Efficient photocatalytic degradation of perfluorooctanoic acid by a wide band gap p -block metal oxyhydroxide InOOH. Applied Surface Science 416, 587-592.

Xu, T., Ji, H., Gu, Y., Tong, T., Xia, Y., Zhang, L. and Zhao, D. (2020a) Enhanced adsorption and photocatalytic degradation of perfluorooctanoic acid in water using iron (hydr)oxides/carbon sphere composite. Chemical Engineering Journal 388, 124230.

Xu, T., Ji, H., Gu, Y., Tong, T., Xia, Y., Zhang, L. and Zhao, D. (2020b) Enhanced adsorption and photocatalytic degradation of perfluorooctanoic acid in water using iron (hydr)oxides/carbon sphere composite. Chemical Engineering Journal 388.

Xu, T., Zhu, Y., Duan, J., Xia, Y., Tong, T., Zhang, L. and Zhao, D. (2020c) Enhanced photocatalytic degradation of perfluorooctanoic acid using carbon-modified bismuth phosphate composite: Effectiveness, material synergy and roles of carbon. Chemical Engineering Journal 395, 124991.

Xue, C., Zhang, T., Ding, S., Wei, J. and Yang, G. (2017) Anchoring Tailored Low-Index Faceted BiOBr Nanoplates onto TiO2 Nanorods to Enhance the Stability and Visible-Light-Driven Catalytic Activity. ACS Appl Mater Interfaces 9(19), 16091-16102.

Yamazaki, S., Matsunaga, S. and Hori, K. (2001) Photocatalytic degradation of trichloroethylene in water using TiO2 pellets. Water Research 35(4), 1022-1028.

Yan, H., Lin, Y., Wu, H., Zhang, W., Sun, Z., Cheng, H., Liu, W., Wang, C., Li, J., Huang, X., Yao, T., Yang, J., Wei, S. and Lu, J. (2017) Bottom-up precise synthesis of stable platinum dimers on graphene. Nature Communications 8(1), 1070.

Yan, T., Long, J., Shi, X., Wang, D., Li, Z. and Wang, X. (2010) Efficient Photocatalytic Degradation of Volatile Organic Compounds by Porous Indium Hydroxide Nanocrystals. Environmental science & technology 44(4), 1380-1385.

Yang, L., Xin, C. and Ning, G. (2008) Computational investigation of interaction between nanoparticles and membranes: hydrophobic/hydrophilic effect.(Report). Journal of Physical Chemistry B 112(51), 16647-16653.

Yang, Q., Xu, Q. and Jiang, H.L. (2017) Metal-organic frameworks meet metal nanoparticles: synergistic effect for enhanced catalysis. Chem Soc Rev 46(15), 4774-4808.

Yang, X., Chen, Y., Qin, L., Wu, X., Wu, Y., Yan, T., Geng, Z. and Zeng, J. (2020a) Boost Selectivity of HCOO− Using Anchored Bi Single Atoms towards CO2 Reduction. ChemSusChem 13(23), 6307-6311.

Yang, X., Sun, S., Cui, J., Yang, M., Luo, Y. and Liang, S. (2021) Synthesis, Functional Modifications, and Diversified Applications of Hybrid BiOCl-Based Heterogeneous Photocatalysts: A Review. Crystal Growth & Design.

Yang, Y., Zheng, Z., Yang, M., Chen, J., Li, C., Zhang, C. and Zhang, X. (2020b) In-situ fabrication of a spherical-shaped Zn-Al hydrotalcite with BiOCl and study on its enhanced photocatalytic mechanism for perfluorooctanoic acid removal performed with a response surface methodology. J Hazard Mater 399, 123070.

Ye, L., Zan, L., Tian, L., Peng, T. and Zhang, J. (2011) The {001} facets-dependent high photoactivity of BiOCl nanosheets. Chemical Communications 47.

Yilmaz, P., Lacerda, A.M., Larrosa, I. and Dunn, S. (2017) Photoelectrocatalysis of Rhodamine B and Solar Hydrogen Production by TiO2 and Pd/TiO2 Catalyst Systems. Electrochimica Acta 231, 641-649.

Yoon, T.P., Ischay, M.A. and Du, J.J.N.c. (2010) Visible light photocatalysis as a greener approach to photochemical synthesis. 2(7), 527-532.

You, X., Yu, L.-l., Xiao, F.-f., Wu, S.-c., Yang, C. and Cheng, J.-h. (2018) Synthesis of phosphotungstic acid-supported bimodal mesoporous silica-based catalyst for defluorination of aqueous perfluorooctanoic acid under vacuum UV irradiation. Chemical Engineering Journal 335, 812-821.

Yu, X., Qiu, H., Wang, Z., Wang, B., Meng, Q., Sun, S., Tang, Y. and Zhao, K. (2021) Constructing the Z-scheme TiO2/Au/BiOI nanocomposite for enhanced photocatalytic nitrogen fixation. Applied Surface Science 556, 149785.

Zhang, E., Wang, T., Yu, K., Liu, J., Chen, W., Li, A., Rong, H., Lin, R., Ji, S., Zheng, X., Wang, Y., Zheng, L., Chen, C., Wang, D., Zhang, J. and Li, Y. (2019a) Bismuth Single Atoms Resulting from Transformation of Metal-Organic Frameworks and Their Use as Electrocatalysts for CO2 Reduction. J Am Chem Soc 141(42), 16569-16573.

Zhang, E., Wang, T., Yu, K., Liu, J., Chen, W., Li, A., Rong, H., Lin, R., Ji, S., Zheng, X., Wang, Y., Zheng, L., Chen, C., Wang, D., Zhang, J. and Li, Y. (2019b) Bismuth Single Atoms Resulting from Transformation of Metal–Organic Frameworks and Their Use as Electrocatalysts for CO2 Reduction. Journal of the American Chemical Society 141(42), 16569-16573.

Zhang, H., Lv, X., Li, Y., Wang, Y. and Li, J. (2010a) P25-Graphene Composite as a High Performance Photocatalyst. ACS Nano 4(1), 380-386.

Zhang, H., Zuo, S., Qiu, M., Wang, S., Zhang, Y., Zhang, J. and Lou, X.W.D. (2020) Direct probing of atomically dispersed Ru species over multi-edged TiO2 for highly efficient photocatalytic hydrogen evolution. Science advances 6(39), eabb9823.

Zhang, K.-L., Liu, C.-M., Huang, F.-Q., Zheng, C. and Wang, W.-D. (2006) Study of the electronic structure and photocatalytic activity of the BiOCl photocatalyst. Applied Catalysis B: Environmental 68(3), 125-129.

Zhang, Z., Shao, C., Li, X., Wang, C., Zhang, M. and Liu, Y. (2010b) Electrospun Nanofibers of p-Type NiO/n-Type ZnO Heterojunctions with Enhanced Photocatalytic Activity. ACS Applied Materials & Interfaces 2(10), 2915-2923.

Zhao, B., Li, X., Yang, L., Wang, F., Li, J., Xia, W., Li, W., Zhou, L. and Zhao, C. (2015) ss-Ga2O3 nanorod synthesis with a one-step microwave irradiation hydrothermal method and its efficient photocatalytic degradation for perfluorooctanoic acid. Photochem Photobiol 91(1), 42-47.

Zhao, B., Lv, M. and Zhou, L. (2012) Photocatalytic degradation of perfluorooctanoic acid with β-Ga2O3 in anoxic aqueous solution. Journal of Environmental Sciences 24(4), 774-780.

Zhao, B. and Zhang, P. (2009) Photocatalytic decomposition of perfluorooctanoic acid with β-Ga2O3 wide bandgap photocatalyst. Catalysis Communications 10(8), 1184-1187.

Zhong, J., Zhao, Y., Ding, L., Ji, H., Ma, W., Chen, C. and Zhao, J. (2019) Opposite photocatalytic oxidation behaviors of BiOCl and TiO2: Direct hole transfer vs. indirect OH oxidation. Applied Catalysis B: Environmental 241, 514-520.

APPENDIX

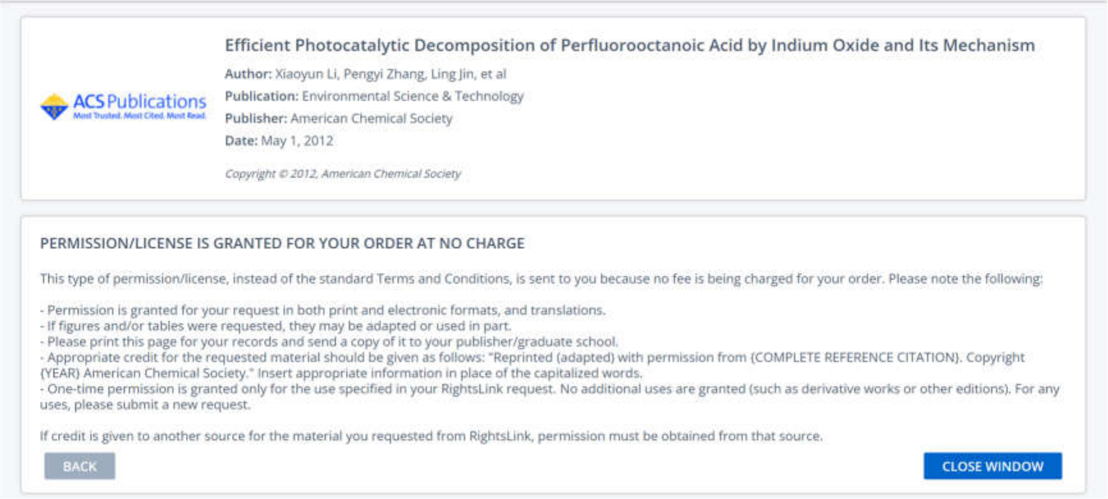

Efficient Photocatalytic Decomposition of Perfluorooctanoic Acid by Indium Oxide and Its Mechanism

Author: Xiaoyun Li, Pengyi Zhang, Ling Jin, et al
Publication: Environmental Science & Technology
Publisher: American Chemical Society
Date: May 1, 2012

PERMISSION/LICENSE IS GRANTED FOR YOUR ORDER AT NO CHARGE

This type of permission/license, instead of the standard Terms and Conditions, is sent to you because no fee is being charged for your order. Please note the following:

- Permission is granted for your request in both print and electronic formats, and translations.
- If figures and/or tables were requested, they may be adapted or used in part.
- Please print this page for your records and send a copy of it to your publisher/graduate school.
- Appropriate credit for the requested material should be given as follows: "Reprinted (adapted) with permission from {COMPLETE REFERENCE CITATION}. Copyright {YEAR} American Chemical Society." Insert appropriate information in place of the capitalized words.
- One-time permission is granted only for the use specified in your RightsLink request. No additional uses are granted (such as derivative works or other editions). For any uses, please submit a new request.

If credit is given to another source for the material you requested from RightsLink, permission must be obtained from that source.

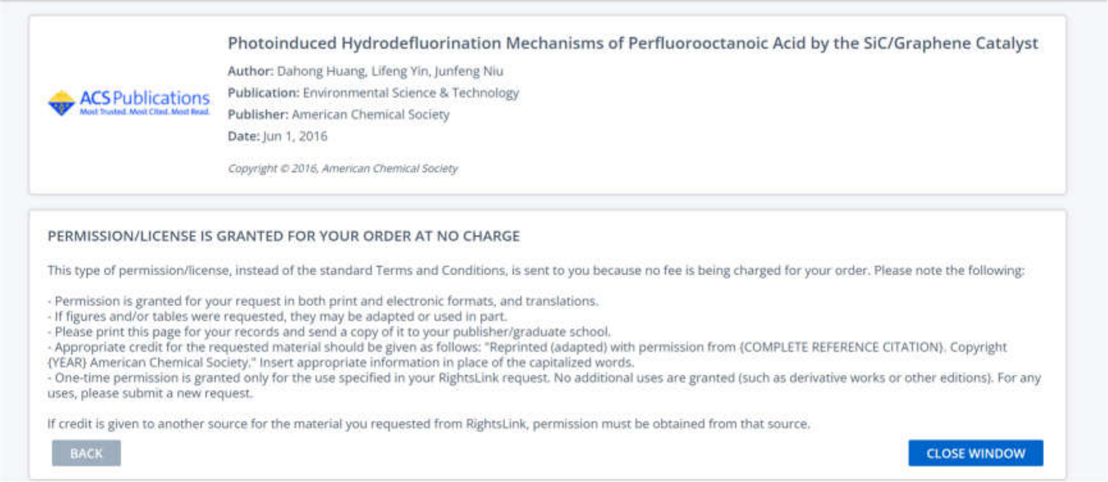

Photoinduced Hydrodefluorination Mechanisms of Perfluorooctanoic Acid by the SiC/Graphene Catalyst

Author: Dahong Huang, Lifeng Yin, Junfeng Niu
Publication: Environmental Science & Technology
Publisher: American Chemical Society
Date: Jun 1, 2016

Copyright © 2016, American Chemical Society

PERMISSION/LICENSE IS GRANTED FOR YOUR ORDER AT NO CHARGE

This type of permission/license, instead of the standard Terms and Conditions, is sent to you because no fee is being charged for your order. Please note the following:

- Permission is granted for your request in both print and electronic formats, and translations.
- If figures and/or tables were requested, they may be adapted or used in part.
- Please print this page for your records and send a copy of it to your publisher/graduate school.
- Appropriate credit for the requested material should be given as follows: "Reprinted (adapted) with permission from {COMPLETE REFERENCE CITATION}. Copyright {YEAR} American Chemical Society." Insert appropriate information in place of the capitalized words.
- One-time permission is granted only for the use specified in your RightsLink request. No additional uses are granted (such as derivative works or other editions). For any uses, please submit a new request.

If credit is given to another source for the material you requested from RightsLink, permission must be obtained from that source.

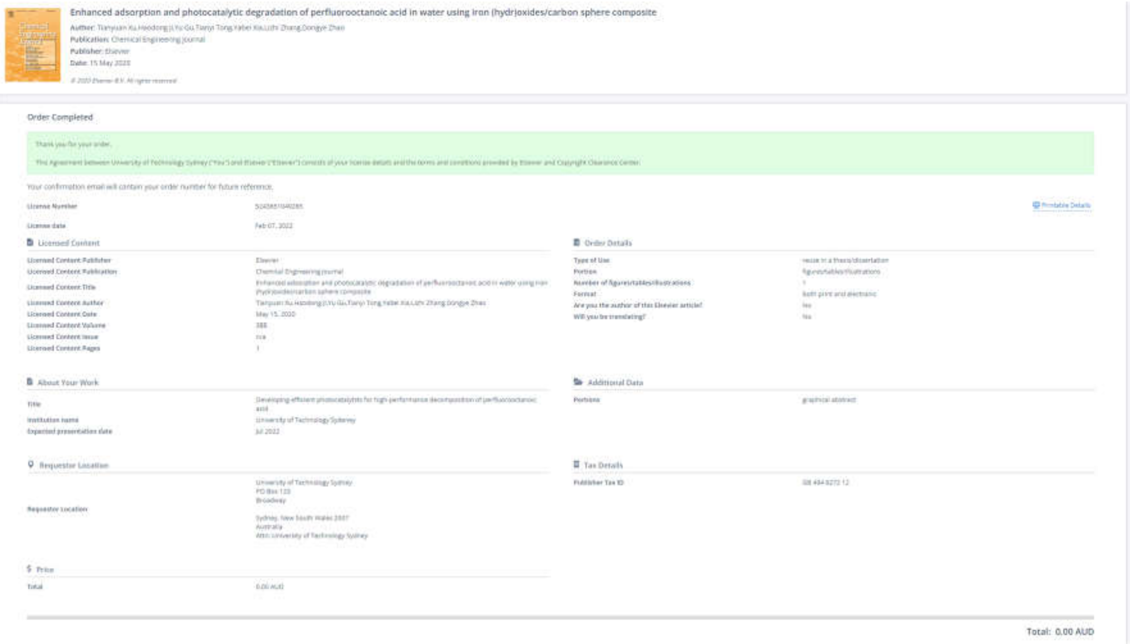

Enhanced adsorption and photocatalytic degradation of perfluorooctanoic acid in water using iron (hydr)oxides/carbon sphere composite

Author: Tianyuan Xu,Haodong Ji,Yu Gu,Tianyi Tong,Yabei Xia,Lizhi Zhang,Dongye Zhao
Publication: Chemical Engineering Journal
Publisher: Elsevier
Date: 15 May 2020

Order Completed

Thank you for your order.

This Agreement between University of Technology Sydney ("You") and Elsevier ("Elsevier") consists of your license details and the terms and conditions provided by Elsevier and Copyright Clearance Center.

Your confirmation email will contain your order number for future reference.

License Number	5243851040285
License date	Feb 07, 2022

Licensed Content

Licensed Content Publisher	Elsevier
Licensed Content Publication	Chemical Engineering Journal
Licensed Content Title	Enhanced adsorption and photocatalytic degradation of perfluorooctanoic acid in water using iron (hydr)oxides/carbon sphere composite
Licensed Content Author	Tianyuan Xu,Haodong Ji,Yu Gu,Tianyi Tong,Yabei Xia,Lizhi Zhang,Dongye Zhao
Licensed Content Date	May 15, 2020
Licensed Content Volume	388
Licensed Content Issue	n/a
Licensed Content Pages	1

Order Details

Type of Use	reuse in a thesis/dissertation
Portion	figures/tables/illustrations
Number of figures/tables/illustrations	1
Format	both print and electronic
Are you the author of this Elsevier article?	No
Will you be translating?	No

About Your Work

Title	Developing efficient photocatalysts for high-performance decomposition of perfluorooctanoic acid
Institution name	University of Technology Sydney
Expected presentation date	Jul 2022

Additional Data

Portions	graphical abstract

Requestor Location

Requestor Location	University of Technology Sydney PO Box 123 Broadway Sydney, New South Wales 2007 Australia Attn: University of Technology Sydney

Tax Details

Publisher Tax ID	GB 494 6272 12

Price

Total	0.00 AUD

Total: 0.00 AUD

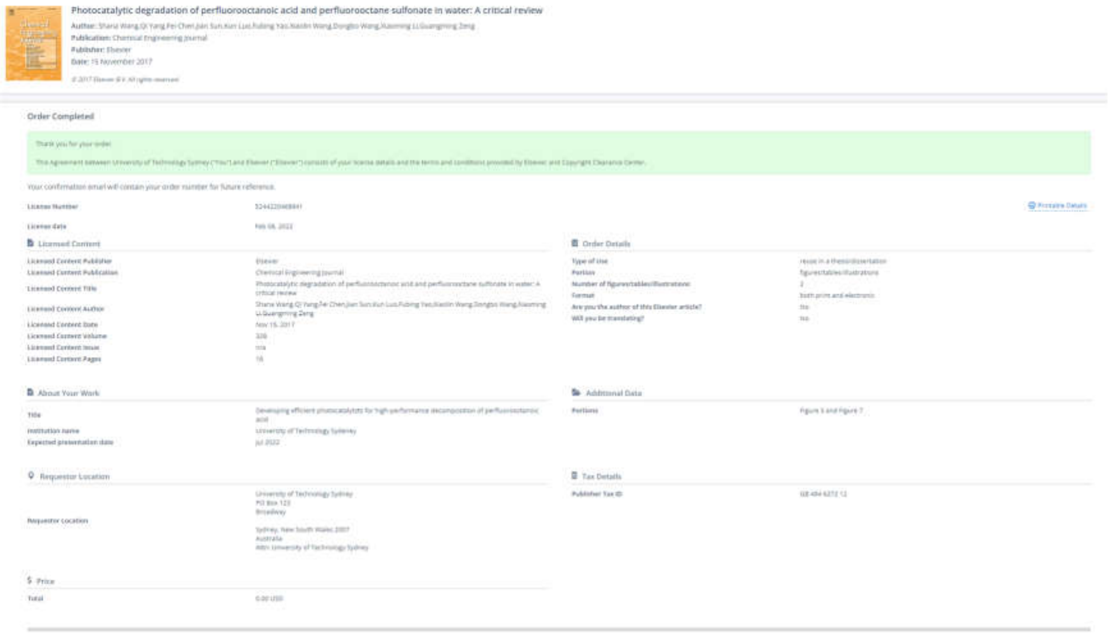

Photocatalytic degradation of perfluorooctanoic acid and perfluorooctane sulfonate in water: A critical review

Author: Shana Wang,Qi Yang,Fei Chen,Jian Sun,Kun Luo,Fubing Yao,Xiaolin Wang,Dongbo Wang,Xiaoming Li,Guangming Zeng
Publication: Chemical Engineering Journal
Publisher: Elsevier
Date: 15 November 2017

© 2017 Elsevier B.V. All rights reserved.

Order Completed

Thank you for your order.

This Agreement between University of Technology Sydney ("You") and Elsevier ("Elsevier") consists of your license details and the terms and conditions provided by Elsevier and Copyright Clearance Center.

Your confirmation email will contain your order number for future reference.

License Number	5244220468841
License date	Feb 08, 2022

Printable Details

Licensed Content

Licensed Content Publisher	Elsevier
Licensed Content Publication	Chemical Engineering Journal
Licensed Content Title	Photocatalytic degradation of perfluorooctanoic acid and perfluorooctane sulfonate in water: A critical review
Licensed Content Author	Shana Wang,Qi Yang,Fei Chen,Jian Sun,Kun Luo,Fubing Yao,Xiaolin Wang,Dongbo Wang,Xiaoming Li,Guangming Zeng
Licensed Content Date	Nov 15, 2017
Licensed Content Volume	328
Licensed Content Issue	n/a
Licensed Content Pages	18

Order Details

Type of Use	reuse in a thesis/dissertation
Portion	figures/tables/illustrations
Number of figures/tables/illustrations	2
Format	both print and electronic
Are you the author of this Elsevier article?	No
Will you be translating?	No

About Your Work

Title	Developing efficient photocatalysts for high-performance decomposition of perfluorooctanoic acid
Institution name	University of Technology Sydney
Expected presentation date	Jul 2022

Additional Data

Portions	Figure 5 and Figure 7

Requestor Location

Requestor Location	University of Technology Sydney PO Box 123 Broadway Sydney, New South Wales 2007 Australia Attn: University of Technology Sydney

Tax Details

Publisher Tax ID	GB 494 6272 12

Price

Total	0.00 USD